Source localization and connectivity analysis of uterine activity

Saeed Zahran

▶ To cite this version:

Saeed Zahran. Source localization and connectivity analysis of uterine activity. Bioengineering. Université de Technologie de Compiègne; Université Libanaise, 2018. English. NNT : 2018COMP2469 . tel-03770246

HAL Id: tel-03770246
https://theses.hal.science/tel-03770246

Submitted on 6 Sep 2022

Par **Saeed ZAHRAN**

Source localization and connectivity analysis of uterine activity

Thèse présentée en cotutelle pour l'obtention du grade de Docteur de l'UTC

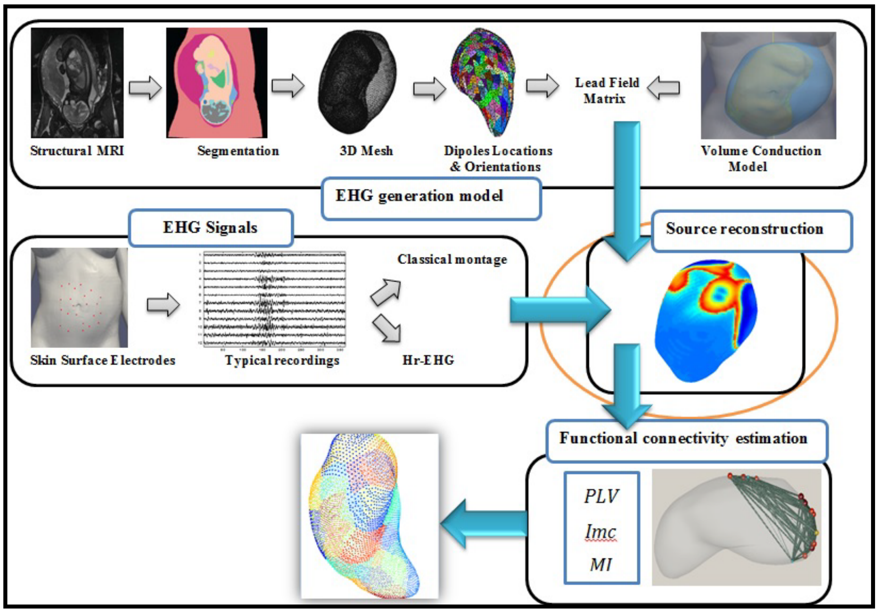

Soutenue le 18 décembre 2018
Spécialité : Bioingénierie et Informatique : Unité de Recherche en Biomécanique et Bioingénierie (UMR-7338)
D2469

Université Libanaise
Ecole Doctorale
Sciences et Technologie

utc
SORBONNE UNIVERSITES

COTUTELLE THESIS

To obtain the degree of Doctor issued by

Sorbonne University, Université de technologie de Compiègne
Doctoral School « Sciences pour l'Ingénieur »
and
Lebanese University
Doctoral School « Sciences et Technologie »

Presented and publicly defended by

Saeed ZAHRAN

Title:

Source localization and connectivity analysis of uterine activity

Spécialité : Bioingénierie et Informatique

18/12/2018

Jury Members :

Régine LE BOUQUIN	Prof., University of Rennes 1	Reviewer
Ziad O. ABU-FARAJ	Prof., American University of Science & Technology	Reviewer
Christine FERNANDEZ	Prof., University of Poitiers	Examiner
Mohamad HAJJ HASSAN	Assoc. Prof., Lebanese International University	Examiner
Jeremy LAFORET	Dr., University of Technology of Compiegne	Examiner
Ahmad DIAB	Asst. Prof., Lebanese University	Co-Director
Catherine MARQUE	Prof., University of Technology of Compiegne	Director
Mohamad KHALIL	Prof., Lebanese University	Director

Acknowledgments

I would like to thank my thesis supervisors: Prof. Catherine MARQUE, Prof Mohamad Khalil and Dr. Ahmad Diab for their insight, support and sharing of knowledge that has made this thesis possible.

Besides my advisor, I would like to express my sincere gratitude to Dr. Maxime Yochum for the continuous support of my Ph.D study and related research, for his patience, motivation, and immense knowledge. His guidance helped me in all the time of research. Furthermore, I am much obliged to him for his time for detailed discussions, his patience and encouragement as well as his ability to make a glass half empty look half full again.

My sincere thanks also goes to Dr. Marie Elisabeth Rognes and Dr. Christophe Grova for offering me the summer internship opportunities in their groups and leading me working on diverse exciting projects.

Furthermore, I would like to thank the members of the jury for taking the time to evaluate my thesis and for their participation in my PhD defense.

I would like to acknowledge the financial support of my work, that has been ensured by French government scholarship.

Finally, I must express my very profound gratitude to my parents for providing me with support and continuous encouragement throughout my years of study and through the process of researching and writing this thesis. This accomplishment would not have been possible without them. Thank you.

To each and every one of you – Thank you.

Contents

List of Figures

List of Tables

Acronyms

AP	Action Potential
AUC	Area under curve
BEM	Boundary Element Methods
Cx43	Protein connexin 43
cMEM	coherent Maximum Entropy on the Mean
EHG	Electrohysterogram
EHGSI	Electrohysterogram imaging
EEG	Electroencephalogram
ECG	Electrocardiogram
EHGSI	Electrohysterogram imaging
EMG	Electromyogram
FFN	Fetal Fibronectin
FWL	Fast Wave Low
FWH	Fast Wave High
FW-h2	Filtered Windowed-h2
GJ	gap junctions
GC	Granger causality
H	General synchronization
h2	Nonlinear correlation

Icoh	Imaginary part of coherence
IUP	Intrauterine pressure
LIF	light-induced auto fluorescence
MMG	Magnetomyography
MNE	Minimum norm method
MRI	Magnetic resonance imaging
ODEs	Ordinary differential equations
PTL	Preterm labor
PSD	Power spectral density
ROC	Receiver operating characteristic
Red3	Model reduction with only three variables
R2	Linear correlation
SNR	Signal to noise ratio
SD	Spatial dispersion
STF	space-time-frequency
STWV	space-time-wave-vector
SVB-SCCD	Sparse variation based sparse cortical current density
sLORETA	Standardized low resolution brain electromagnetic tomography
VB-SCCD	Variation based sparse cortical current density
WMNE	Weighted minimum norm
WHO	World Health Organization
ZEB1	Zinc finger E-box-binding homeobox 1

1

Introduction: Context and motivation

Electrohysterography is a non-invasive technique that records uterine activity with a high temporal resolution using an array of sensors, which are placed on the abdominal skin. The measurements contain valuable information about the electrical uterine sources [144]. This information is crucial for the diagnosis and management of some diseases (Preterm Labor) or for the understanding of the uterus functions. In this thesis, we are concerned with the localization of the active uterus regions, which are involved in uterine activity during contraction.

The ElectroHysterogram signals recorded at the skin surface (Electrohysterogram (EHG)) originate from a certain area of the uterus where a single cell can initiate contractions. But multiple cells, highly synchronized are needed for forceful and maintained contractions [115]. Furthermore, one active cell exhibits a burst of action potentials (bursting spikes). As a consequence, and contrary to the classical point source that can be modeled by a single dipole (one dipole at each vertex of the mesh oriented normal to the mesh surface), for the uterine muscle, the source space can be modeled by extended sources with patches (part of the region) presenting highly correlated actives cells. The objective thus consists in identifying the positions (and spatial extents) of the active uterus sources from the noisy mixture of signals which is recorded at the surface of the abdominal skin by the EHG electrodes. This is known as the inverse problem. On the other hand, deriving the EHG signals for a known source configuration through modeling is referred to as the forward problem (cf. Figure 1.1). Thanks to the advanced mathematical tools that permit to compute the so-called lead field matrix, which characterizes the propagation within the volume conductor, solving the forward problem has become straightforward. By contrast, finding a solution to the inverse problem is still a challenging task. This is especially the case in the context of multiple sources with time correlated signals, that are involved in the propagation phenomena. This problem is the key issue of this thesis and motivates the implementaion of algorithms that are robust to source correlation and to spatial extent.

The inverse problem in uterus has been formulated in different ways in order to non-invasively obtain valuable information about the uterus condition. Identifying the location and spatial extent of several highly correlated and simultaneously active uterus sources from abdominal ElectroHysterogram recordings and extracting the corresponding uterus signals is a challenging problem. The use of the EHG for imaging the sources of the uterine electrical activity could be a new and powerful diagnosis technique. However, the use of EHG gives limited performance as the uterus often demonstrates several simultaneously active regions and as EHGs present low signal-to-noise ratios. The purpose of this work is to study the ability of different distributed source localization methods to recover extended sources of uterus activity from abdominal EHG. Due to the lack of a gold standard to evaluate source localization methods, our evaluation was performed in a controlled environment using well-controlled realistic simulations of EHG signals, involving several locations. Simulated data were corrupted by physiological

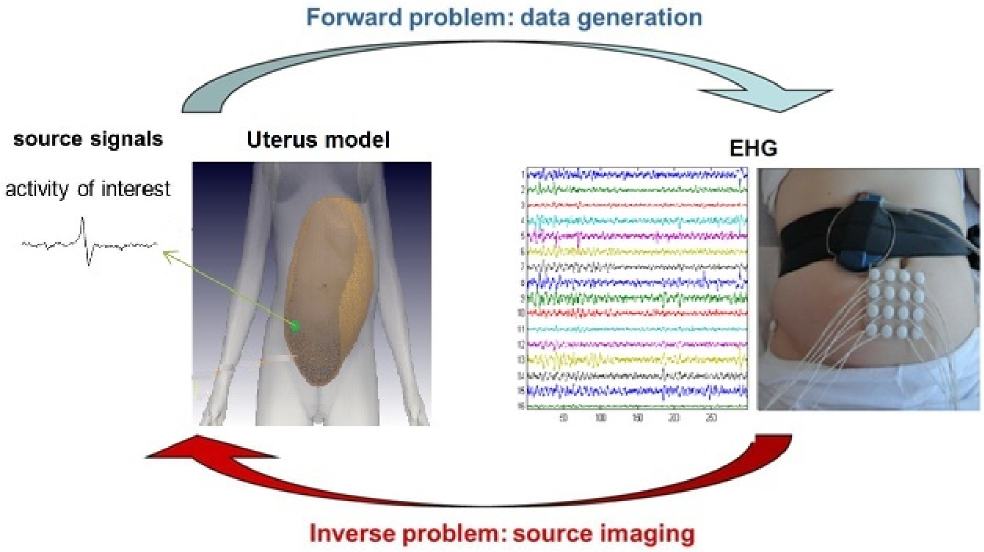

Figure 1.1: Illustration of the EHG forward and inverse problems

EHG noise. The performance of several state-of-the-art techniques for extended source localization is evaluated using a detection accuracy index based on the Dipole Localization Error, the Area Under the Receiver Operating Characteristic Receiver operating characteristic (ROC), Area Under the Curve Area under curve (AUC), and the Correlation Coefficient.

The forward problem is based on a previous work from our team [110], [134] where we consider the volume conductor with 3D realistic meshes (obtained from FEMONUM project [17])) extracted from Magnetic resonance imaging (MRI) images, where only the interfaces have meshed. This makes possible the use of Boundary Element Methods (BEM). The lead field matrix G is estimated using the BEM based on a $3D$ mesh of the interface, for the source model, and on a realistically-shaped abdominal model for the volume conductor. Interpreting the uterine activity requires realistic physiological models and accurate numerical solvers. A volume-averaged approach is employed for this model, which consists in considering that the uterus tissue is divided into two separate domains (intracellular and extracellular) assumed to be continuous. Because in future work we are interested in investigating the effects of mechanical deformation on simulated EHG, we need to compute both intracellular and extracellular potentials. This requires the use of the bidomain model. This model is derived by considering the uterus tissue as two superimposed Ohmic conductors that are separated by the cell membrane.

EHG inverse problems have no unique solution, since the number of sources is always much larger than the number of sensors. This is therefore an ill-posed problem, which requires additional assumptions to regularize the solution. Various $L2/L1-norm$ regularization techniques have been implemented to search for a unique solution which are referred to as the minimum norm solutions. They comprise techniques such as the original minimum norm method (Minimum norm method (MNE)) introduced in [79], the wieghted minimum norm (Weighted minimum norm (WMNE)) [89] and the standardized low resolution brain electromagnetic tomography (Standardized low resolution brain electromagnetic tomography (sLORETA)) [138]. In this work, we test a variation based sparse cortical current density Variation based sparse cortical current density (VB-SCCD) [48] together with its other extensions method [14], that are different from both L1- and L2-norm regularized MNE, since it uses the concept of sparse source imaging. We study their performance on realistic simulated data in comparison to the conventional source localization algorithms and tensor method.

Furthermore, we conduct a detailed study of the combination between the algorithm used to solve the EHG inverse problem and the algorithm used to measure the functional connectivity. We evaluate the combinations of three inverse solutions algorithms (Sparse variation based sparse cortical current density (SVB-SCCD), WMNE and coherent Maximum Entropy on the Mean (cMEM)) and four connectivity measures (Linear correlation (R2), Nonlinear correlation (h2) and Imaginary part of coherence (Icoh)). Furthermore, we conduct a detailed study of the influence of some experimental parameters, including inter-electrode spacing, number of electrodes and fat thickness, on these performances. The different steps of the comparative analysis are summarized in Figure 1.2.

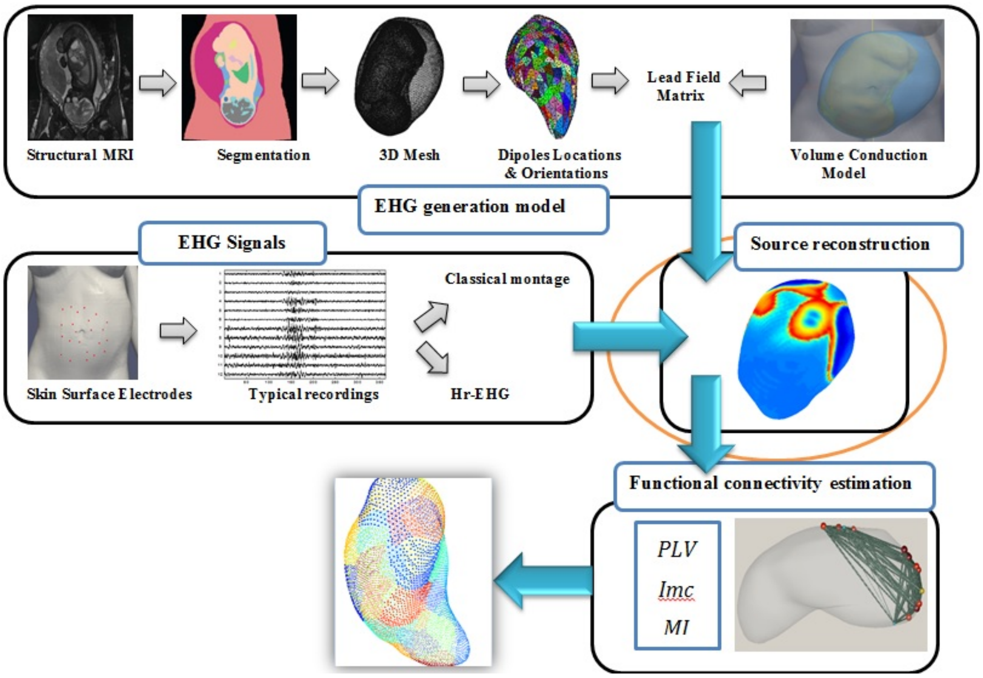

Figure 1.2: Illustration of the EHG forward and inverse problems

This thesis is organized as follows:

In Chapter 2, we provide some background information on the origin of electrical uterine signals, the characteristics of EHG systems, as well as uterine contraction. Furthermore, we describe the mathematical model of EHG that is employed for the simulations conducted in this thesis. In Chapter 3 we compare different inverse methods, to assess their detection accuracy when extended uterus areas are activated. In Chapter 4 we analyze the impact of the combination between the algorithm used to solve the EHG inverse problem and the algorithm used to measure the functional connectivity. In Chapter 5 we present the uterus electrophysiology model at the tissue level with continuum approximations via the bidomain equations.

Finally, Chapter 6 presents a general Conclusion and Perspectives of this work.

2

State of the art

Contents

2.1 Introduction

During the last few decades, the quest for knowledge of the uterus has been motivated, not only by a desire to reveal the secrets of this vital organ, but also by its growing clinical importance. Preterm labor is an important public health problem in Europe and other developed countries as it represents nearly 7% of all births. The annual societal economic burden associated with preterm birth in the United States was at least $26.2 billion in 2005 [92]. The pregnant woman gives birth at term between 37 and 40 weeks of pregnancy. However, this period may end prematurely and induce morbidity and mortality of newborns, when the woman gives birth before 37 weeks of pregnancy. An improved understanding of how the uterus works may lead to new techniques for the diagnosis and treatment of uterus problems. This serves as motivation for the enormous resources that are invested in uterus-related research. Indeed some days more in uterus can improve the maturation of the fetus. The early detection of a preterm labor (Preterm labor (PTL)) is important for its prevention.

The close link between the electrical activity and uterus problems is the basis of the diagnostic power of the Electrohysterography, which is the oldest non-invasive tool for diagnosing uterus conditions. The Electrohysterogram, EHG, is the recording of electrical potential differences on the body surface that result from the electrical activity in the uterus. These potential differences are caused by sources of electrical current in the active uterus muscle.

The electrical activity of the uterus is a well-studied process [29], both of the small scale processes occurring in the cells and of the organ-level pattern of electrical activation. Even so, there are a large number of mechanisms that are not fully understood. The organ-level electrical activity of the uterus is the result of billions of small-scale processes occurring in the cells, and the existing knowledge of how all these processes interact is very limited. A very promising technique to extend our knowledge in this field is the use of mathematical modelling and computer simulations. By formulating precise, quantitative descriptions of the small-scale processes, these models can be combined to form mathematical models of larger systems [185]. This field is often referred to as integrative physiology, and has the potential to improve significantly our understanding of how small-scale processes interact to form the functioning organ. In addition to their efficacy, experiments based on mathematical models and computations often represent a simpler, and less expensive, alternative to experiments with real uterus.

For the case of the electrical activity of the uterus, improved understanding may lead to improved treatment techniques and diagnosis, for instance in the form of more precise EHG analysis.

The focus of this thesis is on understanding the uterine activation process based on computer simulations of the electrical activity of the uterus. Particular emphasis is placed on simulating EHGs, but the simulation results have a number of other applications as well. To motivate the basics of the mathematical model, we will here provide a description of the EHG and the electrophysiology of the uterus [29].

2.2 Uterus Anatomy and Physiology

2.2.1 Uterus Anatomy

The location of the uterus is within the pelvic region directly behind the bladder, and frontal of the sigmoid colon. The non-pregnant uterus is pear-shaped, about 7.5 cm in length, 4 to 5 cm broad, and 2 to 3.0 cm thick and it weighs 50 to 70 grams [53]. The uterus can be divided anatomically into four portions: the fundus which corresponds to the upper portion, the corpus which is the main part of the uterus including uterine cavity, the cervix and the cervical canal [10] held in position within the pelvis by ligaments, which are called endopelvic fascia.

With pregnancy The uterus grows in size, increases in weight, and its walls thin out (Figure 2.1) [152]. During the first trimester, the uterus rises out of the pelvic cavity and reaches the level of the umbilicus by week 20. By weeks 28-30, the uterus reaches the epigastric region. The mother's abdominal viscera are displaced, and the skin and muscles of the anterior abdominal wall are greatly stretched. Uterine size increase is due to hypertrophy of preexisting muscle fibers for the most part and partly to development of some new fibers.

The uterus has three tissue layers. From innermost to outermost, these layers are as follows:

- Endometrium: is the inner epithelial layer that lines the uterus, along with its mucous membrane, of the mammalian uterus. Consists of a single layer of columnar epithelium plus the stroma on which it rests which is the innermost glandular layer and functions as a lining for the uterus. It consists of glandular cells that produce secretions. This membrane thickens to prepare the uterus for implantation of a fertilized egg. [59].
- Myometrium is the middle layer and forms the larger part of the uterine wall, consisting mainly of uterine myocytes. Its main function is to induce uterine contractions [4]. It is composed of three layers of smooth muscles. This layer has an active role during pregnancy. It increases both by hypertrophy of the existing cells and by multiplication of the cell number. During the last stage of gestation, the smooth cells reach a maximum length of 300 µm and a maximum width of 10 µm [39].

- Perimetrium: Serous layer of visceral peritonium. It covers the outer surface of the uterus, enveloping the body of the uterus and part of the cervix.

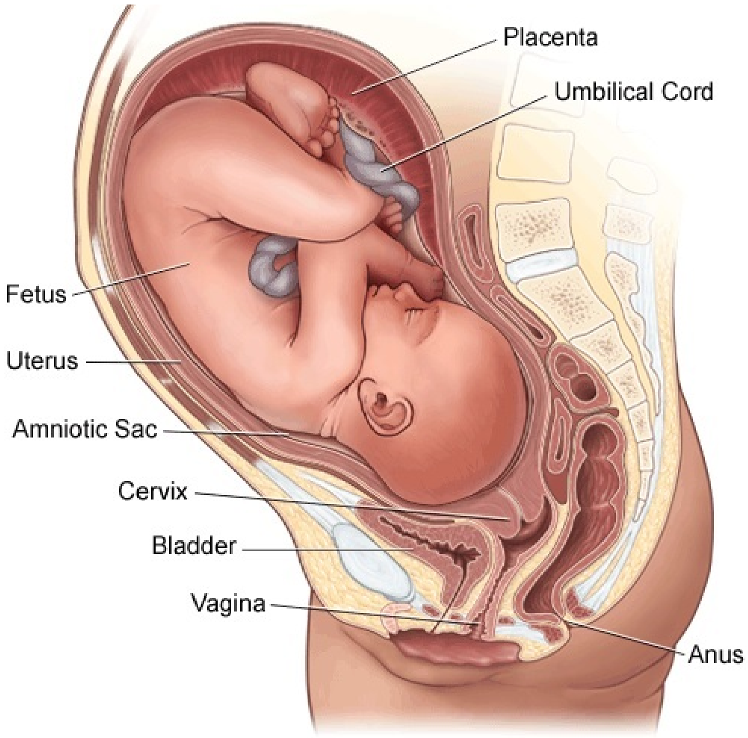

Figure 2.1: Anatomy of pregnant uterus ([2]).

The uterine smooth muscle fibers are arranged in overlapping tissue-like bands, the exact arrangement of which is a highly debated topic [44]. All myocytes (uterine muscle cells) are gathered in packages or ”bundles” with junctions between them. Packets are contiguous within a bundle or fasciculus. The bundles are arranged parallel to the surface of the uterus, transversely at the fundus and obliquely downward. Communicating bridges, named Gap Junctions, connect adjacent bundles. A diagram of this structural organization is shown Figure 2.2.

2.2.2 Uterine activity

Uterine contraction take place after the generation and propagation of electrical activity in the myometrium cells [69], [150], [149]. The electrical activity depends on two parameters related to the contractile process: the excitation and the propagation of the electrical activity. The evolution of uterine contractions is therefore related to an increase in cellular excitability as well as an increase in the synchronization of the entire uterus [69].

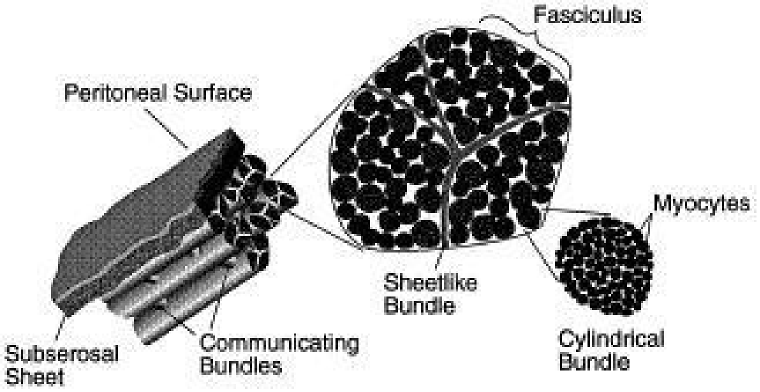

Figure 2.2: Three-dimensional structure of the woman uterus [141].

2.2.2.A Cellular excitability

The electrical activity of one cell can be characterized using two types of potential: the resting potential and the action potential. The resting potential is formed of a slow wave, of small amplitude, of the electrical activity of a membrane. Above a certain threshold of variation of this resting potential, the action potentials are generated. One action potential is due to sudden variations in the permeability of the cell membrane. During pregnancy, the physiological electrical activity is composed of discontinuous bursts of action potentials (figure 2.3)). This inconstant electrical activity has the consequence of the existence of irregular uterine contractions, of low intensity of certain parts of myometrium. On the other hand, term and labor uterine electrical activity is composed of regular bursts with several peaks of action potential (figure 2.3) that propagate to the entire myometrium in a short time, leading to regular intense contractions [160].

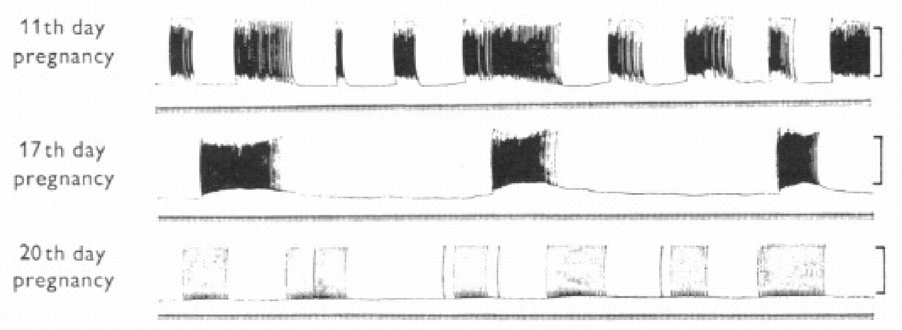

Figure 2.3: Electrical activity of rat uterus at different terms of pregnancy [94]

2.2.2.B Uterine synchronization

Myometrial cells can either trigger their own activity or be excited by the action potentials from a neighboring cell. This propagation of the electrical activity in the uterine muscle is ensured by the local electric potential propagation between active cells to their inactive neighbors, electrically coupled through local ionic currents [108]. The inter-cell electrical coupling is improved by the presence of gap junctions (gap junctions (GJ)). These gap junctions are areas where the membranes of two adjacent cells form pores allowing an electrical coupling. Gap junctions (Figure 2.6) are connections created by the protein connexin 43 (Protein connexin 43 (Cx43)) [66]. These gap junctions provide channels of low electrical resistance between cells [99]. These junctions allow the passage of small molecules, and facilitate electrical connection. It appears that the gap junctions have a significant role in the development of a synchronous electrical activity when approaching delivery. During gestation, the number of junctions is much low. The GJ are created in large number few hours before delivery, ensuring the development of a synchronized muscle activity (figure 2.4).

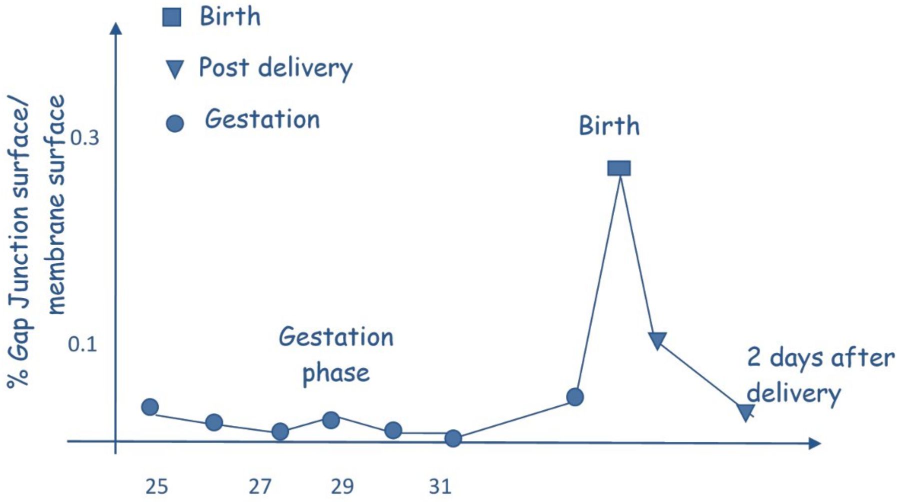

Figure 2.4: The evolution of Gap junction number during gestation, birth and after delivery [64].

The human uterus shows a low level of order for the majority of pregnancy, and activity at any one time, at different places in the uterus, is very similar. Dramatically, this picture changes at the time of labor with an increase in contractility, energy consumption, and order, as the activity at different times is different, either relaxed or contracting (Figure 2.5) [75]. The uterus initiates and coordinates the firing of individual myometrial cells to produce organized contractions causing the expulsion of the fetus from the mother's body. The contractile activity of the uterus results from the excitation and propagation of electrical activity.

In the human being, contractility of the uterus is impeded at the starting of pregnancy to permit implantation. Hormonal signals inhibit uterine contractility. The signals derive from the maternal ovary that produces progesterone [57]. The progesterone suppresses myometrial contractility, providing a "brake" on the uterus. The brake decreases uterine contractility for the wide majority of pregnancy. The brake technique contains keeping single myocytes disassembled from one another. This is done by

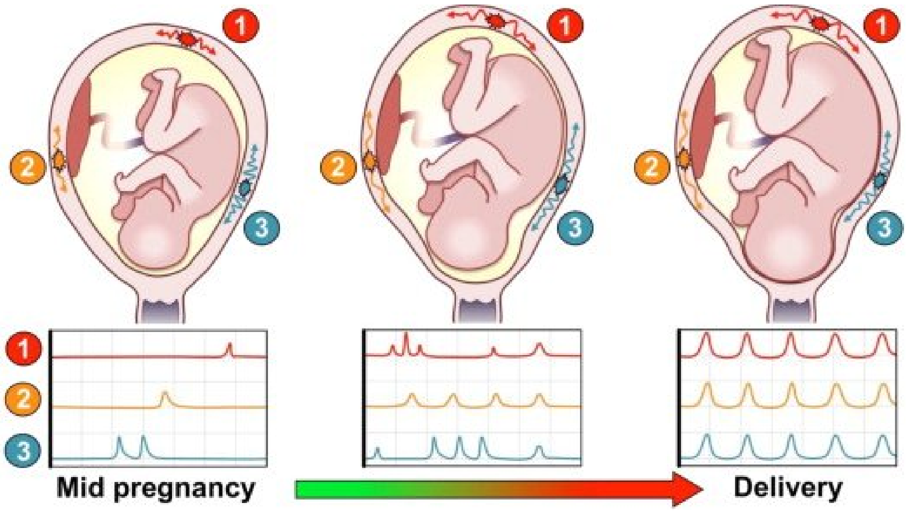

Figure 2.5: The gradual development of synchronous behavior in areas of the uterus that eventually lead to the widespread rhythmic contractions of the uterus that increase intrauterine pressure and dilate the cervix at the time of labor [164].

decreasing gap junctions between individual myocytes [158].

Throughout most of pregnancy, and in all species studied, these cell-to-cell channels or contacts are low, with poor coupling and decreased electrical conductance. The formation of Cx43 is suppressed by a transcription factor called zinc finger E- box binding homeobox (Zinc finger E-box-binding homeobox 1 (ZEB1)), which is stimulated by progesterone [147]. The suppression of Cx43 expression guarantees that even if a myometrial cell depolarizes, the electrical signal does not go far and no increase in intrauterine pressure occurs.

At term, however, the cell junctions increase and form an electrical syncytium required for coordination of myometrial cells for effective contractions. A large number of gap junctions between myometrial cells is observed during labor [63] ensuring the development of a synchronized muscle activity (Figure 2.4) due to electrical diffusion. The available data strongly support the presence of a brake on uterine contractility provided by progesterone. The hypothesis of the progesterone block was developed by Csapo [38] in the middle of last century and for many years little further progress occurred. A primary problem was how the block was removed. It seems that in human beings, estrogen action may increase to override the action of the progesterone brake. Estrogen has many actions on the uterine myometrium. Acting via micro- RNA species estrogen action reduces the formation of ZEB transcription factors that inhibit production of Cx43 [148, 179]. These events combine at the end of pregnancy to dramatically increase the connectivity of myometrial myocytes, which makes them more likely to concurrently depolarize and to remain depolarized longer (Figure 2.7) [173]. The increase in connectivity between individual myocytes at the end of pregnancy and the increase in myocyte excitability allows the myocytes to behave as coupled oscillators and generate coordinated contractions.

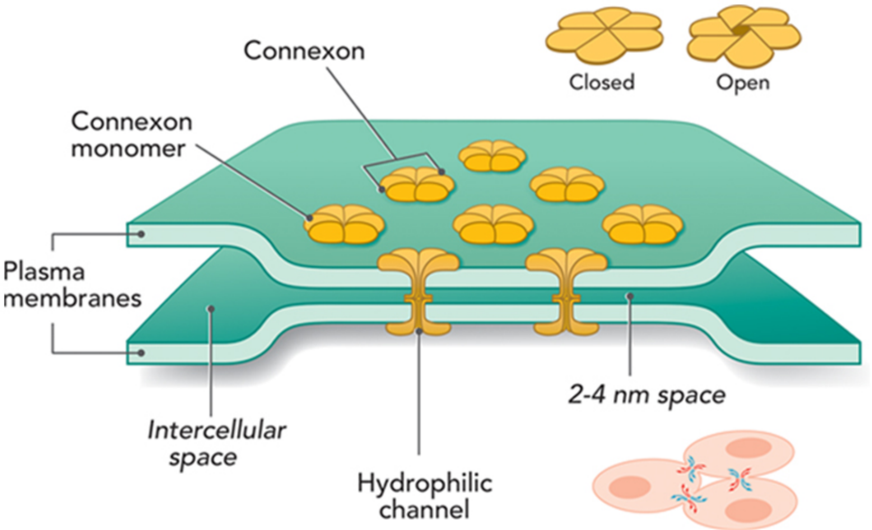

Figure 2.6: A representation of gap junctions [171].

The area over which an action potential could spread is a key determinant of the development of synchronous contractions. If the area over which an action potential could spread is large enough, contraction of this region or patch of tissue would increase intrauterine pressure leading to an increase in uterine wall tension [40]. Increased uterine wall tension then provoked widespread synchronous contraction of myocytes. If the area over which an action potential propagated is too small to raise intrauterine pressure then no synchronous contractions of the whole uterus would occur. Synchronous contractions across the uterus raise the intrauterine pressure leading to dilation of the cervix.

Although the quintessential endpoint of labor is cervical dilation, it is critically important that the uterus generates large intrauterine pressures for dilation to occur. The concept of assessing intrauterine pressure is still relevant and clinically useful for determining the adequacy of uterine contractions [6] [28]. The areas of the uterine wall that were not participating in a contraction would elongate when the actively contracting areas increased wall tension, and elongation of the passive areas would attenuate the rises of pressure. Because of this effect, high pressures of labor can be generated only when most of the uterine wall is contracting at the same time in a coordinated manner [40].

In summary, from Caldeyro-Barcia, we learned that frequent contractions that consistently generate high intrauterine pressures are necessary and sufficient for labor. From Csapo, we understand that in order to achieve the high pressures, the uterus must somehow contract most areas at the same time. Caldeyro-Barcia described his ‘triple descending gradient’ model of uterine function as a wave-like contraction which starts at the fundus, spreads down the uterus, and decreases in strength and duration

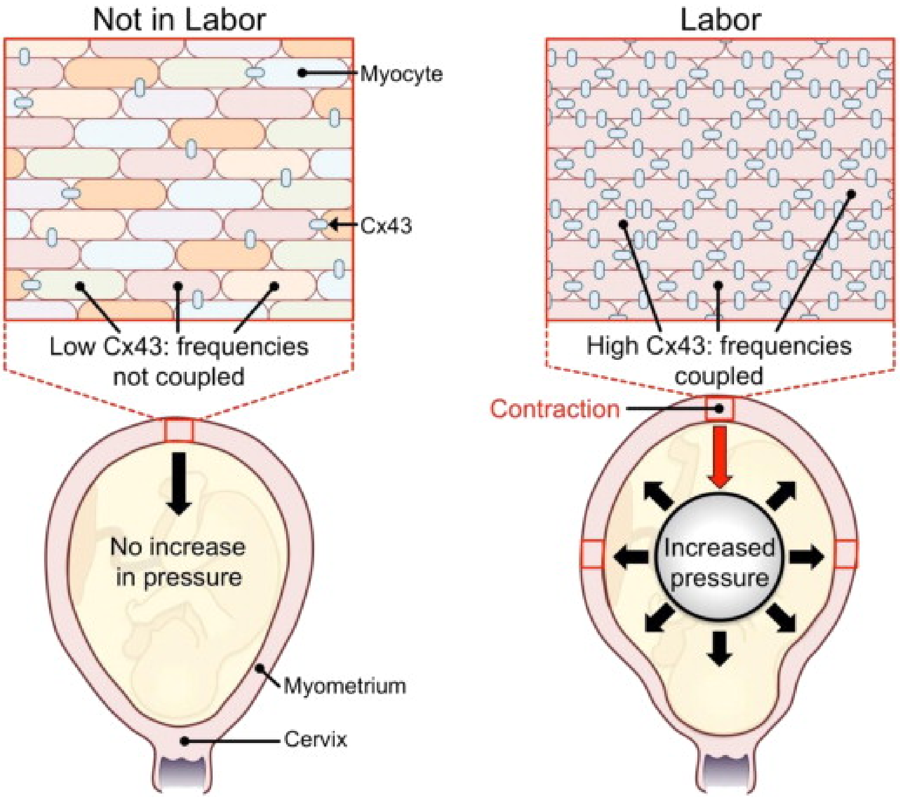

Figure 2.7: Labor and Not in Labor illustration with the expression of Cx43 that are required to increase intrauterine pressure [164].

as it progresses [6]. The fact that uterine muscle creates bioelectrical activity as it contracts was established at the time, although Caldeyro-Barcia did not emphasize that contractile activity occurs as a direct result of electrical activity. Detailed investigations into the electrical properties of uterine cells and tissue began in the mid-1950s, and the concept of excitation–contraction coupling in myometrium was soon formalized ([41], [74], [123]). In 1963, Csapo and Takeda [42] reported that when in active labor, uterine bioelectrical signals were expressed in synchrony with the generation of intrauterine pressure. He defined contractions that remained local as nonpropagating and labor contractions as propagating [40]. These terms were likely chosen to emphasize that his concept for all uterine signaling involved action potential propagation. Connexin 43 is the protein responsible for cell to cell electrical coupling in the heart, and Garfield's discovery of connexin 43 in the uterus [66] provided a mechanism for uterine electrical communication. Through the 1980s and 1990s, emerging data supported the concept that connexin 43 increases myometrial excitability, and inferred that action potential propagation is the mechanism for both short- and long-distance electrical signaling ([62]). Through the end of the twentieth century, action potentials were thought to perform three important functions: initiating and maintaining cellular contractions, recruiting cells for participation in the contraction, and organ-level signaling to coordinate contractile activity in all parts of the uterus. Yet discrepancies arose when experimentally testing action potential propagation as the mechanism for signaling long distances. There is a significant doubt that myometrial action potentials travel in straight paths. In sheep [11], rodent [97], and human [21], [165] action potentials are not found to travel linearly.

In their recent review, Rabotti and Mischi concluded that electrical propagation in human is unpredictable and demonstrates complex patterns [143]. Using a 152 element array of superconducting quantum interference devices (SQUID), Ramon and coworkers (2005) found that localized biomagnetic activity (and by direct inference, bioelectrical activity) appeared suddenly in random locations that were not contiguous or anatomically related to each other. Hence the enigma – action potentials appear to propagate slowly in tissue, in complex pathways, noncontiguously, and over only short distances.

Like cardiac cells, uterine myometrial cells can generate either their own impulses -pacemaker cells- or can be excited by the action potentials propagated from the other neighboring cells -pacefollower cells. But unlike cardiac cells, each myometrial cell can alternately act as a pacemaker or a pacefollower. In other words, there is no evidence of the existence of a fixed anatomic pacemaker area on the uterine muscle [115]. The spontaneous oscillations in the membrane potential of the autonomously active pacemaker cells lead to the generation of an action potential burst when the threshold of firing is reached. The electrical activity arising from these pacemaker cells excites the neighboring cells, because they are coupled by electronic connections called gap junctions. It is believed that the action potential burst can originate from any uterine cell, thus the pacemaker site can shift from one contraction to another.

Many hypotheses on the pacemaker cells have been issued including their number, position ... It seems that there is a one or more preferential pacemaker activities loci near the fundus, as found by Caldeyro-Barcia et al. [27]. This activity is then propagated in all directions, but ultimately from the fundus to the cervix.

A more recent hypothesis explains the long-distance uterine synchronization by means of a hydrodynamic-stretch activation mechanism [91], mechano-transduction process, rather than to solely the classical electrical propagation hypothesis, presented above. The synchronization of uterine contractility is thus related to two distinct phenomena: electrical propagation through GJs (local electrical diffusion) and mechano-transduction process (global uterus synchronization) [91]. This mechano-transduction process will be detailed in section 2.6.

2.3 Problem of preterm labor

Preterm birth, that is, birth before the 37th week of pregnancy, remains a major problem in obstetrics. In Europe and other developed countries, the incidence of preterm birth is between 5 and 12%. According to the definition of the World Health Organization (World Health Organization (WHO)), preterm delivery is a delivery at a gestational age of less than 37 completed weeks or less than 259 days of amenorrhea. Every birth occurring after 22 weeks of amenorrhea and before 37 weeks is defined as a premature birth. A birth occurring before 22 weeks of amenorrhea is considered as an abortion by WHO. Also, preterm birth accounts for 85% of infant mortality and 50% of infant neurologic disorders [71]. Infants born prematurely are at high risk of mortality as well as health and development problems [71], [36]. Preterm birth is a pathology that can lead to serious consequences for the child and has also a socio-economic cost. The main risks to children are:

Preterm birth is a pathology that can lead to serious consequences for the child and has also a socio-economic cost. The main risks to children are:

- Respiratory distress (often associated with hyaline membrane disease)
- Infection
- Neurological Diseases
- Hypothermia
- Necrotizing enterocolitis

2.4 Methods for monitoring pregnancy

Optimal detection of labor implies finding markers indicating that the labor will occur, but also predicting whether it will actually result in a premature birth (premature labor). There are several methods presently used for the monitoring of pregnancy, among them:

- Intrauterine pressure (Intrauterine pressure (IUP)), the mechanical effect of uterine contraction, is a direct method providing precise information concerning uterine contractions efficiency. For its measurement, a catheter is inserted into the uterine cavity and connected to a pressure sensor, giving information on the duration, amplitude and frequency of appearance of the contractions [68]. Despite the accurate information provided by IUP, its major drawback is its invasiveness. IUP cannot clearly be used during pregnancy as it requires rupture of the membranes in order to insert the catheter into the amniotic sac. Therefore, it can increase the risk of infection or accidental labor induction [160].

- Tocography being external and non-invasive, is the most widely used method for monitoring uterine contractions during pregnancy. This device contains a force sensor placed on the mother's abdomen, usually over the uterine fundus. This sensor measures the deformation of the abdomen as a result of a contraction [24] and provides only quantification of the number of contractions per time unit. This parameter has been demonstrated being not predictive of delivery [26].

- Biological tests, such as fibronectin, have been clinically used for the prognosis of premature births [87], although they have a low predictive value.

- A noninvasive technique named light-induced auto fluorescence (light-induced auto fluorescence (LIF)) has been proposed for labor monitoring [65]. It attempts to evaluate optically the concentration of collagen in cervical tissue.

- The measurement of cervix length via endovaginal ultrasonography, Cervical changes, when evidenced by sonographic measurement of cervical length, may be an accurate indicator of women needing specific therapeutic monitoring [154], [100]. The sequential use of cervical sonography and fibronectin test appears to give better results indicator of preterm risk. However, these indicators are mainly associated with a strong negative predictive value. Furthermore, using this technique needs cervical dilation and effacement, and may induce vaginal bleeding, or ruptured membranes [37]. It is thus not adapted to preterm labor detection.
- Magnetomyography (Magnetomyography (MMG)) measures the magnetic fields associated with the uterine action potentials. It is a noninvasive technique. A device based on 151 magnetic sensor array were used to MMG recording of spontaneous uterine activity [55].

- Fetal Fibronectin (Fetal Fibronectin (FFN)) [126], α-fetoprotein [180], Placental peptides [119]. They have been proposed as methods for monitoring patients that have a risk for premature labor. Some results show that FFN can be used for the prediction of premature labor [87].

- One of the promising methods to monitor the efficiency of uterine contractions during pregnancy is the analysis of the electrical activity of the uterine muscle, the electrohysterogram (EHG) [114], recorded on the mother's abdomen [6], [168].

2.5 The Electrohysterography

Labor and delivery are preceded by two physiological phenomena: increased excitability and increased connectivity between the myometrial cells, which results in an increase in the propagation of the action potentials that trigger the uterine contractions [44]. Electrohysterogram EHG is the non-invasive measurement of the electrical activity related to uterine contractions. It originates from the depolarization-repolarization of billions of smooth muscle myometrial cells. It is a technique that records uterine activity with a high temporal resolution by using one pair or an array of electrodes, which are placed on the abdominal skin. The measurements contain valuable information about the electrical uterine sources. It permits to monitor the efficiency of uterine contractions during pregnancy. This information is crucial for the diagnosis and management of some diseases or for the understanding of the uterus functions. It is one of the most promising bio-physical markers of PTL. The parameters derived from the EHG signal have been considered, both in time [98,166], and in frequency domains [65,98]. The uterine contractility depends on the excitability of uterine cells and on the propagation of the electrical activity to the whole uterus [44]. Both aspects influence the spectral content of EHG, mainly composed of two frequency components, traditionally referred to as Fast Wave Low (FWL) (Fast Wave Low) and Fast Wave High (FWH) (Fast Wave High). These frequency components may be related to the propagation and to the excitability of the uterus respectively [122]. Several studies have already been realized in the context of preterm labor detection by processing EHG.

EHG is low-cost, non-invasive and thus easily suitable for pregnant women. The exploration of contraction behaviors at the uterus level, by using EHG inverse solutions may help to shed light on dysfunctional process of the uterus and on the clinical diagnosis of severe diseases which can also impact the baby. Noway, there is no effective detection for preterm labor, and when it exists, it is often too late to delay it. EHG source imaging (Electrohysterogram imaging (Electrohysterogram imaging (EHGSI))) may provide a solution to detect preterm labor sooner, which could permit to use treatment more efficiently.

Several tools of EHG signal processing have been used first to analyze the excitability (linear method and nonlinear method) from processing only one EHG lead (monovariate analysis), and then to study the propagation of uterine electrical activity, by using correlation between 2 EHG leads (Bivariate analysis).

Linear methods, in both time and frequency domains, were the first used to extract features from one EHG signal. Recently, much attention has been paid to the use of nonlinear analysis techniques for the EHG characterization. Additionally, in the last few years, several teams focused on the study of uterine synchronization based on multi-electrode EHG recordings.

2.5.1 Excitability analysis - Linear parameters

The first parameters used for the characterization of uterine contractility/excitability were extracted from the time domain [112], [73], [113], [23], [116], [191], [161]. Then several EHG analysis and characteristics extraction were made in other domains. These include frequency representation, through Fourier transform and time-frequency representation or wavelet transform.

In the frequency domain, the power spectral density (Power spectral density (PSD)) of the electrical activity has been used in several studies. By using PSD, several variables were calculated, such as peak frequency, [22], [107], [70], [101], [49], [176], [163], [106], mean frequency [172], median frequency [58]. The ratios of the energies contained in several frequency bands, or the relative energy, have also been used for the characterization of the efficiency of contractions .

Some authors have also used time–frequency methods such as wavelet decomposition [9], [47] to characterize EHG. They extracted relevant parameters, after the decomposition into details coefficients.

2.5.2 Excitability analysis - NonLinear parameters

In an attempt to improve the results obtained when using linear methods, and as the EHG, like other biomedical signals, seems to present some nonlinear characteristics, several measures have been proposed for detecting nonlinear characteristics in the EHG. Radomski et al. [145] have applied sample entropy to identify regularity in uterine EMG.

Ivancevic et al. [88] have presented a review on the nonlinear parameters used for the prediction of preterm birth. One of the studied methods of interest is the Lyapunov exponent that studies the stability of the signal and its sensitivity to initial conditions.

Diab et al. [46] compared the performances of several nonlinear methods (time reversibility, sample entropy, Lyapunov exponent and delay vector variance) on synthetic signals. The aim was to test their sensitivity to the change of signal complexity, with or without noise. Then, they applied these methods on contractions recorded during pregnancy and labor. Results on synthetic signals showed that time reversibility is less sensitive to changes in noise. On real signals, the results show a clear superiority of time reversibility in classifying pregnancy and labor EHG.

2.5.3 Synchronization analysis – propagation/connectivity parameters

Several studies have been realized to characterize the uterine propagation by means of the synchronization between EHG signals recorded at the abdominal surface. These efforts were based on various methods such as i) correlation/connectivity analysis [56] [83], [111] where the methods were applied on the entire uterine burst manually segmented, and ii) propagation velocity quantified by analyzing either the propagation of whole bursts of EHG [106], or single spikes identified within bursts [106]. Indeed, looking at the connectivity at the electrode level, bivariate analysis, could provide important information on the synchronization of the uterine activity.

These methods used recently to characterize the Correlation/connectivity can be divided into two types: phase synchronization (mean phase coherence and phase entropy) [82]; linear (R2) and nonlinear (h2) correlations [84]. They permit to characterize the connectivity between 2 EHGs, recorded at different locations on the abdomen, and study either its evolution during normal pregnancy, or its ability to discriminate pregnancy and labor contractions. Marque et al. have used the linear correlation coefficient (R2) and noticed more correlation in low than in high frequencies [155]. Duchene et al used autocorrelation, cepstrum and deconvolution function in order to study the uterine Electromyogram (EMG) propagation [51]. Their results show that no linear propagation can be evidenced from all developed methods. The linear inter-correlation has been also used for EHG propagation analysis by Karlsson et al. [90]. They used 16 electrodes for the EHG recording. They present both an animation of the evolution of the electric potential, as well as a temporal correlation evolution. They observed complex activation patterns. Mansour et al. used the inter-correlation function to analyze the propagation of the internal uterine EMG of a monkey by using four internal electrodes [109]. The signals were first filtered into FWL and FWH frequency bands. Their results indicate that the correlation during labor is higher for FWL than for FWH. Other studies used the nonlinear correlation coefficient to estimate the relationships between 16 EHG signals recorded by a matrix of 4x4 electrodes placed on the woman's abdomen [83]. Authors showed a significant difference between pregnancy and labor contractions [84] as well as an increase in the correlation of EHGs as labor approaches [128]. Recently, Diab et al. [45] performed a comparative study between several correlation measures applied to EHG signals. Authors used the nonlinear correlation coefficient (h2), General synchronization (General synchronization (H)) and the Granger causality (Granger causality (GC)). They tested the sensitivity of these methods to some characteristics of the signal (non-stationarity, frequency content) or to the recording protocol (bipolar or monopolar recording), in order to improve the performance of the coupling detection methods for the classification of EHG bursts recorded during pregnancy and labor. They processed EHG signals recorded from 48 women during pregnancy (174 contractions) and labor (115 contractions), with a 16 electrode matrix (4x4). The h2 coefficient did not demonstrate any monotonic increase from pregnancy to labor. Therefore, authors tried to improve the performance of this method. They retained only the low frequency band of the EHG

(FWL), which is supposed to be more related to the propagation of EHG, and proposed a time varying approach. The combination of these two preprocessing steps (windowing, filtration step to retain only FWL), Filtered Windowed-h2 (Filtered Windowed-h2 (FW-h2)), leads to an increase in h2 performance.They obtained good performance with an increase from pregnancy to labor. They also noticed that H method performance is highly influenced by the nonlinearity of EHG signals and therefore requires further investigation. Monopolar recordings gave better results than bipolar ones.

However, in almost all previous studies, reported above, about the synchronization of uterine elec-trical activity [45], authors estimated the correlation between multiple EHG. The EHG correlation matrices were often reduced keeping only their mean and standard deviations. Despite the encouraging results obtained, relevant information may have been missed due to this averaging, which may induce the relatively low classification rate reported so far. To characterize precisely the correlation/connectivity of uterine sources of activity, Nader [130], [131] proposed to use a network measure technique based on graph theory, She based her work on the estimation of a correlation matrix by using H2, R2 or the Imaginary part of the coherence (Icoh), the quantification of the obtained connectivity matrices using graph theory-based parameters, the clinical use of these measures for pregnancy monitoring as well as for the classification between pregnancy and labor EHG bursts. This network-based approach demonstrated very promising tool to quantify uterine synchronization, when applied at the abdominal level, for a better pregnancy monitoring.

Furthermore, most of these methods were applied to surface signals, representing each a mix of activity coming from different sources. Nader tested, as a first trial, the application of the connectivity analysis to the source of EHG, identified by a simplified approach [129]. The aim of this thesis is to study further the possible interest of the application of the connectivity analysis at the source level. We thus work on the best way to identify the sources directly by means of inverse methods, as well as the best mean to study the connectivity of the obtained sources. We mainly developed our study on simulated realistic signals, and then applied the best method to real EHGs.

2.6 Mechanotransduction mechanisms

The first experimental report indicating that mechano-transduction might be important in organ-level signaling for the uterus appeared in 1965 by Takeda, who studied the repressurized postpartum rabbit uterus [91]. Mechano-transduction mechanism, was initially proposed by Takeda [170], as the origin of global uterine muscle synchronization [188]. Briefly, a contraction starting from one part of the uterus, induces the contraction of another part, not only by electrical diffusion through the tissue, but also by means of the tissue stretching related to the induced increase in the intrauterine pressure (IUP). An interesting study proposed by Young proves that mechano-transduction exists on uterine tissue from rat [189], where a uterus piece contracts, due to its stretching induced by the contraction of a second uterus piece. This theory is possible due to the existence of electrical stretch-activated channels in the membrane of smooth muscle cells [86], [157]. These channels are mechanotransducers as they convert a tissue stretching (induced by the intrauterine pressure) into a biological signal (ionic current inward or outward the muscle cell). For smooth muscle cells, they concern particularly the calcium and sodium channels [192], [193]. While the stretching of uterine parts, initially inactive, increases due to the increase in the intrauterine pressure induced by the active parts of the uterus, these channels open and then induce the contraction of the stretched part by mechano-transduction. This process permits to initiate the long-distance synchronization of the uterine muscle, and may partly explained the poor results obtained when trying to quantify global uterine synchronization.

2.7 EHG Recording

The EHG signal has been studied mainly after segmentation of the electrical bursts corresponding to the mechanical contractions of the uterus [117]. Marque et al. [114] used bipolar Ag/ AgCl surface electrodes (8 mm diameter, 2.5 cm spacing) for recording EHG. A reference electrode was positioned on the women's hip. They indicate that the best electrode position was the median vertical axis of the woman's abdomen.

Simultaneous recording of internal and external EMG activity on the same woman showed a very good correlation between the two signals [181]. This demonstrated that the surface EMG signal is representative of the electrical activity of the uterine muscle. These results have been confirmed in an analysis of the EMG signal of the pregnant macaque [109]. Using these results, the external uterine EMG has become a standard non-invasive method for the study of uterus electrical activity.

The electrohysterogram (EHG), that is the uterine EMG recorded, by using surface electrodes, is characterized by a low frequency activity (0.1 to 0.3 Hz) with a superimposed activity of higher frequency (FW, fast Wave: 0.3 to 2 Hz). The low frequency signal is considered as the result of mechanical disturbances induced by the deformation of the abdomen under the effect of contractions [168]. At the opposite, FW (parted then in two components FWL - Fast Wave Low- and FWH - Fast Wave High) is related to uterine contractions.

During the BioModUE-PTL, a new multielectrode system has been used (Porti 32, TMSi) that offers recording of up to 32 channels (Figure 2.8). Based on this system, we standardized the protocol using Ag/AgCl electrodes (8mm diameter), positionned as a 4x4 matrix placed on the woman's abdomen (the third electrode column of the grid being set on the uterine median axis, and the 10-11h electrode on the middle of the uterus), with two reference electrodes on each woman's hips. The collected signals are fed into an amplifier and then to an A/D converter (PORTI 32). Then, by using an optical fiber and a USB cable, the signals are digitized (Sampling frequency equal to 200Hz) by a PC where they can be saved on disk or uploaded to an online database. Another signal called TOCO (output of a tocographic probe) is also recorded by using the probe placed above the electrode matrix (figure 2.8). This signal is further used for EHG bursts segmentation.

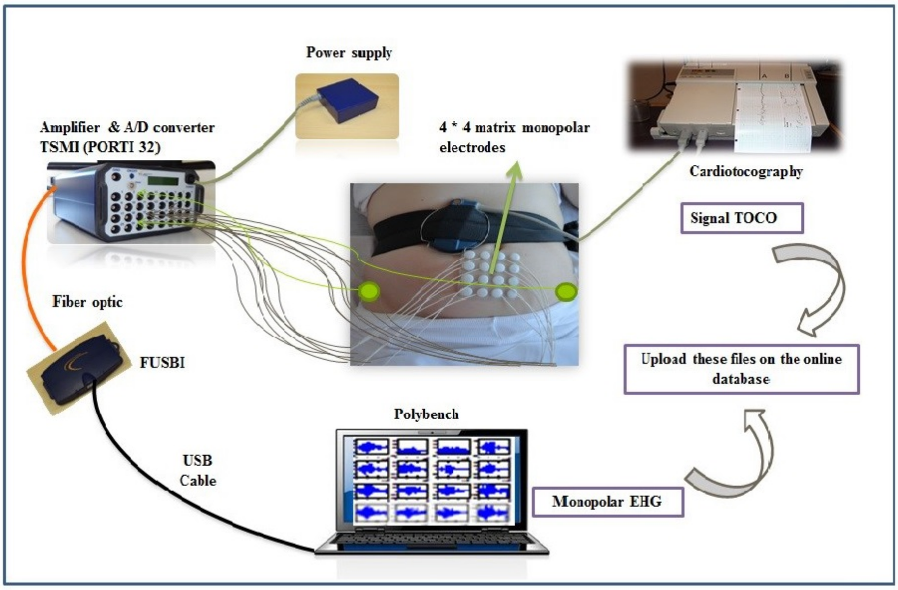

Figure 2.8: The new multichannel system: 4x4 electrode matrix placed on the women abdomen with two reference electrodes on the hip and the tocographic probe.

To increase the signal to noise ratio, we calculated the vertical bipolar signals, obtaining thus 12 bipolar signals (Figure 2.9). The monopolar and bipolar bursts of uterine electrical activity that correspond to contractions were manually segmented, based on the TOCO signal recorded simultaneously. The tocodynamometer paper trace was digitalized in order to facilitate the segmentation of the uterine contractions (Figure 2.9).

2.8 Inverse problems for imaging uterine activity

The application of biomedical source localization is not new. Source imaging applied to Electroencephalogram (Electroencephalogram (EEG)) [77] or electrocardiography (Electrocardiogram (ECG)) [85] signals, attempts to reconstruct internal electrical activity of the body by using surface measurements on the scalp in the case of EEG, on the torso or the limbs for ECG. Source imaging techniques are a powerful tool for the analysis of human organs and biological systems. Their common feature is that they require mathematical modeling of the acquisition process and numerical methods for the solution of

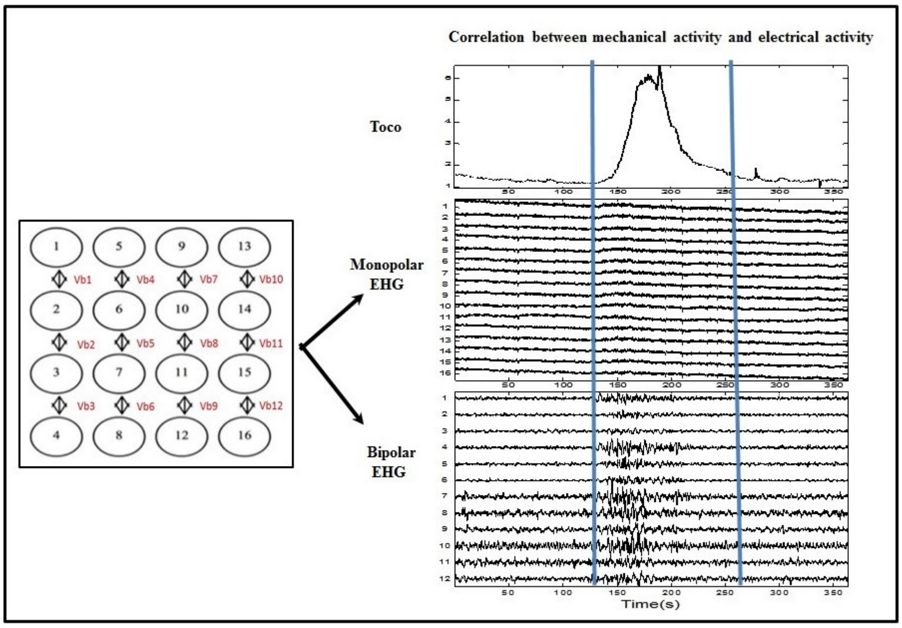

Figure 2.9: Digitized tocodynamometer paper (Top), monopolar signals (middle), corresponding bipolar signals (bottom). The blue lines define the beginning and the end of the contraction according to TOCO.

the equations relating the data (the signals) to the unknown object (the sources of activity). Their main feature is that the problems to solve are ill-posed, so that their solutions require special care.

An alternative approach to identifying an initial stimulus to a surface activity is via inverse modeling. In this approach, available measurements or observations are used to constrain the model input. The inverse electrocardiography entails finding the electrical activation on the heart's epicardium (outer wall) from electrocardiogram (ECG) measurements on the torso. For recent advances in this field of electrocardiographic imaging see [34], [13]. Another natural cardiac electrophysiological inverse problem that is less studied is to find the electrical activation inside the myocardium given measurements of the extracellular potential on the epicardium as can be obtained via electrocardiographic imaging [25].

In literature, we can find different methodologies to address the problem of localize ischemic regions using potential measurements taken at the body surface. Several works have analyzed the localization of cardiac ischemia from remote voltage measurements [177]. In [102] the size and position of myocardial infarction is estimated by minimizing the difference between real voltage measurements and model-simulated ones.

The hypothesis behind this thesis is that the analysis of uterine synchronization, which is a phenomenon of great importance for the characterization of uterine contraction efficiency (and thus for the detection of PTL) could give better results when applied to identified sources rather than to surface EHG. We thus have questioned in this work 3 mains aspects: i) the forward problem: which model best represents the links between sources and EHG?; ii) The inverse problem: which method is more suited to the specificity of uterine sources identification?; iii) The synchronization analysis: which method is adapted to the anlysis at the source level? The following chapters will present our approach to answer these questions.

3

Electrohysterogram Imaging (EHGI) and Inverse problem

Contents

3.1 Introduction

The uterine contractility is the direct consequence of the underlying electrical activity in the myometrial cells [3]. The electrohysterogram (EHG) measures the uterine electrical activity (Uterine electromyogram, uEMG) generated by the underlying activity in the myometrial cells, by using a few number of sensors distributed on the mother's abdominal skin [44]. It is a long-standing technique for the analysis of uterine activity that consists in measuring the electric potential on the skin surface with up to an array of sensors. Due to its good temporal resolution, the EHG is used to monitor uterine contraction and has proven to be useful in the clinical evaluation of uterine activity as early as 18 weeks of pregnancy [72].

It has been more recently used as a noninvasive technique to identify uterus activation patterns, which plays a crucial role in contractiliyty. Indeed, it is the only technique with the Magnetomyography (MMG) providing information directly linked to the generation of the uEMG. Performing an accurate localization of EHG sources of uEMG is thus of particular interest to better understand their generation and propagation. We propose in this work to use the imaging of the source of the electrical activity based on inverse source localization from the EHGs [190] to tackle this problem. This technique allows a noninvasive reconstruction of the electrical potential on the uterine surface based on electrical potential measured on the body surface and on anatomical data related to the abdominal conducting volume. This non-invasive modality is used in this study to localize uterus regions involved during the generation of burst of contractile activity. There is a large gap of understanding about how billions of uterine cells contract. Uterine activity originates from excitability and synchronization of myometrial cells. This synchronization could be the result of two phenomena: a) increased connectivity between the myometrial cells, due to the appearance of Gap Junctions, which results in an increase in the local diffusion of the action potentials [44], b) increased sensitivity to mechanotransduction, at the cell level, that permits a longer distance activation of the uterine muscle due to its stretching [186].

Caldeyro-Barcia described their model of uterine function as a wave-like contraction which starts at the fundus, spreads down the uterus, and decreases in strength and duration as it progresses [27]. Wolfs and van Leeuwen [182] estimated a linear propagation. However, there is a significant doubt that myometrial action potentials travel in straight paths. In sheep [136], rodent [98], and human [143] action potentials are not found to travel linearly.

Furthermore the amplitude of Magnetomyography (MMG) signals for physiological uterine activity is expected to range from pico (10^{-12}) to femto (10^{-15}) Tesla (T), depending on the approach of measurement [61]. As mentioned in [103], uterine burst activity give rise to a relatively large amplitude (4.5 pT). This implies that MMG signals are likely to arise from large spatially extended regions of active uterus. Thus uEMG are detectable on EHG/MMG recordings only when associated with a spatially extended uterus generator of several square centimeters. It is thus essential to assess the ability of source localization methods to recover such spatial extent of the sources. Furtherfore, not only it is important to localize the origin of uEMG but also to recover their spatial extent and estimate the temporal course of their activity. This task can become particularly challenging when several distributed regions with highly synchronized activity are simultaneously active or are involved during a propagation process.

Source localization methods may help to determine the regions of the uterus where the activity are generated [190]. Studying the underlying mechanisms and anatomical areas involved in the generation and the propagation of uEMG constitutes a key issue toward a better understanding of the uterus. This process is generally referred to as source imaging and permits to identify the uterus regions that are involved in generating characteristic activity patterns, which is of clinical relevance. Inferring the source location within the uterus from a signal acquired on the abdominal skin, i.e., the EHG inverse problem, is an ill-posed problem since there is a large number of source configurations that can produce the exact same potential at the surface of the abdominal skin. Additional constraints should then be added to obtain a unique solution. Two types of approaches have been proposed [12, 121] in the literature. (1) The equivalent current dipole methods assume that the potentials are generated by a few dipolar sources [93, 159]. (2) The distributed source methods assume that surface potentials are generated by a large number of dipolar sources distributed within source space [43]. Distributed source methods seem appropriate to estimate spatially extended sources. In our work, we aim at localizing myocyte activation on a large number of sources (around 5,000) given few sensors (around 64 or less). The problem is then highly underdetermined and requires additional constraints in the form of a regularization scheme. In this study we add a priori knowledge or constraints by fixing the position of the sources along the uterus surface to achieve linearity in the inverse problem. However, the problem is still under-determined due to the small number of electrodes. In order to obtain a unique solution, additional constraints in the form of a regularization scheme are required. Some mathematical constraints are proposed, such as choosing the minimum energy solution [80] or the maximum of spatial smoothness solution [139]. Statistical frameworks, based on Bayesian inference [174] or entropy [7, 33], Were propose in the state of the art to provide a flexible way of introducing prior information.

Our objective here was to carefully compare different methods, to assess their detection accuracy when extended uterus areas were activated. To do so, we used a common ground-truth fully controlled simulation environment (Figure 3.1).

First, to overcome the accuracy issues when using Boundary Element solutions due to the high conductivity ratio between neighboring tissues (muscle/fat conductivity ratio), we solved the forward problem using Symmetric Boundary Element [95] an extended version of the Green representation theorem [132]. Then, we simulated in this environment different patterns of source configurations varying the number of sources, their spatial properties, and their level of synchronization. We also considered the influence of the number of sensors and used a realistically shaped uterus model. All simulated data were corrupted

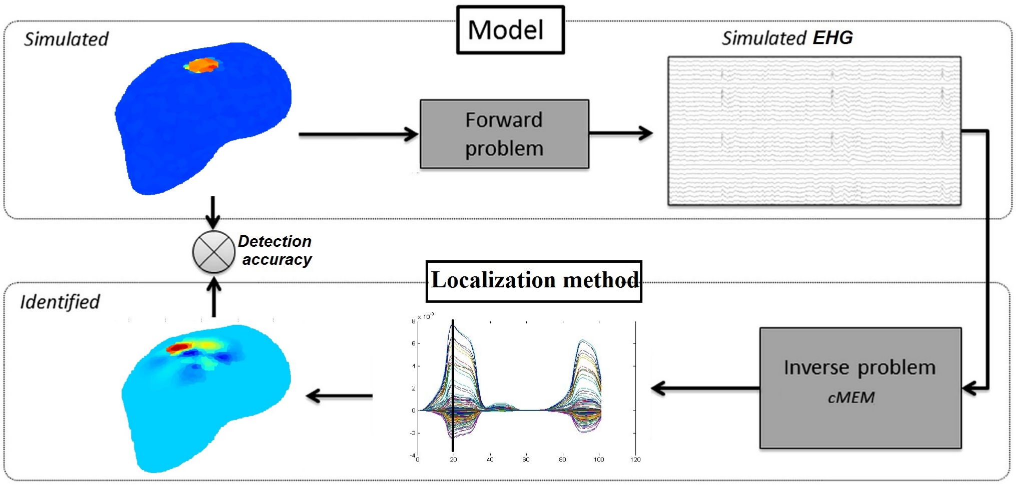

Figure 3.1: Illustration of the study environment: forward model and inverse model in the context of EHG

by averaged physiological EHG noise.

Six source localization methods were thus evaluated and compared, namely: the sloreta [138], the cMEM [32], STWV-DA and STF-DA [15], the Sparse, variation-based source imaging approaches [14]. We quantified the performance of each method by using different criterion permitting to test their performances. Finally, we applied the source localization method to real EHG recordings,.

3.2 Forward model

The electrical activity that can be observed at the surface of the abdominal skin originates mostly from myometrium cells that are primarily located in the middle layer of the uterine wall, consisting mainly of uterine smooth muscle cells (also called myocytes). In order to obtain a signal of sufficient amplitude to be measurable at the skin surface, a certain number of simultaneously active myocyte populations is required. We used in this study an electrical model of these populations developed by our team, based on an Hodgkin-Huxley approach. All details can be found in [185]. The variables of the electrical model are described by the following equations:

$$\frac{dV_m}{dt} = \frac{1}{C_m}(I_{stim} - I_{ca} - I_k - I_{kCa} - I_L) \tag{3.1}$$

$$\frac{dnk}{dt} = \frac{h_{k\infty - nk}}{\tau_{nk}} \tag{3.2}$$

$$\frac{d[Ca]^{2+}}{dt} = fc[-\alpha I_{Ca} - k_{Ca}[Ca^{2+}]_i] \tag{3.3}$$

where Vm is the transmembrane potential , n_K is the potassium activation variable, K_{Ca} is the Calcium extraction factor and $[Ca^{2+}]_i$ the intracellular calcium concentration. The ionic currents are I_{Ca}

for the voltage dependent calcium channel current, I_K for the voltage dependent potassium channel current, I_{KCa} for the calcium dependent potassium channel current and I_l for the leakage current.
For the generation of sources, we consider a number of patches each of which consists of several adjacent cells corresponding to a determined uterus area. Using this electrical model, we created the signals with a sampling rate of 10 Hz for all the cells of each patch (see Figure 3.2 for one example).

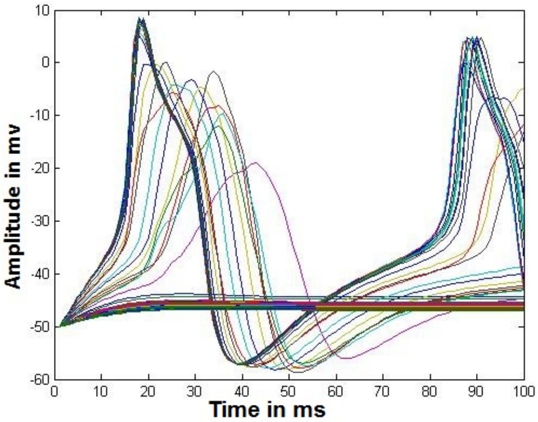

Figure 3.2: Example of signals for the cells in one patch.

The electric potential at the surface of the skin is characterized by the superposition of signals originating from all over the uterus. For modeling purposes, we define a source space that consists of D dipoles located on the uterus surface with a fixed orientation perpendicular to surface. The dipoles are positioned at the vertex of the mesh of the uterus surface. The realistic shape of the uterus has been segmented from a standard 3D MR data set offered to the scientific community by the FEMONUM project [17]. The triangle vertices will later become the source locations. In the same fashion, the compartment borders of skin, fat, and muscle are segmented, subsampled, and triangulated. The obtained thousands of triangles serve as the geometric model for the Symmetric Boundary Element Method used in the forward calculations [76]. The EHG measurements (X $\in R^{N\times T}$) recorded by N electrodes for T time samples, contain a linear mixture of the sources (S $\in R^{D\times T}$) in the presence of noise (N $\in R^{N\times T}$), such that:

$$X = GS + N \tag{3.4}$$

where ($G \in R^{N\times D}$) is the lead field matrix that describes the propagation in the volume conductor and depends on spatial parameters of the model, such as the geometry of the uterus, muscle, fat and abdominal skin as well as their conductivities, and D denotes the number of dipoles. G is estimated using the Symmetric Boundary Element Method (BEM) with the OpenMEEG [76]implemented in Brainstorm software. Based on the realistically-shaped uterus model cited above the forward problem is there solved in a 4-layer realistic model of the volume conductor that contains: the myometrium (where the source is located) with conductivity = $0.2S/m$ (the source are supposed to be located at the surface of the uterine muscle); the abdominal muscle with conductivity $0.3S/m$, and thickness = $0.936cm$; fat with conductivity = $0.04S/m$ and thickness = $2cm$; and skin with conductivity = $0.5S/m$ and thickness = $0.2cm$. With the dipoles of the source space located on the uterus surface and perpendicular to this surface, as said previously, the EHG inverse problem then consists in reconstructing the sources S based on the surface measurements X for a given lead field matrix G (Figure 3.3). However, as the number of dipoles (several thousands) generally exceeds the number of sensors (several tenths), the source imaging problem is ill-posed. In order to restore identifiability of this ill-posed linear inverse problem, additional hypotheses about the sources have to be made. A spatial prewhitening is thus accomplished to decorrelate the source signals, in order to facilitate the separation of the components. This is done by multiplying the data and the lead field matrix by the prewhitening matrix $P = K^{+}$, where K is the square root of the covariance matrix of the background activity.

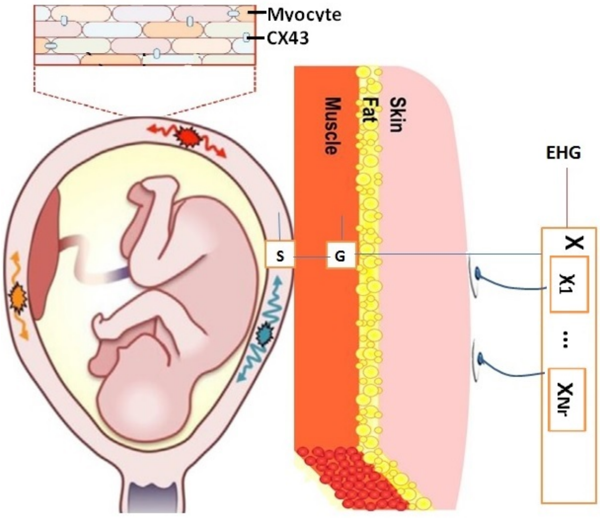

Figure 3.3: The uterus patch is embedded in a volume conductor. As a consequence, S is projected at electrodes (X_1 ... X_{Nr}) placed at the abdominal skin as determined by the leadfield matrix G, which includes the effects of the volume conductor on electrical activity at the uterus level

To test the influence of the recording protocol (number and position of electrodes), we generated data for Nr = 16; 30; 64 electrodes according to different montages of the electrodes, corresponding to different recording protocols used in our team: for the 64 electrodes we used 8,57 mm between the electrodes (Figure 3.4 a), for the 16 electrodes 17,5 mm (Figure 3.4 b) and for the 30 electrodes we used 5.5 cm in the rows and 3.5 cm in the column (Figure 3.4 c).

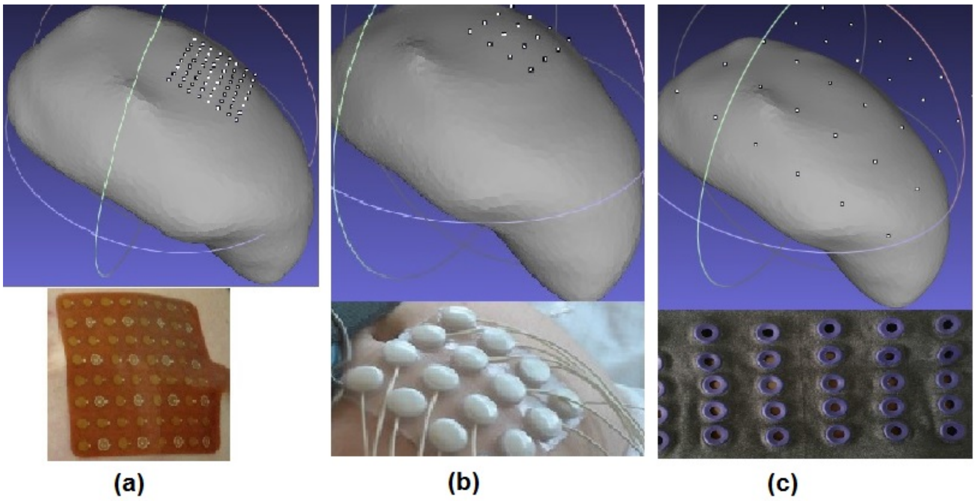

Figure 3.4: Electrodes montage, a) 64 (8.57mm inter-electrodes), b) 16 (17.5mm inter-electrodes), c) 30 (5.5cm x 3.5cm inter-electrodes)

3.2.1 Surface source space

When working with distributed source models, the locations of the dipolar sources need to be specified a priori to compute the forward operator, also known as the gain matrix. This ensemble of dipole locations is called the source space. We assume that each point of the uterus mesh is a source which leads to an average spacing of 3.1 mm between dipoles. The dipoles are oriented normal to the uterus surface (Figure 3.5).

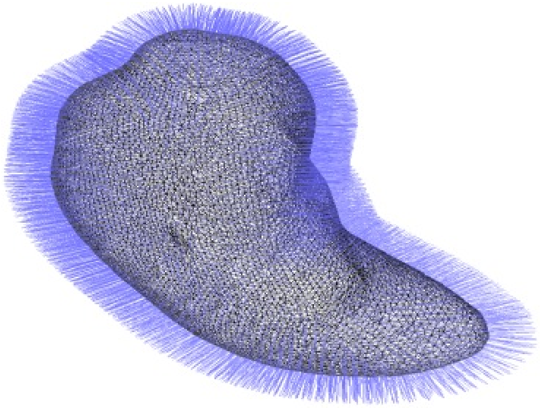

Figure 3.5: Uterus mesh; the blue lines indicate the normal of each dipole.

In order to decrease the computation time of the lead field and of the simulation of sources, we proposed a new algorithm to segment the uterus into different regions (see chapter 5, section 5.6). We thus considered only 5000 dipoles or less instead of the initial 9288 dipoles. In order to simulate extended sources, we then define from these 5000 dipoles, different local patches as illustrated (Figure 3.6). For some localization study, we used 2 different patches separated by either a small distance (interpatch distance= 5cm) or a large distance (interpatch distance= 15cm).

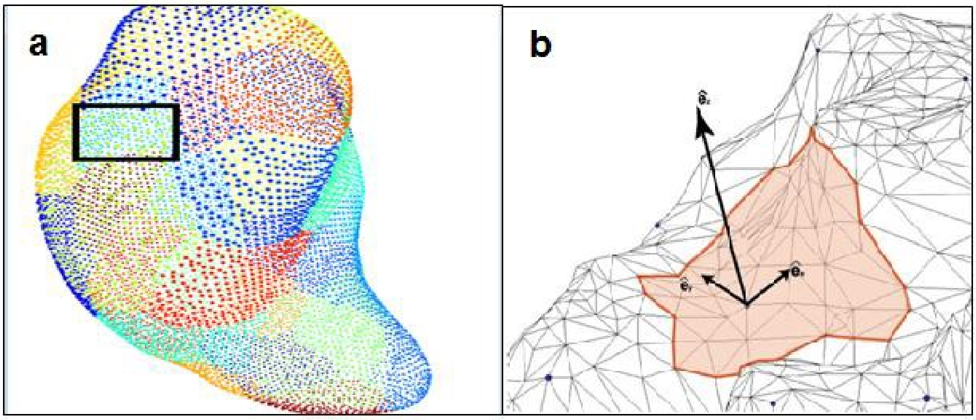

Figure 3.6: a) The black box indicates the region used to introduce the definition of local uterus patch, b) Local patch bounded by the thick red lines. Blue spots denote the locations of the sources after 10-mm decimation. A Cartesian coordinate system with z-direction aligned with the average normal direction is indicated with the black arrows.

Figure 3.7 presents the EHGs obtained with a 4 by 4 electrodes grid. The 16 signals are presented according to their position on the electrode grid. Figure 3.8 shows the Power Spectral Density of the

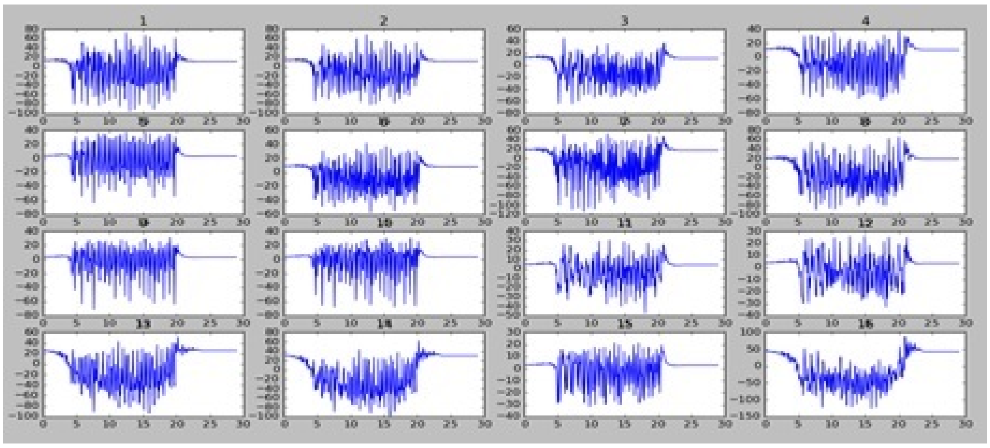

Figure 3.7: Temporal signals of the simulated monopolar EHG signals with a 3D volume conductor.

EHG signals. The Y axis represents the electrode number and the X axis the frequency content. Each noise-free simulated EHG signals were then corrupted by adding realistic physiological noise extracted from a segment of real EHG background activity (figure 3.9).

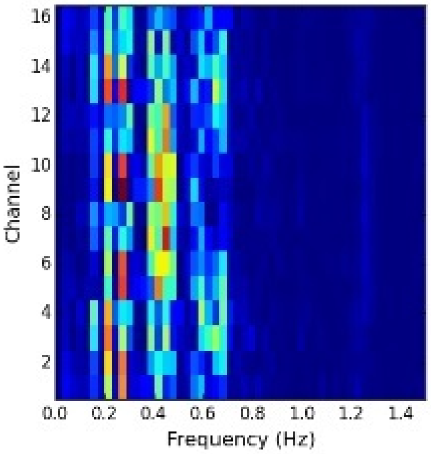

Figure 3.8: Power Spectral Density of the simulated monopolar EHG signals

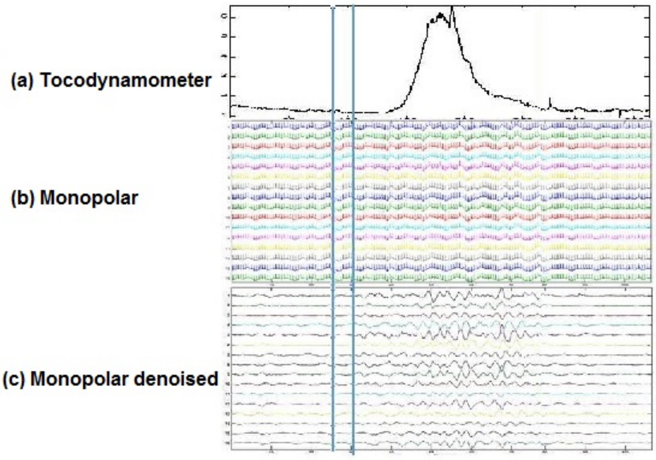

Figure 3.9: Segmentation and Denoising of the recorded EHG signals. (a) TOCO signal used for segmentation. (b) Monopolar EHGs. (c) Monopolar EHGs after denoising. The vertical lines represent the window of segmentation of the baseline used to extract the noise

3.3 Source localisation and extraction

In this work, we compared different methods, extracted from the literature, in order to assess their detection accuracy when extended uterus areas were activated, to simulate uterine sources.

3.3.1 Minimum Norm Estimate (MNE)

Minimum norm estimates are based on a search for the solution with minimum power using the $L2$ norm to regularize the problem, assuming that the solution should be the one providing the minimum energy of the current distribution.

$$\widehat{D}_{MNE} = (G^T G + \lambda I)^{-1} G^T X \tag{3.5}$$

where I is the identity matrix and λ is the regularization parameter.

3.3.2 Weighted Minimum Norm Estimate (wMNE)

The minimum norm is there weighted by a multivariate source prelocalization (MSP) a preprocessing method used to extract some prior information. This is done by introducing a weighting matrix W_S:

$$\widehat{D}_{wMNE} = (G^T W_S G + \lambda I)^{-1} G^T W_S X \tag{3.6}$$

where W_s is a diagonal matrix, $W_S = \frac{1}{APM(i)}$ computed for each source and APM is the activation probability map generated by MSP.

3.3.3 Standardized low resolution brain electromagnetic tomography (sLORETA)

The idea of the conventional sLORETA algorithm [138] consists in standardizing the Minimum Norm Estimte solution for the current density distribution, computed on a voxel grid, by weighting the current dipoles by their estimated variances. This method can be adapted to our data model by replacing the voxel grid by a surface grid that considers only dipoles on the uterus surface with an orientation perpendicular to this surface.

sLORETA [138] uses the source distribution estimated from MNE and standardizes it a posteriori by the variance of each estimated dipole source:

$$\widehat{D}_{sLORETA} = \widehat{D}^T_{MNE,1} \{|V_{\widehat{D}}|\}^{-1} \widehat{D}_{MNE,1} \tag{3.7}$$

where $|V_{\widehat{D}}|^{-1}$ defined as $G^T[GG^T + \lambda I]^{-1} \in R^{N_d \times N_r}$ is the Tikhonov-regularized inverse matrix of G and I denotes the identity matrix of size $N_r \times N_r$.

3.3.4 Transform-based tensor methods

To separate several simultaneously active patches (extended sources) and to reduce the noise on the estimated lead field matrix, we employ a tensor-based preprocessing step. The idea of this method consists in exploiting the structure of the data in 3 different ways. This is done by applying a transform to the two-dimensional measurements (2D space) along time. Under the hypothesis that the resulting data, which depends on three variables, is trilinear (time and 2D space), the tensor W can be decomposed in a unique way (under mild conditions) up to scale and permutation ambiguities, into separate characteristics for each variable with the help of the Canonical Polyadic (CP) decomposition (also sometimes referred to as Parallel Factor Analysis (PARAFAC)). It is thus possible to get an accurate estimate of the spatial mixing matrix or the signal matrix without imposing statistical constraints on sources (unlike Independent Component Analysis (ICA), which may be physiologically difficult to justify.

To get a 3-dimensional data tensor which can be treated by the CP decomposition, one can either compute a transform over time of the electric potential measurements, which leads to the Space-Time-Frequency (STF) analysis, or a transform over space, yielding Space-Time-Wave-Vector (STWV) data. These methods will be described in the subsequent sections.

a- Time-Frequency (STF) analysis

A technique often used for the time-frequency analysis consists in using the wavelet transform of the time signals $x(r, t)$ of the different channels [124]. The resulting three dimension data can then be stored into the data tensor. In order to decompose the tensor W using the CP decomposition, we assume that for each extended source, the time and frequency variables separate, leading to a trilinear tensor. This is approximately the case under the hypothesis of oscillatory signals. The tensor can then be decomposed as:

$$\begin{aligned} W(r,t,f) &= \int_{-\infty}^{\infty} x(r,t)\Psi(\alpha,\tau,t)d\tau \\ &\approx \sum_{p=1}^{R} a(r_i,p)b(t_j;p)c(f_k;p). \end{aligned} \tag{3.8}$$

where r_i, t_j and f_k represent the sampled space, time, and frequency variables and $a(r_i;p)$, $b(t_j;p)$, and $c(f_k;p)$ denote elements of the loading matrices A, B, and C indicating the space, time, and frequency characteristics, respectively. The number of components R corresponds to the number of extended sources. The loading matrix A, containing the spatial characteristics, generally constitutes a good estimate of the spatial mixing matrix $\widehat{H}^{(e)}$. Pseudoinverse of the estimated spatial mixing matrix $\widehat{H}^{(e)}$ is used to obtain an improved estimate of the signal matrix $\widehat{S}^{(e)}$:

$$\widehat{S}^{(e)} = \widehat{H}^{(e)+}X \tag{3.9}$$

b- Space-Time-Wave-Vector (STWV) analysis

Space-Time-Wave-Vector (STWV) is obtained by a 3D local Fourier transform over space accomplished on the measured data. If a local spatial Fourier transform is calculated within a certain region on the uterus, selected by the spherical window function $w(r'\text{-}r)$ centered at a sensor position r, the STWV tensor

$$\begin{aligned} F(r_k, t_l, k_m) &= \int_{-\infty}^{\infty} w(r' - r_k)x(r', t_l)e^{jk_m^T r'}dr' \\ &\approx \sum_{r=1}^{R} a_r(r_k)b_r(t_l)c_r(k_m). \end{aligned} \tag{3.10}$$

is obtained [16], where variable k_m is the wave vector which indicate the direction of the changes of electric potential. Here, $w(r' - r_k)$ is a window function that selects data to the sensor with position r_k for the local transform and $a_r(r_k), b_r(t_l)$, and $c_r(k_m)$, denote the space, time, and wave vector characteristics, which are obtained by the CP decomposition of the tensor.

This analysis requires knowledge of the sensor positions, specified by the matrix r, and of the number of expected sources (corresponding to the number of CP components) R. Several types of window functions can be used, including rectangular, triangular, Hann, and Blackman windows. The radius of the window function is fixed relative to the smallest distance between a pair of adjacent sensors of the EHG matrix and is specified by the variable d. As sensors at the border of the EHG electrode matrix are not surrounded by other sensors that would permit to compute a 3D Fourier transform, these sensors should be excluded from the analysis. To this end, their indices need to be specified by a vector. The tensor is decomposed by using the DIAG (previously called SALT) algorithm [105], [104]. The results of the tensor decomposition yield an estimate of the signal matrix $\widehat{S} = [b_1, ..., b_R]$, describing the temporal dynamics of each source. An estimate of the so-called spatial mixing matrix $H = [h_1, ..., h_R]$, which characterizes the spatial distribution of each source at the sensor level, is obtained as $\widehat{H}^{(e)} = X\widehat{S}(e)+$, where $\widehat{S}^{(e)+}$ denotes the pseudo-inverse of $\widehat{S}^{(e)}$.

$$\widehat{H}^{(e)} = X\widehat{S}^{(e)+} \tag{3.11}$$

c- Disk algorithm (DA)

To localize extended sources based on the estimated spatial mixing matrix obtained by the STWV and STF analyses, we present in this section the Disk Algorithm [15]. In addition to the hypotheses that are made on the structure of the STF or STWV tensor in order to separate the sources, this approach assumes that the measurements can be described by extended sources with a piece-wise constant spa-

tial distribution
The concept underlying the Disk Algorithm consists in recovering the extended source from a number of small circular-shaped patches of grid dipoles, the disks.

The localization of distributed sources is done for each component separately by comparing the spatial mixing vectors $\widehat{h}_r, r = [1, ..., R]$, estimated in the first step, to the spatial mixing vectors associated with a number of potential distributed sources contained in a dictionary .

We refer to this method as the disk algorithm (DA), because we employ circular-shaped regions of varying sizes, called disks, to define the potential distributed sources of the dictionary.

The input of this algorithm is the spatial mixing vector, estimated in the first step, as well as the matrix which characterizes the spatial mixing vector of all disks, that are part of the dictionary. These disks are described by the matrix which contains the indices of the dipoles that belong to each disk.

To determine the disks which best explain the estimated spatial mixing vectors of the sources, a metric based on the normalized inner product between the spatial mixing vector $\widehat{h_r}$ of the r-th source estimated in the first step and the spatial mixing vectors h of the disks is computed:

$$F(\widehat{h}_r, h) = -\frac{(\widehat{h}_r^T h)^2}{h^T h} \tag{3.12}$$

The disks are then ranked according to their metric and the distributed sources are reconstructed by uniting the disks associated with the smallest values of the metric. The output of the DA algorithm is a cell array containing different source estimates obtained by uniting and increasing the number of disks up to a maximal number of disks.

To select an appropriate source configuration among these solutions, a measure referred to as the Goodness-of-fit (GOF) can be employed. The idea consists in choosing the source configuration that minimizes the relative reconstruction error:

$$GOF = \frac{\|X - X_{rec}\|_F}{\|X\|_F} \tag{3.13}$$

where $Xrec = \sum_{p=1}^{P} h_p S_p^T$ corresponds to the data matrix that is reconstructed from the estimated source configuration, which is composed of P source regions. Here, h_p denotes the reconstructed spatial mixing vector of the $p-th$ source region in the estimated source configuration and S_p denotes the corresponding source signal. The source signals $S = [s_1, ..., s_P]^T$ can be computed as $S = \widehat{H}^+ X$ with $\widehat{H} = [\widehat{h}_1, ..., \widehat{h}_p]$.

The patches are localized based on the spatial mixing vectors obtained by the STF and STWV preprocessing using DA. Depending on the tensor method used for the preprocessing, we subsequently refer to these techniques as STF-DA and STWV-DA (Figure 3.10).

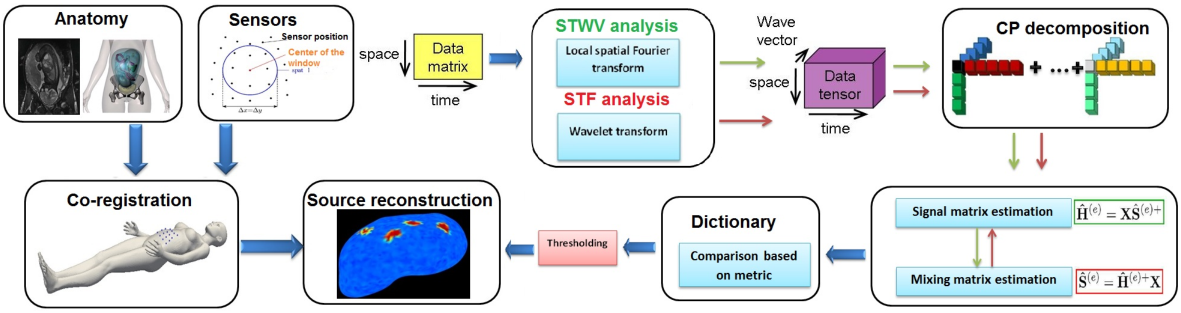

Figure 3.10: Leadfield and signal matrix estimation procedures for the STF and the STWV analyses

3.3.5 Sparse, variation-based source imaging approaches

The variation-based algorithm is a source imaging method based on structured sparsity, which improves the Variation-Based Sparse Cortical Current Density (VB-SCCD) method [14]. More particularly, it imposes sparsity on the variational map and in the original source domain by solving the following optimization problem:

$$\|\mathbf{X} - \mathbf{G}\mathbf{S}\|_F^2 + \lambda(f(\mathbf{V}\mathbf{S}) + \alpha f(\mathbf{S})) \tag{3.14}$$

where the regularizing function f is either the L_1-norm (for SVB-SCCD) or the $L_{1,2}$-norm (for L1,2-SVBSCCD). VB-SCCD optimization problem assumes a piece-wise constant spatial source distribution, and can be regarded as a particular case of (3.14) where $\alpha = 0$. The matrix $\mathbf{V}$ is a linear operator that implements the variational map. For a given mesh of the uterus surface, which defines the source space, this operator can be computed by using the following matrix:

$$V = \begin{bmatrix} v_{11} & v_{12} & \dots & v_{1N} \\ v_{21} & v_{22} & \dots & v_{2N} \\ \vdots & \vdots & \ddots & \vdots \\ v_{P1} & v_{P2} & \dots & v_{Pn} \end{bmatrix}$$

where $v_{ij} = 1$; $v_{ik} = -1$; if the triangles share the same edge, and $v_{ij} = 0$ otherwise. The parameter α determines the size of the estimated source regions and should generally be chosen such that $0 \leq \alpha \leq 1$. The parameter λ determines the overall influence of the regularization term and should be adjusted based on the noise level. Equation 3.14 can be solved by the optimization problem using the Alternating Direction Method of Multipliers (ADMM) algorithm, which is a simple and efficient algorithm for constrained convex optimization. This gain on computational complexity enables us to apply the algorithm to large time intervals and to reconstruct the source signals. Different values for the parameter λ can be given as input to the algorithm and a suitable regularization parameter is chosen automatically from this set of values by selecting the parameter for which $\|\mathbf{VS}\|_0+\alpha\|\mathbf{S}\|_0$ is minimal.

3.3.6 Standard Maximum Entropy on the Mean (cMEM)

The Maximum Entropy on the Mean (MEM) solver is based on a probabilistic method where inference on the current source intensities is estimated from the data, which is the basic idea of the maximum of entropy. The main feature of this method is its ability to recover the spatial extent of the underlying sources. Its solution is assessed by finding the distribution of source intensities to a reference distribution in which source intensities are organized into parcels showing homogeneous activation state. In addition a constraint of local spatial smoothness in each parcel can be introduced [32].

3.3.6.A Realistic Spatial Model using Data Driven Parcellization (DDP) of the uterus surface

We assume that uterine activity can be organized into functional uterus regions. Data Driven Parcellization (DDP) method was used to perform full parceling of the uterus surface into non-overlapping regions at different scales(see figure 3.11). Such a partition at a specific spatial scale s is denoted by $P(s)$. Region growing around each seed points was then iterated until a given spatial neighborhood order s is reached, resulting in a partition of the whole uterus into K regions.

In this DDP approach, we used partial information from Uterine Magnetomyography (MMG) data in order to guide this spatial clustering. The SQUID synchronization data in [146] suggest regions with an area of $64cm^2$. Therefore, on a classical uterine muscle surface the surface area is $1300cm^2$ assuming a perfect sphere (20 to 21 regions) and approximately $1900cm^2$ assuming a more realistic oblate spheroid. Then the number of regions could be around 30, and the global uterine synchronization occurs when the number of regions is $15-30$ while synchronized contractions are inhibited when the number of regions is between 32 and 44 [187]. According to the surface of the used mesh ($1726.59cm^2$), $K=44$, $K=27$ and $K=13$ regions have been chosen in the following result section leading to a mean surface region of $39.24cm^2$, $63.95cm^2$ and $132.81cm^2$ respectively.

Defining uterine activity in terms of K regions of functionally homogenous activity ($K \ll r$) aims at better conditioning the under-determined inverse problem, while the inverse method will infer the local source intensity inside each region.

3.3.6.B Regularization Techniques

To regularize the problem, priori model or assumptions regarding the distribution of the sources j were added to admit a unique solution. In the MEM framework, the amplitude of the sources j is es-

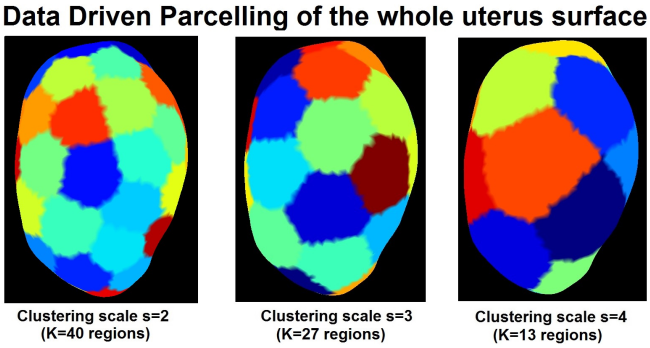

Figure 3.11: clustering of the uterus surface at different spatial scales s obtained using the DDP technique (each color represents one region).

timated as a multivariate random variable. In this study we used the variant of MEM algorithm called coherent MEM (cMEM) implementation, as described in [32]. In cMEM, additional constraint of local spatial smoothness in each region was introducedusing diffusion based spatial priors [60].

We assessed the detection accuracy of cMEM by simulating sources of several spatial extents se ranging from $11.14\ cm^2$ to $59.91\ cm^2$. Secondly, using the spatial model $P(s)$, we assessed the influence of the spatial clustering scale s on their detection accuracy.

3.3.7 Performance Evaluation

3.3.7.A Area Under the Receiver Operating Characteristic(ROC) Curve, AUC:

AUC was proposed in [78] as a detection accuracy index (between 0 and 1), to assess the sensitivity of a source localization method to the spatial extent of the underlying generator. An AUC value greater than 0.8 was considered a good detection accuracy. The AUC index is assessing towards a Ground Truth the normalized energy of a source map at a specific time sample. AUC was estimated based on available Ground Truth, whereby, ROC curves were generated by plotting the sensitivity against the false positive detection rate for different detection thresholds b (between 0 and 1). Normalized energy for both the estimated and the simulated current density distribution were used to quantify the amount of true positive (TP), true negative (TN), false negative (FN), and false positive (FP) for each threshold (Figure 3.12).

$$sensitivity(b) = \frac{TP(b)}{TP(b) + FN(b)} \tag{3.15}$$

$$specificity(b) = \frac{TN(b)}{TN(b) + FP(b)} \tag{3.16}$$

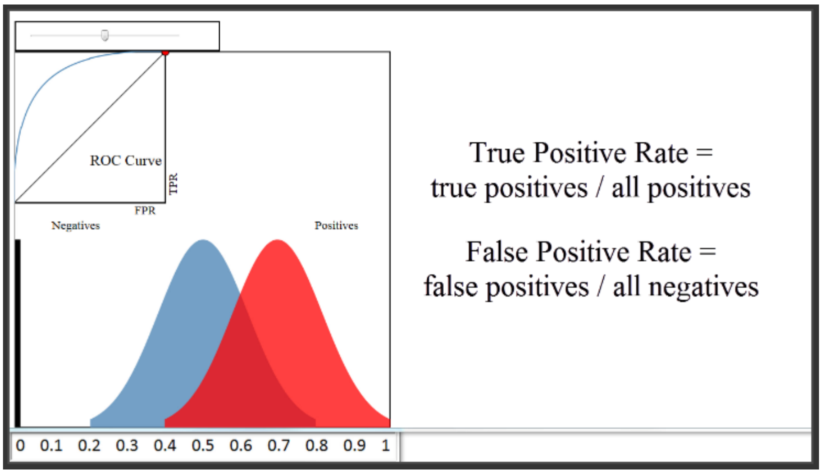

Figure 3.12: Receiver Operating Characteristic (ROC) Curve Analysis [1]

3.3.7.B Dipole Localization Error (DLE)

The Distance of Localization Error (DLE) [31], which characterizes the difference between the original and the estimated source configurations, is defined as follows:

$$DLE = \frac{1}{2Q}\sum_{k\in I}\min_{l\in\hat{I}}\|r_k - r_l\| + \frac{1}{2\hat{Q}}\sum_{l\in\hat{I}}\min_{l\in\hat{I}}\|r_k - r_l\| \tag{3.17}$$

where Q and $\hat{Q}$ are the numbers of original and estimated active dipoles i.e., $Q = \#I$, $\hat{Q} = \#\hat{I}$, and r_k denotes the position of the $k - th$ source dipole.

3.3.7.C Correlation coefficients

In order to analyze the quality of the extracted signals of the different methods, we compute the correlation coefficients between the original and the estimated signals of the uterine activity components. The quality of the extracted signals is evaluated by calculating this correlation coefficients between the estimated patch signal and the averaged signal of all dipoles belonging to a patch. We then compute the mean of the correlation coefficients for all patches.

$$\rho_s = \frac{(s-\mu_s)^T(\hat{s}-\mu_{\hat{s}})}{\|s - mu_s\|_2.\|\hat{s} - mu_{\hat{s}}\|_2} \tag{3.18}$$

3.3.7.D Spatial Dispersion(SD)

This index [125], measures the spatial spread of the estimated source distribution around the true source location. Spatial dispersion (SD) values close to zero means there is no active source outside the simulated patch.

$$SD(\widehat{j}) = \sqrt{\frac{\sum_{i=1}^{r} \left(min_{l\in\phi}(D^2(i,l))\widehat{j}^2(i,\tau_0)\right)}{\sum_{i=1}^{r} \widehat{j}^2(i,\tau_0)}} \tag{3.19}$$

Where $\widehat{j}$ is the result of the source localization method to be evaluated, $\widehat{j}(i,\tau_0)$ represents the amplitude of the current density distribution estimated for a dipolar source i on the uterus surface at the main peak of the spike(τ_0), $min_{l\in\phi}$ (D(i,l)) indicates the minimum Euclidean distance between the source i and the sources l in the simulated patch, ϕ represents the set of indices of the dipoles in the simulated patch.

3.4 Results

3.4.1 Influence of recoding conditions

3.4.1.A Inter-electrodes spacing

An important factor that influences the result of the source localization, and especially the resolution of the localization is the distance between electrodes. In our experiments, to record EHG, we used a grid of 4x4 electrodes with a 17.5 mm electrode spacing [5]. To determine the influence of the inter-electrodes distance on the source localization resolution, we consider the following six distances between electrodes: 5 mm, 10 mm, 17.5 mm, 20 mm, 25 mm, and 30 mm. We used in this analysis two patches parted by 60 mm distance. The corresponding DLE are presented in table3.1. For all inverse methods, 25 mm outperforms all the other distances.

Table 3.1: Performance of source imaging algorithms in terms of Distance of Localization Error (DLE) with different montages of inter-electrodes spacing for two patches with $60mm$ distance, $30cm^2$ area of the patch, $Nt = 100$ time samples with a sampling rate of $10Hz$. The smallest DLE obtained for each methods is marked in red.

Interelectrode (mm)	5	10	17.5*	20	25	30
MNE	3.83	4.14	3.83	3.54	3.50	3.52
WMNE	4.16	4.04	3.99	3.75	3.63	3.69
sLORETA	3.81	3.79	3.71	3.58	3.44	3.95
SVBSCCD	5.37	4.27	3.79	3.05	1.78	2.29
VBSCCD	3.69	3.74	3.66	3.41	2.46	3.38

3.4.1.B Influence of the number of electrodes

Besides the inter-electrodes spacing, the number of electrodes may affect the source localization result. We consider here different electrode numbers: 16, 30 and 64. The corresponding DLE graphs as well as the position of the original patches are plotted in figure 3.13. For these simulations, we used only one patch. The vertex of the mesh located closest to the center of the electrode grid is defined as the ax-index. The patch is placed on the ax-index (figure 3.13a), then 31.28 mm apart from the ax-index (figure. 3.13b), and third 93.5 mm apart from the ax-index (figure 3.13c) to get far gradually from the position of the electrode grid. For the 3 configurations, 64 clearly give better results

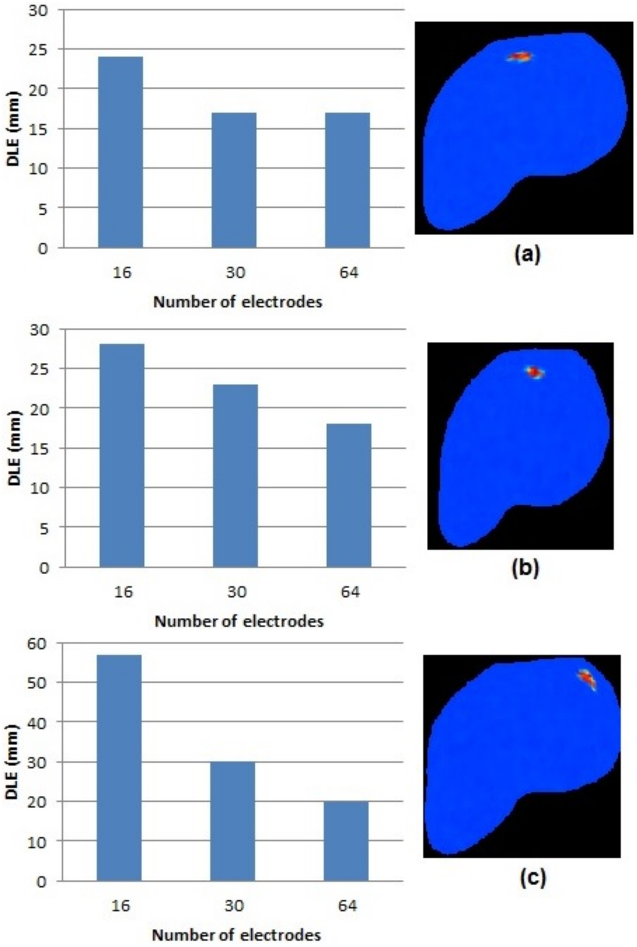

Figure 3.13: Bargraph representation of DLE distribution for 16, 30 and 64 electrodes with three simulated sources (a) patch on the ax-index, (b) patch on 31.28 mm from the ax-index, (c) patch on 93.5 mm from the ax-index. 25 mm of inter-electrode spacing and SVB-SCCD inverse method are used in this simulation, $30cm^2$ area of the patch, $Nt = 100$ time samples with a sampling rate of $10Hz$, $25mm$ Interelectrode distance

3.4.1.C Influence of the fat thickness

As the conductivity of the fat is low, the fat thickness may have a large impact on the source localization performance. We thus studied this point with the following simulations. We conduct a simulation study with one patch placed on the ax-index with different fat thicknesses 3, 8, 13, 18, 23 mm [54]. The resulting DLE and SD curves are displayed in figure 3.14, which evidences an increase in both DLE and SD with increasing fat thickness.

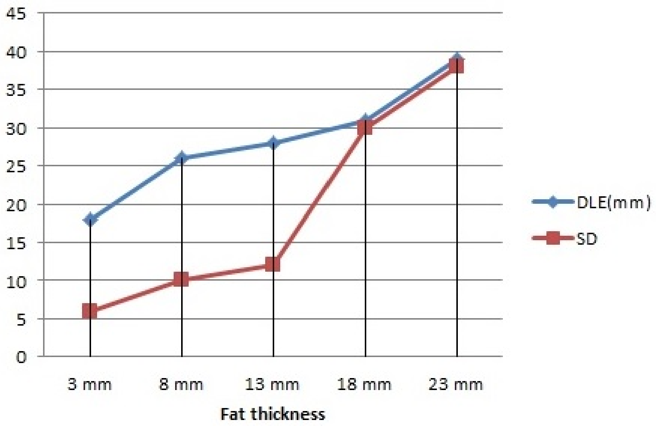

Figure 3.14: Representation of DLE and SD, with the fat thickness. 64 number of electrodes with $25mm$ inter-electrode spacing and SVB-SCCD inverse method are used in this simulation, $30cm^2$ area of the patch, $Nt = 100$ time samples with a sampling rate of $10Hz$

3.4.2 Numerical Experiments of Tensor analysis

3.4.2.A Influence of the SNR

The STWV analysis achieves good performances for SNR greater than 4 dB, reaching correlation coefficients that are higher than 0.8. The best results are obtained for distant patches (distance = 15 cm) whereas the worst results are achieved for close patches (distance = 5cm) . The correlation coefficients of the signals estimated by using the STF analysis do not exceed 0.5 for all tested SNR. In fact, due to the high correlation of the signals of the two synchronous patches, the STF analysis does not manage to separate the sources, which explains its bad performance.

3.4.2.B Influence of the number of time samples

For the STWV analysis, the signal correlation coefficient is approximately the same for all considered lengths of time intervals, meaning that the temporal characteristics of the sources are accurately extracted by the CP decomposition independently of the signal length. However for STF, as explained previously, this method does not permit to separate the sources, due to their correlated signals, and the

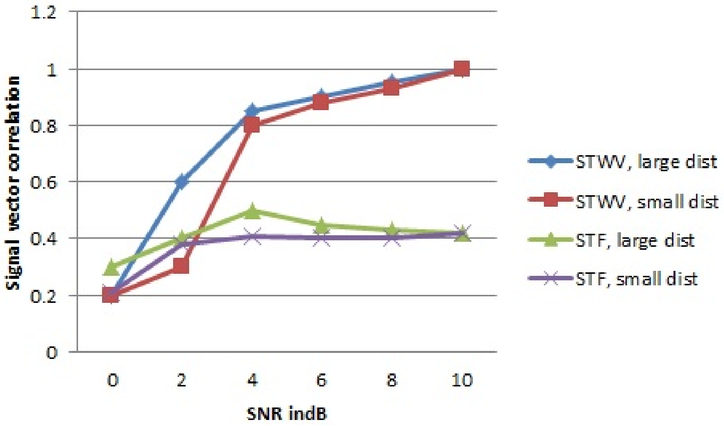

Figure 3.15: Correlation of original and estimated signal vectors for the STWV and STF analyses for patches with large distance and patches with small distance as a function of the SNR for T = 100 time samples, N = 64 sensors, $30cm^2$ area of the patch, with a sampling rate of $10Hz$, $25mm$ Interelectrode distance

accuracy for the estimated source time signals is poor.

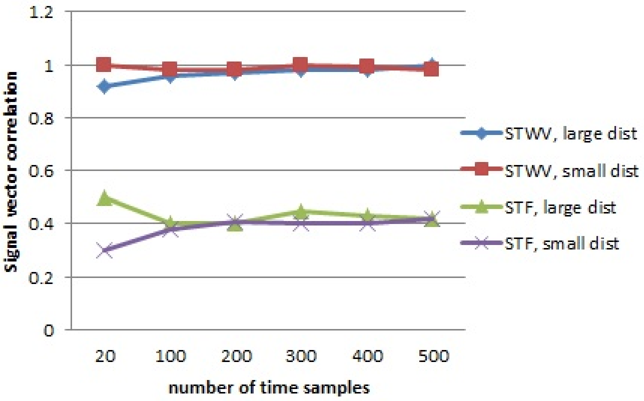

Figure 3.16: Correlation of original and estimated signal vectors for the STWV and STF analyses for patches with large distance, and patches with small distance depending on the number of time samples for a SNR of 4 dB, N = 64 sensors, $30cm^2$ area of the patch, with a sampling rate of $10Hz$, $25mm$ Interelectrode distance

3.4.2.C Influence of the number of sensors

Figure 3.17 presnts the correlation coefficients for different electrode configurations and a SNR of 4 dB. While we observe only a slight increase in the correlation coefficients while increasing the number of sensors for the STF analysis, the performance of the STWV method clearly depends on the number of sensors used to simulate EHGs, specially for the close distant patches.

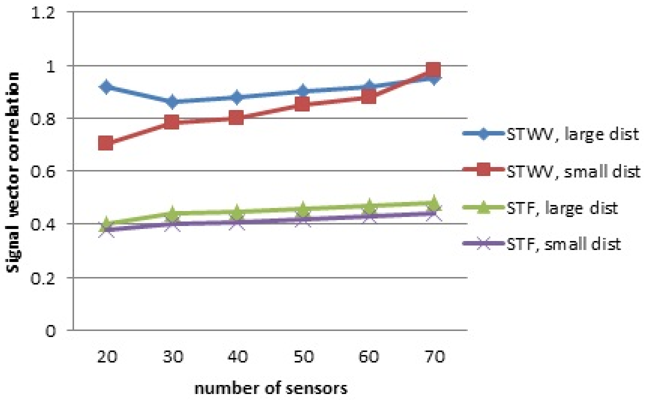

Figure 3.17: Correlation of original and estimated signal vectors for the STWV and STF analyses for patches with large distance, and patches with small distance depending on the number of sensors for T = 100 time samples, a SNR of 4 dB, $30cm^2$ area of the patch, $Nt = 100$ time samples with a sampling rate of $10Hz$

3.4.3 cMEM: Influence of the number of parcels

The performance of cMEM method with the validation metrics AUC and SD for three spatial extents of the source (se= 2, 3 and 4) at different clustering scales (s=15, 10 and 8) are illustrated in figure 3.18. We noticed that the localization accuracy increased when increasing the source spatial extent. We also illustrated the impact of the clustering scale s. We observed an overall very good accuracy (AUC $>$ 0.8 and SD < 29 for all spatial extents) at a clustering scale s=8.

3.4.4 Method selectivity: Influence of patch distance

We compare the performance in term of selectivity of the sources for SVB-SCCD, VB-SCCD, STWV-DA, STF-DA, cMEM and sLORETA. To this end, EHG data are generated for N = 30 electrodes using a realistic uterus and abdomen model with four compartments that represent the uterus, the muscle, the fat and the skin. For the generation of extended sources, we consider a number of patches each of which consists of 20 adjacent dipoles. Highly-correlated uEMG signals comprising 200 time samples with a sampling rate of 200 Hz are created for all dipoles of one patch. The main interest of the methods consists in their ability to separate several simultaneously active patches. An important factor for the distinction of two patches is their distance. This point is therefore studied in the following simulations. To study the influence of the patch distance on the source localization results, we consider in the following three configurations of two superficial patches with large, medium, and small distances, amounting to approximately 15 cm, 10 cm, and 5 cm, respectively. This will permit us to test the spatial resolution of the methods. We used 2 patches that exhibit similar activities with highly synchronized activities. The time courses of the dipoles in the first patch are delayed by several time samples according to the

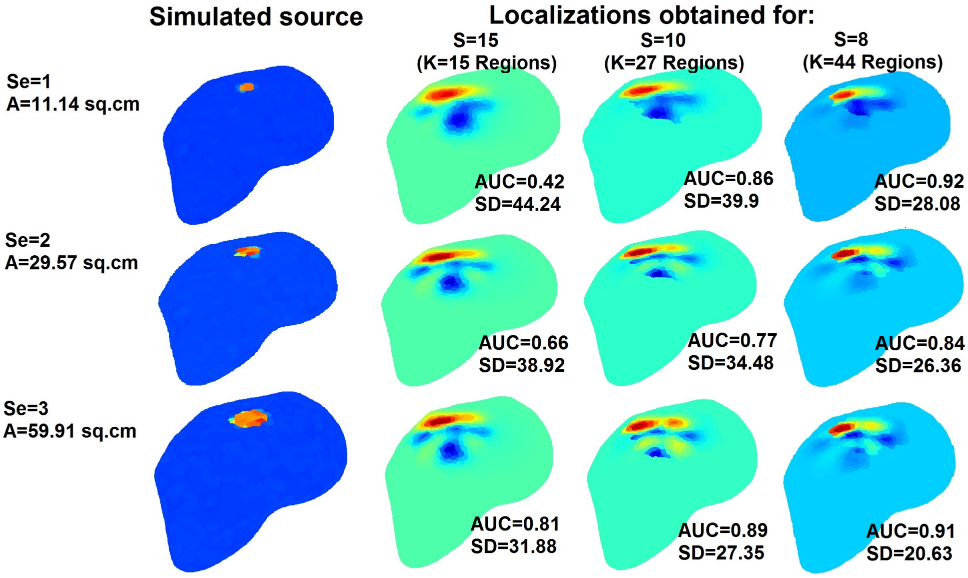

Figure 3.18: **cMEM** qualitative assessment. Visual analysis of source localization results together with Area Under the ROC curve (AUC) and Spatial Dispersion(SD) values for a simulated source of spatial extent se = 2, 3 and 4 at s=15, 10 and 8, $30cm^2$ area of the patch, $N = 64$ sensors, $Nt = 100$ time samples with a sampling rate of $10Hz$

distance between the two patches and attributed to the dipoles in the second patch. Assuming that the other patches are activated due to a propagation of uEMG, we use the same signals for the dipoles of the second patch but introduce a delay, for small distances, a random delay of 5 ms is used for each signal. For medium distances the signals are shifted 13 ms and for large distances, a signal delay of 20 ms is employed. The performance achieved with the different source imaging algorithms for the three scenarios, averaged over 20 realizations with different patch signals (by introducing small variations in amplitude and delay) and noise, is summarized in Table 3.2 and 3.3. The AUC boxplot obtained for the tested source localization methods are plotted in Figure 3.19 for both raw and prewhitened EHG data (The EHG data were spatially prewhitened before applying the source localization algorithms).

In the case where the source imaging algorithms are applied to the raw EHG recordings, for all three patch configurations, the AUC boxplot, the DLE and the correlation coefficient values show that both VB-SCCD and SVB-SCCD clearly outperform all other extended source localization approaches. For two patches (scenario 3), one can observe that SVB-SCCD approach clearly leads to better results than VB-SCCD. The SVB-SCCD approach provides a better separation of the sources than the VB-SCCD approach. cMEM and STWV-DA achieves comparable performances for all three source configurations. They does not permit to recover the patches as accurately as variation-based source imaging methods but perform better than sLORETA. STF-DA exhibiting high DLEs. The localization accuracy diminishes with decreasing source distance. Applying the source imaging algorithms to the prewhitened data leads to an improved performance for all methods. In particular, the cMEM algorithm attains almost the same performance as STWV-DA. STF-DA manages to recover both patches. Furthermore, the AUC boxplot obtained for each method for the three tested scenarios are comparable, which means that the patch distance does not influence the source localization performance in the case of prewhitened data.

Application on real EHGs:

We then applied the best method (SVB-SCCD) to real EHG signals. We used a standard protocol, to record the electrical activity of the uterine muscle. This protocol uses a grid of 16 monopolar electrodes (4x4 matrix) placed on the woman's abdominal skin, with two reference electrodes on each of her hips. The standardized system uses Ag/AgCl electrodes (8mm diameter, with 17.5 mm distance between the centers of two adjacent electrodes). Each window in figure 3.20 represents 20 s of averaged data overlaps with the previous and subsequent windows by 10 s. Hot spots of myometrial activity are seen. Islands of activity appear without activation of neighboring tissue. We could not evidence from these preliminary results any kind of linear propagation of the uterine electrical activity.

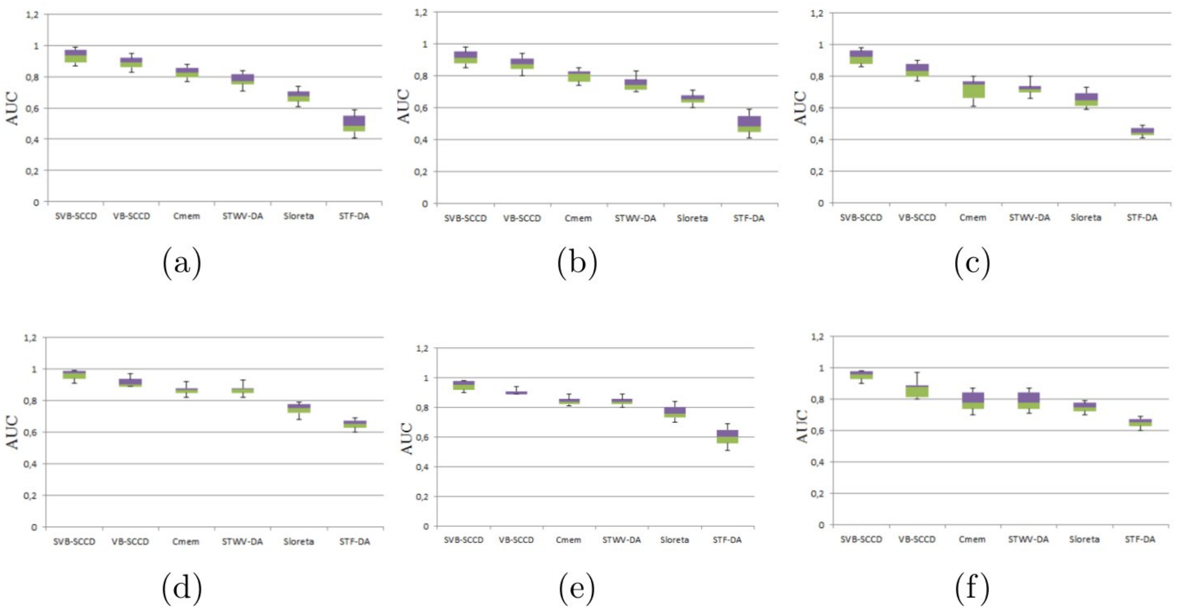

(a) (b) (c)

(d) (e) (f)

Figure 3.19: AUC obtained for different methods applied to raw EHG data (up) and to spatially prewhitened EHG data (down) for three different scenarios composed of two patches with large distance (left), patches with medium distance (center), and patches small distance (right). ($30cm^2$ area of the patch, $N = 64$ sensors, $Nt = 100$ time samples with a sampling rate of $10Hz$)

Table 3.2: Performance of source imaging algorithms in terms of DLE (in cm) and signal correlation for the considered scenarios with large patch distance (1), medium patch distance (2), and small patch distance (3), applied to raw EHG data. ($30cm^2$ area of the patch, $N = 64$ sensors, $Nt = 100$ time samples with a sampling rate of $10Hz$)

	DLE			Correlation coefficient %		
Scenario	1	2	3	1	2	3
SVB-SCCD	0.12	2.12	3.01	96.6	93.2	90.09
VB-SCCD	0.14	2.9	5.9	95.1	91.2	80.9
cMEM	4.2	5.34	6.3	75.3	73.4	72.3
STWV-DA	6.43	8.3	12.4	71.44	68.11	60
STF-DA	25.16	20.67	17.4	47.5	52.6	55.67
sLORETA	10.56	12.54	17.8	65.43	59.8	54.89

Table 3.3: Performance of source imaging algorithms in terms of DLE (in cm) and signal correlation for the considered scenarios with large patch distance (1), medium patch distance (2), and small patch distance (3), applied to spatially prewhitened EHG data. ($30cm^2$ area of the patch, $N = 64$ sensors, $Nt = 100$ time samples with a sampling rate of $10Hz$)

	DLE			Correlation coefficient %		
Scenario	1	2	3	1	2	3
SVB-SCCD	0.98	1.4	2.59	97.65	95.41	92.5
VB-SCCD	0.99	1.9	3.2	96.4	94.7	90.52
cMEM	3.4	4.01	4.55	85.4	83.34	81.6
STWV-DA	3.3	4.23	4.7	85.7	83.23	81.17
STF-DA	13.16	12.67	10.15	56.9	59.4	65.88
sLORETA	5.67	8.9	11.12	76.45	75.6	72.42

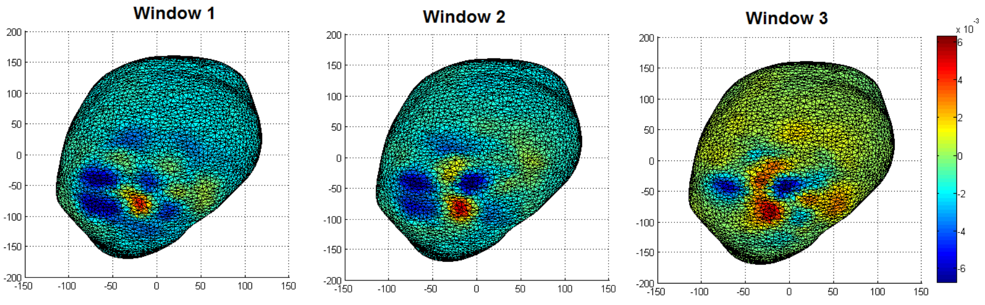

Figure 3.20: EHG source imaging using SVB-SCCD inverse method of pregnant contraction recorded by 16 electrodes. Each window represents 20 s of averaged data.

3.5 Discussion and Conclusion

We have investigated the relationship between the source localization, and some experimental parameters: the number, distance of electrodes and the fat thickness. It was proved that the source localization benefitted from an increased number of electrodes and that an optimal electrode spacing (25mm for an inter-patch distance of 60mm) exists. We have also shown that an increase in the fat thickness leads to larger DLE and SD values. This may be related to the fact that, with increasing fat thickness, the electrode get farther away from the true source that are contributing to the estimated solution. Thus the diffusion process due to the low conductivity of the fat impedes the localization accuracy.

We demonstrated using Data Driven Parcellization of the uterus surface is particularly relevant to localize uterine sources as well as their spatial extent. The possibility of locating the sources of the uterus is likely to give new information on the synchronization of activity of the whole uterus.

We have conducted our analysis using a realistic uterus model and have aimed at identifying the spatial extent of the sources. The computer simulations have shown that both SVB-SCCD and VB-SCCD exhibited the best performance, which permits to simultaneously localize several highly correlated active source regions. They appear therefore to be of the most promising approaches for the identification of multiple active uterus regions in the context of propagation phenomena. Nevertheless, the VB-SCCD algorithm shows some difficulties in separating sources. The SVB-SCCD method permits to obtain more focal source estimates than VB-SCCD and achieves the separation of even closer sources, which leads to an increased performance in terms of signal extraction, due to the additional regularization term that imposes sparsity in the original source domain. We have also analyzed the use of tensor-based methods which separate the sources prior to the localization. STWV method accurately separated the patches and exhibited good performance. This can be explained by the fact that the STWV analysis correctly separates the spatial mixing vectors of the two patches and therefore permits to localize each patch individually. In particular, STWV-DA has proven to be robust if applied to the raw EHG data with no prewhitening, contrary to the other tested source imaging algorithms, which, for patches with medium to small distances, only lead to good results in the case of prewhitened data. However, the tensor-based methods do not provide accurate results for the correlated sources in case of the STF analysis due to the highly correlated signals of the two patches (Due to propagation effects, the source signals can be expected to be highly correlated), which differ only by a small time delay. The STF analysis is therefore unlikely to separate the sources, therefore impeding source localization. This poor sensitivity may be explained by the inability of the STF analysis to identify components that can be associated to different patches because the time-frequency content of the simulated patch activities is nearly identical. The time signals of the different sources should not be too correlated to be properly identified by this method.

Low correlations facilitate the source separation. STWV-DA does not yield as accurate results as cMEM for the raw EHG data. Nevertheless, employing prewhitening improves the source localization results obtained by STWVD-DA, leading to a performance that is similar to STWV-DA in this case. sLORETA generally do not permit to achieve as accurate results as cMEM.

When applying SVB-SCCD inverse method to real signals, our analysis of the evolution of the real sources during contraction showed a non-linear propagation, appear to propagate slowly in tissue, in complex pathways and noncontiguously.

This result promotes the hypothesis that another mechanism than the only electrical diffusion, permits the global uterus synchronization. In future work we would like to go deeply to the clinical applications (estimating the sizes of the regions and analysing the synchronicity between them), in order to improve our knowledge concerning the uterine synchronization.

4

EHG Source Connectivity

Contents

4.1 Introduction

Noninvasive EHG source connectivity is a technique to identify functional uterine networks at uterus level from noninvasive recordings.

Studying the global synchronization of the uterus at the source level, by using noninvasive signals (recorded real EHGs) could be a very important tool for clinical purpose. Imaging techniques could be used to identify uterus networks involved in pregnant uterus functions as well as in labor. A number of studies performed at the level of electrodes reported that electrohysterogram (EHG) associated with appropriate signal processing techniques might bring relevant information about normal networks activated [130]. Indeed, this interpretation is not straightforward as signals are severely corrupted by the effects of volume conduction. To overcome these difficulties, we apply connectivity methods on the temporal dynamics of uterus sources reconstructed from surface EHG. This approach includes two steps (EHG inverse problem followed by source connectivity estimation). However, it raises a number of methodological issues. First, it requires to solve the ill- posed EHG inverse problem. Second, a functional connectivity method must be chosen among the many available ones. A central issue is the impact of selected methods (EHG inverse solution and connectivity measure) on the topological/statistical properties of identified uterine networks. Regarding the first aspect, several approaches have been proposed to solve the EHG inverse problem, some efforts have been done to evaluate inverse algorithms in the view of localizing the uterus sources [190]. For the purpose of this study, we retained three functional connectivity methods based on linear cross-correlation (R2) [20], nonlinear regression (h2) [142, 178], coherence function [19].

In this study, we report a quantitative comparison of methods aimed at identifying uterus networks from surface EHG data. In addition, our comparative study includes simulated EHGs generated from realistic computational model uterine sources.

To characterize precisely connectivity matrices and quantify the global uterine connectivity, we used an analysis based on the graph theory. This field has shown a growing interest in the last years, especially to characterize uterus networks [24, 130, 156]. According to this approach, a connectivity matrix can be represented as graphs consisting of a set of nodes interconnected by edges.

In this study, we analyze the impact of the combination between the algorithm used to solve the EHG inverse problem and the algorithm used to measure the functional connectivity. We evaluate three inverse solution algorithms and three connectivity measures, on data simulated from a 3D model that generate realistic uterine EHG recorded in woman's abdomen. We used a network-based similarity index to compare between the network identified by each of the inverse/connectivity combination and the original network generated by the model.

The chapter is organized as follows. The connectivity and inverse algorithms we retained for evaluation are described in the methods section. Results obtained from the quantitative comparison of analyzed methods are then presented. They show that fairly different networks are identified from the same EHG data set when different methods are being used. However, they also suggest that the combinations (inverse + connectivity methods) could lead to the identification of networks topologically close to the expected ones.

4.2 Materials and methods

4.2.1 Data generation

The EHG signals recorded at the abdominal skin surface mostly reflect the activity of myometrial cells within the uterus. We model these activities by using a realistic model developed in our team, to simulate EHGs. This model permits us to control the number, position and activity of the uterine sources (network of sources) used to simulate the EHGs, as described previously. Each noise-free simulated EHG signals were then corrupted by adding realistic physiological noise extracted from a segment of real EHG background activity (figure 4.2). We generated by using this model different networks by creating different sources which connectivity are known (ground truth network). This ground truth will then be compared with the estimated network.

4.2.2 Inverse solutions

We chose in this work to compare 3 inverse methods: wMNE, cMEM and SVBCCD. We retain wMNE as a a classical inverse method, SVBCCD because this method gave the best results for source localization in the previous study and cMEM that perfomed well on raw data (with no prewhitening).

4.2.3 Connectivity measures

For the purpose of this work, we selected three methods that permit to estimate the functional uterus connectivity from electrophysiological signals. These 3 methods are the ones that were selected in Nader's preliminary work [129].

4.2.3.A Cross-correlation coefficient (R^2)

This is one of most classical measures of interdependence between two time series [8]. The cross-correlation coefficient measures the linear correlation between two variables X and Y in the time domain as a function of their time delay (t). The estimation of this coefficient for the two-time series X(t) and Y(t) is performed by using the following equation:

$$R^2 = \max_{\tau} \frac{cov^2(X(t), Y(t+\tau))}{(\sigma X(t)\sigma Y(t+\tau))^2} \tag{4.1}$$

where σ and cov denote the standard deviation and the covariance, respectively. R^2 ranges from 0 (X and Y are independent) to 1 (Y is a linear function of X).

4.2.3.B Imaginary part of coherence ($Icoh$)

The coherence (C) function gives the linear correlation between two signals X and Y as a function of the frequency [135]. It is defined as their cross-spectral density function C_{XY} normalized by their individual auto-spectral density functions C_{XX} and C_{YY}. The imaginary part of coherence ($Icoh$) is then defined as:

$$Icoh = \frac{|ImC_{XY}(f)|}{\sqrt{|C_{XX}(f)|\,|C_{YY}(f)|}} \tag{4.2}$$

$Icoh$ varies between 0 (X and Y are independent) and 1 (X and Y are fully correlated). This new connectivity analysis will be tested in this work and compared to the previously used method. To quantify the connectivity computed with these different methods over the whole matrix of EHG signals, we will use the graph theory approach.

4.2.3.C The nonlinear correlation (h^2)

In practice, to estimate the nonlinear correlation coefficient h^2, we study a scatter plot of Y versus X. We subdivide the values of X into bins; for each bin, we calculate the average value of X (pi) and the average value of Y (qi). The regression curve is approximated by connecting the resulting points $(pi$, $qi)$ by straight line segments [140]. Then, the nonlinear correlation coefficient between the two signals X and Y is calculated as follows:

$$h^2_{Y/X} = \frac{\sum_{k=1}^{N} Y(k)^2 - \sum_{k-1}^{N}(Y(k) - f(X_i))^2)}{\sum_{k-1}^{N} Y(k)^2)} \tag{4.3}$$

The estimator $h^2_{y/x}$ ranges from 0 (Y is independent of X) to 1 (Y is fully determined by X) and the nonlinear correlation coefficient is asymmetrical so $h_{y/x} \neq h_{x/y}$ and thus permits to give information on the direction of the information. This asymmetry feature is not explored in our work as we are interested only in the presence or not of a nonlinear relationship between two signals. To quantify the connectivity computed with these different methods over the whole matrix of EHG signals, we will use the graph theory approach.

4.2.4 Graph analysis

The “Graph theory” started with the scientist Euler in 1936 when he tried to find a solution for the question: “What is the best path across the seven Köningsberg bridges?” [18]. This path that was called later “Eulerian path” should cross over each of the seven bridges exactly once. From such problems, the field of graph theory has developed numerous algorithms that can be applied into many domains. Later on, this approach has been largely used in several fields such as biological system, internet networks and social groups [133].

Several metrics can be extracted from a graph network to quantify its connectivity. We chose in this work to use the strength parameter that provided the best results in : Nader’s results [129].

The strength shows the importance and the contribution of each node with respect to the rest of the network. The strength of a node is the sum of the weights of the edges connected to this node and can be defined as:

$$S_i = \sum_{j \in N} w_{ij} \tag{4.4}$$

where i, j denotes respectively the ith , jth nodes and wij is the value (weight) of the relation between nodes i and j [156]. The average strength value over all the nodes can be also computed, indicating the overall characteristic of the network.

4.2.5 Proposed approach

The different steps of our analysis of the connectivity at the source level are summarized in figure 4.1 and figure 4.2. In step 1, the lead field matrix G was computed as previously explained (chapter 3). The distributed source space consisted in a mesh of the uterus surface (5000 vertices). Dipoles were located at each vertex of this mesh. The time-course of each dipole of the source space was generated from a physiologically uterus model reported in [185], that permits the simulation of uterine electrical activity with well-controlled time shifts. We considered in this work two interconnected networks. The temporal dynamics of the second network were highly correlated with those of the first one, but with a minor delay (50ms). This delay was usually interpreted as reflecting propagation between distant regions in the uterus. 20 trials of 40s at 200 Hz containing 30 uterine spikes were simulated. Each trial was obtained for a new realization of the input random noise leading to a new realization of uterine spikes.

In step 2, the temporal dynamics of dipolar sources D were estimated from simulated surface EHG signals S(t). The three above-described methods (wMNE, cmem, svbccd) were used to estimate D, the highest energy sources. The uterus surface was parcellated into 1000 regions of interest (ROI). Then, in step 3 the functional connectivity among uterus sources was computed using the 3 methods described above (R2 , h2 and Icoh). The strength of all nodes of the connectivity matrix was then computed. A thresholding procedure was then applied on the functional connectivity values in order to retain only the strongest functional connections. On all connectivity matrices (1000 x 1000) we computed the strength of each node. We kept nodes with the highest 1% strength values. The same threshold was applied on the connectivity matrices for all combinations (inverse/connectivity).

Finally, in step 4, the performance of each method (source reconstruction+functional connectivity) was evaluated against its capacity to identify a network topologically close to that expected. For this purpose, we used a criterion based on the simNet algorithm [120]. The main advantage of this algorithm is that it takes into account the spatial location (3D coordinates) of the nodes when comparing two networks. The algorithm provides a normalized Similarity Index (SI) between 0 (totally different graph) and 1 (same graph). A Gaussian noise was used as external input.

We used the matlab based Brain Connectivity Toolbox (BCT) for the calculation of graph parameters [156]. For the simulated data, we used Python programming language using the Pycharm Edu 2.0.3 software (www.jetbrains.com). For the network visualization, we used mayavi toolbox on the same software.

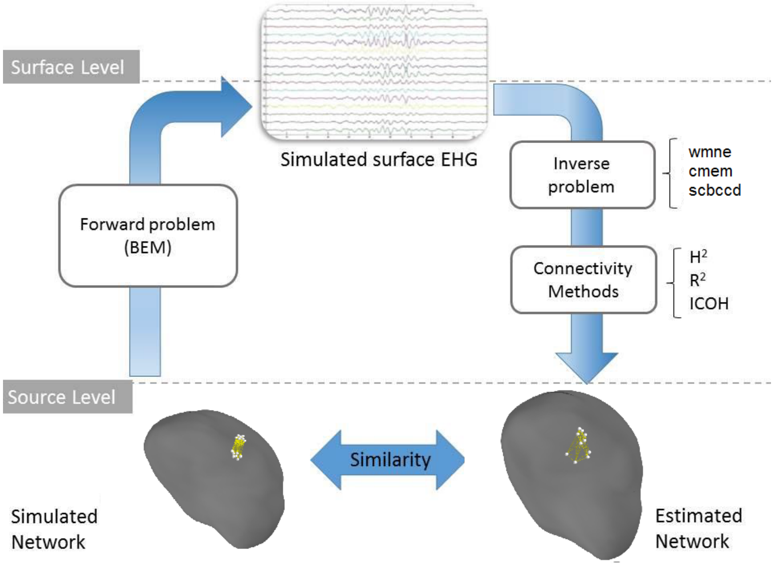

Figure 4.1: Identification of uterus network: first, a network is generated by the model and considered as the ground truth. By solving the forward problem, synthetic EHG data are generated. These signals are then used to solve the inverse problem in order to reconstruct the dynamics of sources using three different inverse solutions (wMNE, svbccd and cMEM). The statistical couplings are then computed between the reconstructed sources using three different methods (r2, h2 and Icoh). The identified network by each combination (inverse/connectivity) was then compared with the original network using a network similarity

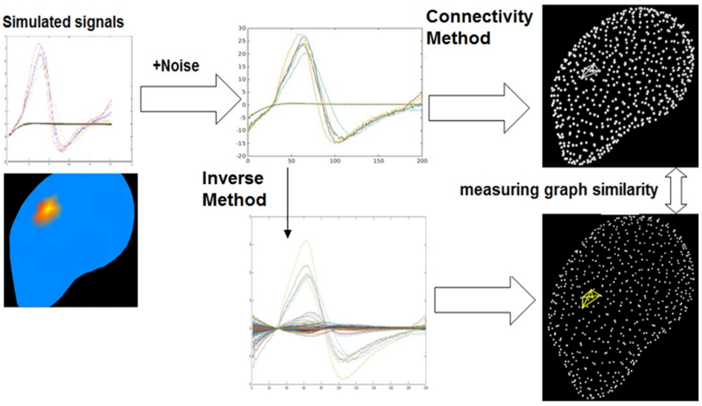

Figure 4.2: Ilustration of the simulated signals in each step

4.3 Results

A typical example of the connectivity graphs obtained for the 9 different combinations of the source reconstruction and functional connectivity methods is presented in figure 4.3. The qualitative visual inspection of the identified networks shows that results are highly dependent on the both chosen algorithms used to solve the EHG inverse problem and to measure the functional connectivity. The qualitative analysis also showed that the number of nodes and the connections between them varied according to the combination of methods used. Quantification of these differences is provided in Fig. 4.4c. Overall, values of network similarity ranged from 55 to 69 %. The combination providing the highest similarity values between the estimated and the actual network was scbsccd/ h2 (69 %) followed by scvbsccd/Icoh (65 %) and wmne/r2 (61 %). The lowest similarity value was obtained with the cmem/Icoh combination. For labor data case, we can notice, as expected, an increased synchronization among interconnected myometrium populations distributed over distant areas. This synchronization often leads to an increase in uterus connectivity more evident than during pregnancy (4 weeks before labor), as shown in figure 5.6.

4.4 Discussion and conclusion

Identifying uterus networks from noninvasive EHG data is a challenging issue. The joint use of these two approaches (source localization combined with functional connectivity analysis) is still novel and raises a number of methodological issues that should be controlled in order to get appropriate and interpretable results. In this study, we presented a comparative analysis of the results obtained from the possible combinations between three algorithms to solve the EHG inverse problem and three methods to estimate the functional connectivity. The connectivity matrix was then quantified by a graph parameter, the strength.

The results show that the choice of the inverse algorithm and the connectivity method is crucial and can strongly alter the results and their interpretation. It is remarkable that starting from the exact same EHG recordings, different networks can be identified. An originality of this study is related to the use of EHG signals simulated data from a realistic model as a ground truth for comparing the performance of considered methods. By proposing a quantitative comparison procedure, we were able to retain one combination that showed the best performance in identifying the uterus networks. Overall results obtained on simulated data indicated that the combination of the scbsccd and the h2 methods leads to the most relevant networks as compared with the ground-truth (simulations) (similarity index of 0,7). These results outperform the ones obtained when using a simple approach and classical methods, as done in Nader's preliminary work [129] were the highest value obtained by this similarity index was around 0,3.

The connectivity matrices were thresholded by keeping the nodes with highest strength values (strongest 1%). This procedure was used to standardize the comparison between all the combinations. The threshold of 1% was chosen as the one giving the best results, after testing several values of the threshold. In the previous work [129], the threshold was 10%. But they worked with 16 regions. Here we worked with 1000 regions and we activate the nodes directly below the electrodes.

EHG source connectivity can be a valuable method to identify uterus networks. However, results are highly dependent on the choice of processing methods.

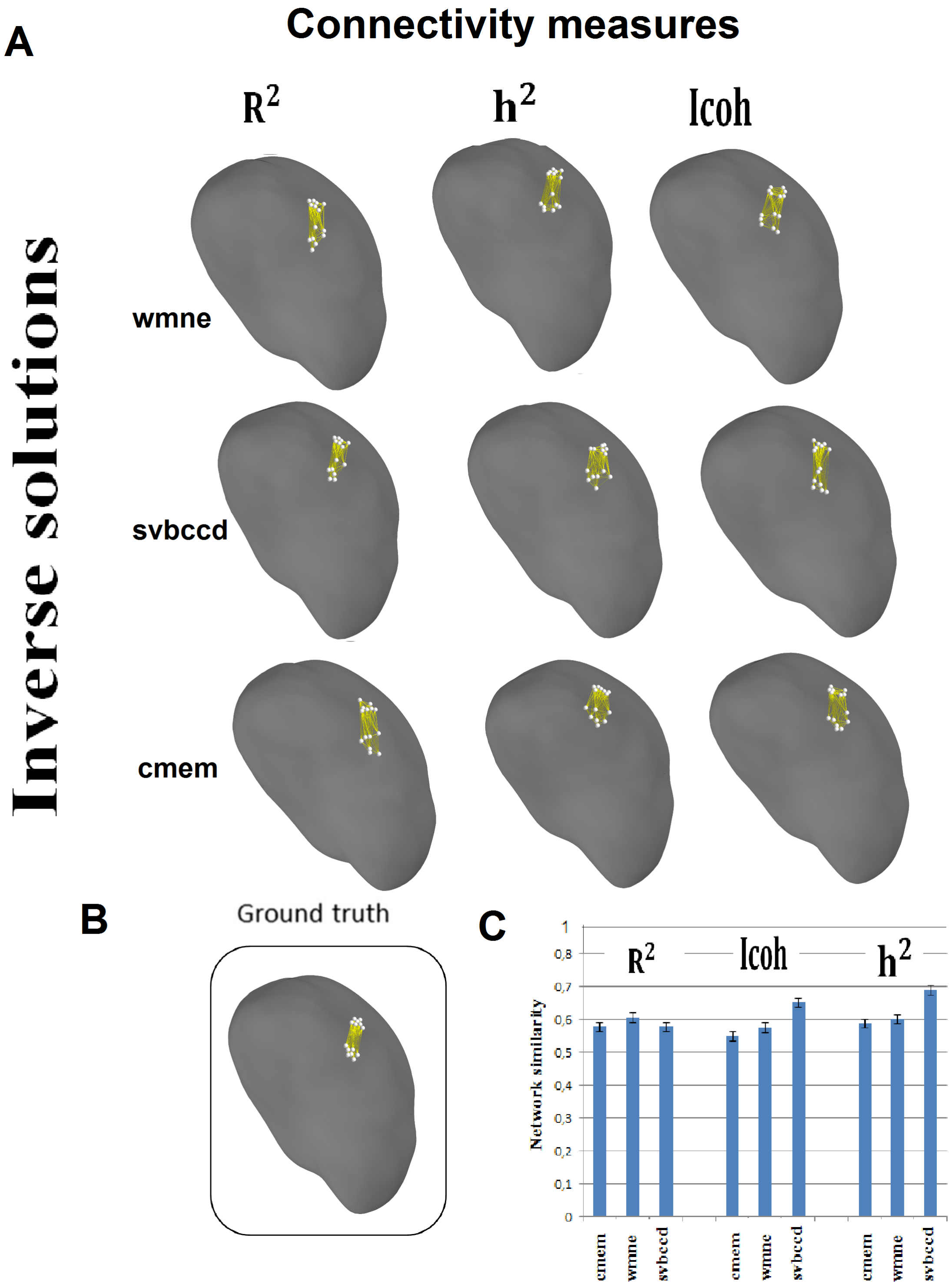

Figure 4.3: Two networks scenario. (a) uterus networks obtained by using the different inverse and connectivity methods. (b) The original network (ground truth) is shown and (c) values (mean ± standard deviation) of the similarity indices computed between the network identified by each combination and the model network

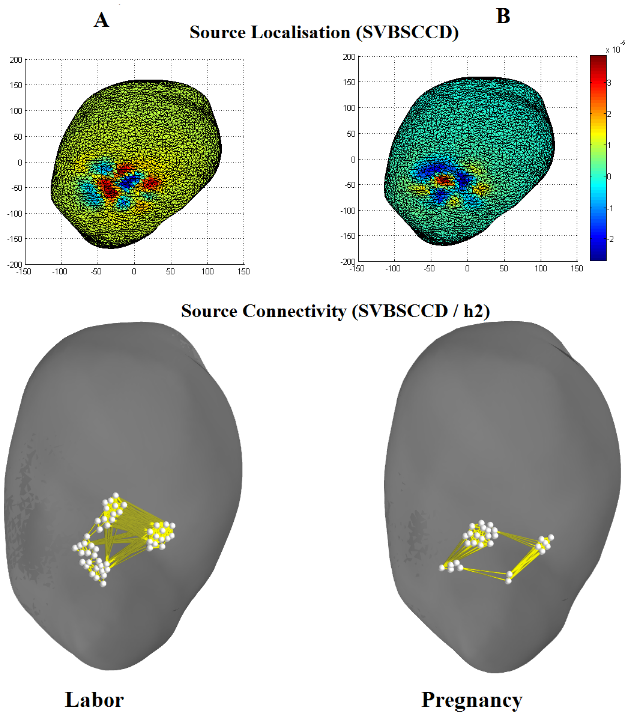

Figure 4.4: Results obtained by the network-based approach (SVBCCD/h2) Results obtained by the localization based approach (SVBCCD). Results were averaged over a 50 ms interval around each of the spike peaks. Red color represents the sources with the highest energy. A. Results for labor EHG signals, and B. Results for 4 week before labor EHG signals

5

Forward problem: The Computational Model

Contents

5.1 Introduction

Biosimulation models of the uterus electrical activity have become a very useful tool. It provides better understanding for the complex biophysical phenomena related to the contractility of the uterus such as uterine contractions during pregnancy. At cellular level, the electrical activity of uterus tissue may be simulated by solving a system of Ordinary differential equations (Ordinary differential equations (ODEs)) describing the electrical behavior of the cell membrane. Because the biophysical processes underlying this phenomenon are non-linear and change very rapidly, the ODE system is a challenge to be solved numerically. Furthermore, the implementation of these models is a hard task for commercial finite element software. In this study we conducted a finite element formulation, model and code generation, for monodomain and bidomain equations. The developed code is coupled with the Red3 cell electrophysiological model already developed [96] in order to have isotropic excitation propagation starting from the cell to the complete uterus levels. Fenics was used to build the proposed finite element code.

Uterus tissue can be viewed as connected cells (myocytes), organized and tethered through an extracellular matrix to produce the contraction of the uterus. The currents underlying the propagation of the electrical activity from cell to cell flow across the cell membrane (Gap Junctions) and through both the intracellular and extracellular spaces in the uterus (Figure 5.1). Over the past 30 years there has been considerable interest in the structures that couple the intracellular spaces of myocytes to one another [35]. Myometrial cells are coupled together electrically by gap junctions composed of connexin proteins [67]. The increase in gap junction number, and the resulting facilitated electrical transmission, provide better coupling between the cells resulting in synchronization and coordination of the contractile events of the connected cells. There is evidence that gap junctions form a pathway for the passage of action potentials by forming a low-resistance electrical contact between the cells [122], [66]. Many studies indicated that during most of pregnancy phases, the cell-to-cell gap junctions are absent or present in very low density [66]. On the other hand, a large number of gap junctions between myometrial cells is observed during labor [63].

The other component of the intracellular resistance is determined by the micro- and nanostructures inside the cell itself. Like most muscle cells, uterus myocytes contain contractile proteins: actin and myosin. Contraction of smooth muscle cells happens due to the interaction of myosin and actin filaments. The key enzyme is the myosin light chains kinase (MLCK) which, activated by the complex Ca^{2+}- calmoduline $(Ca^{2+} - CaM)$, phosphorylates the myosin light chain LC20. It is in this phosphorylated form that myosin can interact with actin and cause contraction. The fall in the concentration of intracellular calcium $\left[Ca^{2+}\right]_i$ leads to relaxation: the dephosphorylated myosin, by the action of a specific phosphating, then detaches from the actin. Furthermore, phosphorylation of MLCK causes a decrease in its ability to activate myosin and thereby to produce the contraction. This activation pattern

(related to depolarization followed by repolarization) is well established in vitro but does not always seem to be strictly followed in vivo. In addition, the relative importance of different control channels varies according to whether it is a spontaneous contractile activity or that caused by extracellular signals. Some animal studies suggest the existence of other regulatory pathways involving protein kinase C (PKC) and the fine filament proteins, the caldesmon and calponin, whose role is far from being elucidated in the uterus [184], [183].
Like the intracellular space, the extracellular space of uterus tissue is similarly complex. But unlike the intracellular space, the role of the interstitial space on the spread of electrical activity is less well understood or appreciated.

Uterus electrophysiology at the tissue level is typically modeled with continuum approximations via the monodomain or bidomain equations, two time-dependent systems of partial differential equations (PDEs) describing the propagation of the transmembrane (and extracellular) potential through the uterus tissue. In order to improve the realism of the model used to solve the forward problem, we implemented a framework for simulating the uterus contraction using the Python interface to FEniCS [52].

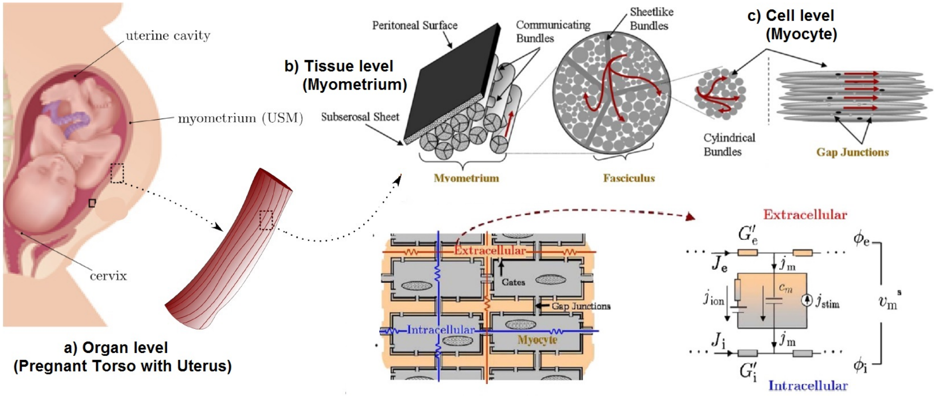

Figure 5.1: A Multiscale Model of the uterus from cell to organ level

5.2 The Torso

The mathematical model for electrical activity in the tissue is based on local volume averaging. Indeed, modeling each cell separately would be much too costly). We consider the body as a volume conductor, in which the electrical activity can be described by the Maxwell's equations. We assume that the effect of temporal variations is negligible, so that we consider the static equation 5.1 giving the electric field E.

$$\nabla \times E = 0 \tag{5.1}$$

From 5.1, the electric field can be written from an electric potential u as:

$$E = -\nabla u \tag{5.2}$$

The current density J in a conductor is directly related to the electrical field E by the conductivity M of the medium. This relates J 5.3 with the electrical potential u 5.2.

$$J = -M\nabla u \tag{5.3}$$

The active uterus tissue generates current sources in the body, modeled as one or more dipoles. The approach considered here consists in computing the potential distribution only to area of the body immediately surrounding the uterus. We introduce this aera as the torso, denoted as ΩT . The torso might be viewed as a passive conductor, which amounts to assume that $\nabla J = 0$ in ΩT.
In the following we denote u_T and M_T the electrical potential and conductivity in the torso, respectively. The previous divergence free relation on J leads to the standard relation 5.4 describing the electrical potential in the torso

$$\nabla.(M_T \nabla u_T) = 0 \qquad on \qquad \Omega_T \tag{5.4}$$

It is natural to assume that the body is surrounded by air, considered as electrically insulating. This leads us to consider the homogeneous Neumann bounday condition 5.5 at the exterior surface of the torso $\delta\Omega_T$.

$$M_T(\nabla u_T.n) = 0 \qquad on \qquad \delta\Omega_T. \tag{5.5}$$

We introduce the uterus domain Ω_U as embedded in the torso Ω_T. This implies an inner boundary denoted as δU which is the interface between the uterus and the surrounding torso. We assume that the potential $u_{\delta U}$ is knowm in this region. The problem to solve for the torso then becomes

$$\begin{cases} \nabla.(M_T \nabla u_T) = 0 \qquad on \qquad \Omega_T \\ M_T(\nabla u_T.n) = 0 \qquad on \qquad \delta\Omega_T \\ u_T = u_{\delta U} \qquad on \qquad \delta U \end{cases}$$

5.3 Action Potential Model

The uterus muscle cells belong to a class of cells known as excitable cells, which have the ability to respond actively to an electrical stimulus or to generate spontaneous activity. As described in introduction the uterus cells are also connected, so that a stimulated cell may pass the electrical signal on to neighbouring cells. This ability enables an electric stimulation of one part of the uterus to propagate through the muscle and activate a part of the the uterus. The signal propagation in excitable tissue takes the form of a so-called depolarization of the cells. When the cells are at rest, there is a potential difference across the cell membrane. The potential inside the cells, called the intracellular potential, is negative compared to the extracellular potential, which is the potential in the space between the cells. When excitable cells are stimulated electrically they depolarize, i.e. the difference between intracellular and extracellular potential changes from its normal negative value to being positive or approximately zero. The depolarization followed by a repolarization that restores the potential difference to its resting value. The complete cycle of depolarization and repolarization is called an action potential. Because the potential difference across the cell membrane is essential for the behaviour of excitable tissue, we need to construct a mathematical model that is able to describe this difference. The used Action Potential (AP) model Figure 5.2 is a cellular model developed in our lab and can be found in [151]. For computation time saving, a reduction of the Rihana's model was used. Indeed, as the model considers each vertex as a cell, this AP model needs to be computed 99084 times per integration time. Therefore, the AP model reduction, named Model reduction with only three variables (Red3), is only three variables [96] instead of the 10 equations per cell of the Rihana's original model. The most computation time consuming part of the original model was ICa calcium current. Therefore, the reduction is in part based on the modification of that current with the one proposed by Parthimos et al. [137]. That reduction is a needed step to the execution time of the model to be acceptable, even in recent clusters, and allows a computation to organ scale (whole uterine muscle) rather than tissue scale. Thereby, the three variables of the simpler electrical model are described by the following equations:

$$\frac{dV_m}{dt} = \frac{1}{C_m}(I_{stim} - I_{ca} - I_K - I_{KCa} - I_L) \tag{5.6}$$

$$\frac{dnk}{dt} = \frac{h_{k\infty - nk}}{\tau_{nk}} \tag{5.7}$$

$$\frac{d[Ca]_i^{2+}}{dt} = fc[-\alpha I_{Ca} - K_{Ca}[Ca^{2+}]_i] \tag{5.8}$$

where V_m is the transmembrane potential, n_K is the potassium activation variable, K_{Ca} is the Calcium extraction factor and $[Ca^{2+}]_i$ the intracellular calcium concentration. The ionic currents are I_{Ca} for the voltage dependent calcium channel current, I_K for the voltage dependent potassium channel current, I_{KCa} for the calcium dependent potassium channel current and I_L for the leakage current.

$$I_{ca} = J_{back} + G_{ca}(V_m - E_{ca})\frac{1}{1 + e^{\frac{V_{ca} - V_m}{R_{ca}}}}, \tag{5.9}$$

$$I_K = G_k n_k (V_m - E_K), \tag{5.10}$$

Table 5.1: Parameters of the electrical model.

Variable	Value	Description	Unit
G_k	0.064	Potassium channels conductance	mS/cm^2
G_{kCa}	0.08	Potassium/Calcium channels conductance	mS/cm^2
G_L	0.0055	Leak channels conductance	mS/cm^2
k	0.01	Half-point potassium concentration	μmol
f_c	0.4	calcium influx probability	
a	4e-5	current conservation factor	$molcm^2/\mu C$
k_{ca}	0.1	Ca extraction factor	ms^{-1}
E_l	-20	Leak nerst potential	mV
E_k	-83	Potassium nerst potential	mV
R	8.318	gas constant	$JK^{-1}mol^{-1}$
T	295	Temperature	K
F	96.487	Faraday constant	KC mol
$\left[ca^{2+}\right]$	3	Extracellular calcium concentration	mmol
J_{back}	0.023	Background calcium current	mA/cm^2
G_{ca}	0.022	VOCC conductance	mS/cm^2
V_{ca}	-20.07	Half-point of the VOCC activation sigmoid	mV
R_{ca}	5.97	Maximum slope of the VOCC activation	mV

$$I_{kCa} = G_{KCa} \frac{\left[Ca^{2+}\right]_i^2}{\left[Ca^{2+}\right]_i^2 + k^2}(V_m - E_K) \tag{5.11}$$

$$I_L = G_L(V_m - E_L) \tag{5.12}$$

The Nernst potential for Ca^{2+} is given by:

$$E_{Ca} = \frac{RT}{2F} ln\Big[\frac{\left[Ca^{2+}\right]_e}{\left[Ca^{2+}\right]_i}\Big] \tag{5.13}$$

where R is the ideal gas constant and T is the absolute temperature (K).

$$h_{k\infty} = \frac{1}{1 + e^{\frac{4.2 - V_m}{21.1}}} \tag{5.14}$$

$$\tau_{nk} = 23.75 e^{\frac{-V_m}{72.15}} \tag{5.15}$$

The constant for the electrical model are given in Table 1

However, as discussed above, the number of cells in the uterus is too large to model each cell separately. Hence, we considered continuous approximations of the tissue, which must be able to distinguish between the intracellular and extracellular domains.

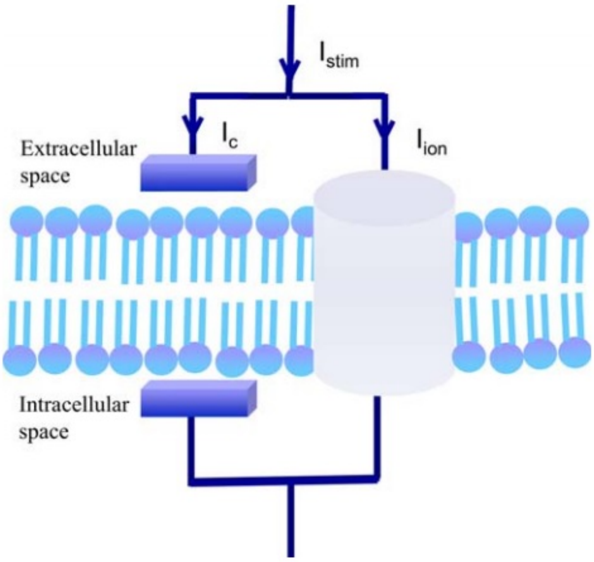

Figure 5.2: Equivalent current source model for the uterus membrane. [30]

5.4 Mathematical derivation of the bidomain model

To include the effects of the potential difference across the membrane, the tissue is now divided into two separate domains: the intracellular and the extracellular. Both domains are assumed to be continuous and they both fill the complete volume of the uterus muscle. The justification for viewing the intracellular space as continuous is that the muscle cells are connected via so-called gap junctions. These are small channels embedded in the cell membrane, which form direct contact between the internals of two neighboring cells. Thanks to the presence of the gap junctions, substances such as ions or small molecules may pass directly from one cell to another, without entering the space between the two cells (the extracellular domain). The intracellular and extracellular domains are separated by the cell membrane. The membrane acts as an electrical insulator between the two domains. The transmembrane potential is defined for every point in the uterus, as the difference between the extracellular and intracellular potential.

Considering the intracellular and extracellular spaces specifically, we have:

$$J_i = -M_i \nabla u_i \tag{5.16}$$

$$J_e = -M_e \nabla u_e \tag{5.17}$$

where J_i and J_e are the intracellular and extracellular current densities, M_i and M_e are the corresponding conductivity tensors, respectively, and u_i and u_e are the respective potentials.

We introduce now C_m the capacitance of the cell membrane, q_i (resp. q_e) the intracellular (resp.

extracellular) charge. The charge accumulation is balanced, and we have the relation

$$\frac{\partial q_i}{\partial t} = -\frac{\partial q_e}{\partial t} = \chi C_m \frac{\partial v}{\partial t} \tag{5.18}$$

Due to the potential difference v, the ions are forced to move across the membrane in a definite direction. We introduce the corresponding ionic current I_{ion} across the membrane. The net current must be equal to the sum of the rate of charge accumulation and the ionic current, giving

$$-\bigtriangledown . J_i = \frac{\partial q_i}{\partial t} + \chi I_{ion} \tag{5.19}$$

From the definition of the curent density Ji, we obtain

$$\bigtriangledown (Mi \bigtriangledown ui) = \chi Cm \frac{\partial v}{\partial t} + \chi I_{ion} \tag{5.20}$$

Let's remind that the difference of potential across the membrane is $v = ui - ue$.

$$\bigtriangledown \cdot (Mi \bigtriangledown v) + \bigtriangledown (Mi \bigtriangledown u_e) = \chi C_m \frac{\partial v}{\partial t} + \chi I_{ion} \qquad on \qquad \Omega_H \tag{5.21}$$

$$\bigtriangledown \cdot (Mi \bigtriangledown v) + \bigtriangledown ((M_i + M_e) \bigtriangledown u_e) = 0 \qquad on \qquad \Omega_H \tag{5.22}$$

Also, we assume that the intracellular domain is not in contact with the interface δH between the uterus and the torso. This correspond to the homogeneous condition

$$Mi(\bigtriangledown u_i \cdot n) = M_i(\bigtriangledown v \cdot n) + M_i(\bigtriangledown u_e \cdot n) = 0 \qquad on \qquad H \tag{5.23}$$

The numerical solution of the bidomain equations was based on [50], where efficient numerical methods were used to solve these equations. For the bidomain model, we applied operator splitting to separate the coupled nonlinear systems of partial differential equations (PDEs) into a system of ODEs, a parabolic PDE, and an elliptic PDE [175]. The system of ODEs associated with the cell model kinetics was integrated using appropriate implicit methods [167].

5.5 Coupling the uterus and the torso

The coupling between the uterus tissue and the torso surrounding the uterus concerns what is happening at the interface at the interface δU (Figure 5.3). The conservation of the current between the uterus and the torso reads as the boundary condition

$$Mi(\bigtriangledown u_i \cdot n) + M_e(\bigtriangledown u_e \cdot n) = M_T(\bigtriangledown_{u_T} n) \qquad on \qquad \delta H \tag{5.24}$$

Rewriting the equation from the transmembrane potential v, we obtain

$$\begin{cases} \triangledown \cdot (Mi \triangledown v) + \triangledown(Mi \triangledown u_e) = \chi C_m \frac{\partial v}{\partial t} + \chi I_{ion} \qquad on \qquad \Omega_H \\ \triangledown \cdot (Mi \triangledown v) + \triangledown((M_i + M_e) \triangledown u_e) = 0 \qquad on \qquad \Omega_H \\ \nabla.(M_T \nabla u_T) = 0 \qquad on \qquad \Omega_T \\ M_T(\nabla u_T.n) = 0 \qquad on \qquad \delta\Omega_T \\ u_T = u_e \qquad on \qquad \delta H \\ M_i(\triangledown u_i \cdot n) + M_i(\triangledown u_e \cdot n) = 0 \qquad on \qquad \Omega_H \\ M_i(\triangledown u_i \cdot v) + (M_i + M_e)(\triangledown u_e \cdot n) = M_T(\triangledown u_T) \qquad on \qquad \Omega_H \end{cases}$$

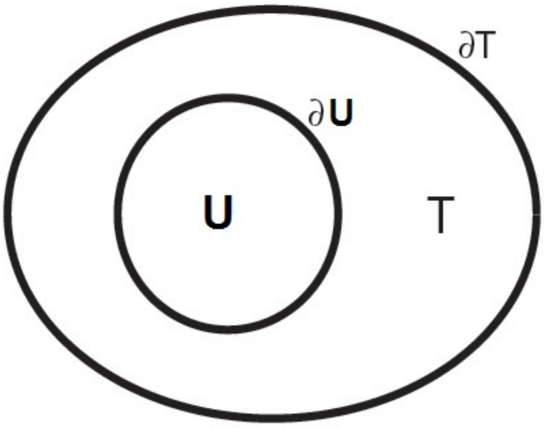

Figure 5.3: Coupling between the uterus and the torso

5.6 3D realistic uterine muscle mesh

We used a 3D realistic mesh of a uterus. The mesh has been obtained thanks to the FEMONUM project (http:// femonum.telecom-paristech.fr/) extracted from MRI images. This mesh was performed at 34.5 weeks of amenhorrea. A tetrahedron mesh is built upon the surface mesh using TetGen [162].
In order to construct the regions, on the mesh that we used for this study, we used a random seed selection among the vertices of the mesh and then a region-growing algorithm. In the model, we can choose the number of regions. Concerning the seed selection, a Poisson disk sampling distribution algorithm [118] was used. It allows to have a well distributed seeds on the uterus surface without having seeds too close from each other as it could be the case if we used a completely random selection. The algorithm for region-growing (see Annex Algorithm 1) permits to attribute one different label per seed. It allows to attribute one different label per seed, found by Poisson disk distributions (representing the regions), from one to the number of chosen seeds. Then, each region propagates its label to its neighbors until all vertices in the mesh are attributed.

In order to electrically isolate regions from each other, the conductivities is set to a 0.001 ms/cm at the border and 0.0068 ms/cm inside the regions Figure 5.4.

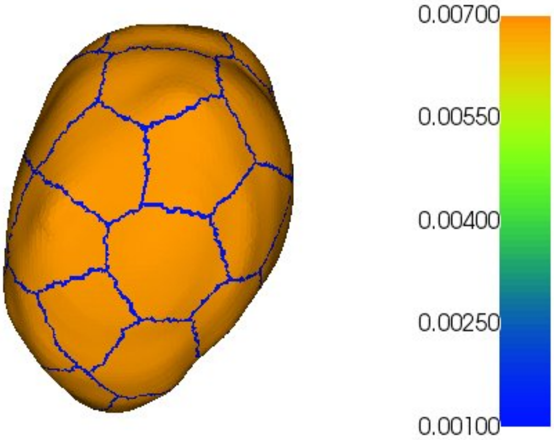

Figure 5.4: An illustration of 27 regions where the conductivites in the border is 0.001 ms/cm and 0.0068 ms/cm inside the regions.

5.7 Numerical model:Operator Splitting

We used the operator splitting technique to solve the complete coupled model described in the previous section. It consists in introducing operators $L1$ and $L2$ so that our problem can read on the form

$$\frac{\partial u}{\partial t} = (L1 + L2)u \tag{5.25}$$

with u the solution of the problem, and $u(0) = u_0$ an initial condition. The problem is then splitt into three steps. Considering a small time step t, we first solve the problem for $t \in [0, \frac{\triangle t}{2}]$ (step 1)

$$\frac{\partial v}{\partial t} = L_{1v} \qquad with \qquad v(0) = u_0 \tag{5.26}$$

Then, we solve the problem associated with the L_2 operator for $t \in [0, \triangle t]$ (step 2)

$$\frac{\partial w}{\partial t} = L_{2v} \qquad with \qquad w(0) = v(\frac{\triangle t}{2}) \tag{5.27}$$

And finally, we come back to the $L1$ operator for $t \in [\triangle t/2, \triangle t]$ (step 3) To model the coupling of the uterus and the torso, the definition of the operators L1 and L2 are:

$$L_{1v} = -\frac{1}{C_m} I_{ion}(v) \tag{5.28}$$

$$L_{2v} = \bigtriangledown \cdot (M_i \bigtriangledown_{ue}) \tag{5.29}$$

We apply a θ - formulation as a generalization of the previously introduced operator splitting technique, with $0 \leq \theta \leq 1$. We denote $v^n = v(t_n)$, and we apply the three previous steps of the method to compute v^{n+1} for each $t_n \in [0, T]$.

Step1

Solve the system for $t_n < t < t_n + \theta \bigtriangleup t$

$$\frac{\partial v}{\partial t} = -I_{ion}(v) \qquad with \qquad v(t^n) = u_0) \tag{5.30}$$

The solution is $v_\theta^n = v(t_n + \theta \bigtriangleup t)$

Step2

Solve the system for $t_n < t < t_n + \triangle t, with v(t^n) = v_\theta^n$

$$\bigtriangledown \cdot (M_i \bigtriangledown v) + \bigtriangledown (M_i \bigtriangledown u_e) = \chi C_m \frac{\partial v}{\partial t} + \chi I_{ion} \qquad \Omega H \tag{5.31}$$

$$\bigtriangledown \cdot (M_i \bigtriangledown u) + \bigtriangledown ((M_i + M_e) \nabla u_e) = 0 \qquad on \qquad \Omega_T \tag{5.32}$$

$$\nabla \cdot (M_T \nabla u_T) = 0 \qquad on \qquad \Omega_T \tag{5.33}$$

The solution is $v^{n+1} = v(t_n + \triangle t)$.

Step3

Solve the system for $t_n + \theta \bigtriangleup t < t < t_n + \triangle t$

$$\frac{\partial v}{\partial t} = -I_{ion}(v) \qquad with \qquad v(t^n + \theta \bigtriangleup t) = v_\theta^{n+1}) \tag{5.34}$$

The solution is $v^{n+1} = -v(t_n + \triangle t$.

The discretization of this problem is based on a $\theta - rule$ for time discretization, and on a finite element method in space. The steps 1 and 3 could be resolved with a standard single-domain model. We introduce $V(H)$ a function space defined over the domain ω_H, and $V(T)$ a function space defined over the domain ω_T . In this way, the solutions v and u_e will be in $V(H)$ and the solution u_T will be in $V(T)$. In the following, $u_e^{n+\theta}$ (resp. $u_T^{n+\theta}$) denotes an approximation of u_e (resp. u_T) at time $t_n + \theta \triangle t$. We multiply the two first equations by a test function $\psi_H \in V(H)$ and the second one by a test function $\psi_T \in V(T)$, and integrate over the respective domains. This gives the variational formulation.

Equation 1

$$\int_{\Omega_H} v_\theta^{n+1}\psi_H + \theta\nabla t\int_{\Omega_H} M_i\nabla v_\theta^{n+1}\cdot\nabla\psi_H + \triangle t \in_{\Omega_H} -\theta\delta t\int_{\delta_H} M_i(\nabla v_\theta^{n+1}\cdot n)\psi_H - \nabla t\int_{\delta H} M_i(\nabla u_e^{n+\theta}\cdot n)\psi_H \tag{5.35}$$

$$= \int_{\Omega_H} v_\theta^n\psi_H - (1-\theta)\triangle t\int_{Omega_H} M_i\nabla v_\theta^n\cdot\nabla\psi_H + (1-\theta)\triangle t\int_{\delta_H} M_i(\nabla v_\theta^n\cdot n)\psi_H \tag{5.36}$$

Equation 2

$$-\theta\int_{\Omega_H} M_i\nabla v_\theta^{n+1}\cdot\nabla\psi_H - (1-\theta)\int_{\Omega_H} M_i\nabla v_\theta^n\cdot\nabla\psi_H - \int_{\Omega_H}(M_i+M_e)\nabla u_e^{n+\theta}\cdot\nabla\psi_H + \theta\int_{\delta_H} M_i(\nabla v_\theta^{n+1}\cdot n)\psi_H \tag{5.37}$$

$$+(1-\theta) + (1-\theta)\triangle t\int_{\delta_H} M_i(\nabla v_\theta^n\cdot n)\psi_H + \int_{\delta_H}(M_i+M_e)(\nabla u_e^{n+\theta}\cdot n)\psi_H = 0 \qquad \forall\psi_H \qquad \in V(H) \tag{5.38}$$

Equation 3

$$-\int_{\Omega_H} M_T\nabla u_T^{n+\theta} + \int_{\Omega_H} M_T(\nabla u_T^{n+\theta}\cdot n_T)\psi_T + \int_{\delta_T}(\nabla u_T^{n+\theta}\cdot n_T)\psi_T = 0 \qquad \forall\psi_T \qquad \in V(T) \tag{5.39}$$

The continuity condition is used to define a new field u defined over the whole domain $H\cup T$. Considering the previous notations $u_e^{n+\theta}$ and $u_T^{n+\theta}$, we define

$$u^{n+\theta} = \begin{cases} u_e^{n+\theta} & \text{for } x \in H \\ u_T n + \theta & \text{for } x \in T \end{cases} \tag{5.40}$$

This new field $u^{n+\theta}$ is continuous at the interface δH.

We define a new function space $V(H\cup T)$ for this field, and the previous test function ψH and ψT can then be replaced by a single test function $\psi \in V(H\cup T)$. We multiply the 2nd equation by $\frac{-\triangle t}{\theta}$, and we apply the boundary conditions. The weak form is reduced to

$$\int_{\Omega_H} v_\theta^{n+1}\psi_H + \theta\triangle t\int_{\Omega_H} M_i\nabla v_\theta^{n+1}\cdot\nabla\psi_H + \triangle t\int_{\Omega_H} M_i\nabla v_\theta^{n+1}\cdot\nabla\psi_H \tag{5.41}$$

$$= \int_{\Omega_H} v_\theta^{n+1}\psi_H - (1-\theta)\triangle t\int_{\Omega_H} M_i\nabla v_\theta^n\cdot\nabla\psi_H \qquad \forall\psi_H \qquad \in V(H) \tag{5.42}$$

$$\triangle t \int_{\Omega_H} M_i \nabla v_\theta^{n+1} \cdot \nabla\psi + \frac{-\triangle t}{\theta} \int_{\Omega_H} (M_i + M_e)\nabla u^{n+\theta} \cdot \nabla\psi + \frac{\triangle t}{\theta} \int_{\Omega_H} (M_T)\nabla u^{n+\theta} \cdot \nabla\psi \tag{5.43}$$

$$= -\frac{\triangle t(1-\theta)}{\theta} \int_{\Omega_H} M_i \nabla v_\theta^{n+1} \cdot \nabla\psi \qquad \forall\psi \qquad \in V(H \cup t = T) \tag{5.44}$$

5.8 Numerical Experiments

5.8.1 Simulation on a 3D Mesh

In this simulation, we consider three dimensional domains (3D volumetric mesh). We run coupled cell model bidomain simulations, with the Red3 model. In the numerical simulations we used the parameters presented in Table 1 for the modified Red3 model. Figure 5.5 represents the simulation of an action potential for a bidomain approach. The tissue has a negative resting potential, typically v = 50mV. Then, the cell depolarizes, returning to its negative resting potential. The whole process is called the action potential. In Figure 5.6 we present the results of the simulation of a propagated activity on a whole isotropic uterus (no regions). The signal propagation in this uterus takes the form of a depolarization, where the potential rises and reaches a positive peak potential after a couple of milliseconds.

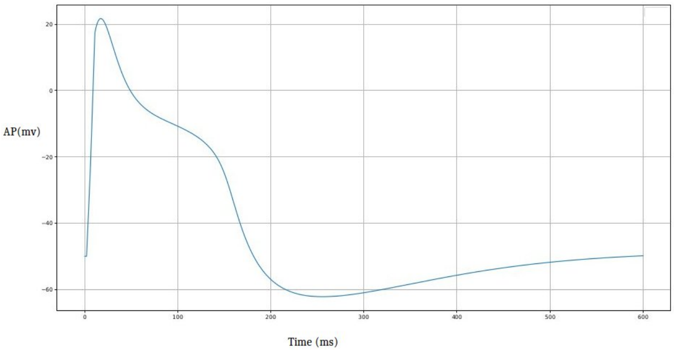

Figure 5.5: Action potential of single cell

5.9 Discussion and conclusion

We presented a mathematical description of the bidomain model for simulating the electrical behavior of uterus tissue. An approach is presented to simulate the propagation of the excitation in the uterus tissues, based on non linear models of reaction-diffusion type, considering the bidomain approach. The ionic currents are expressed by the simple modified electrophysiological cell model (Red3), especially designed for human uterus tissue. One approach that has gained interest in this work views the uterus

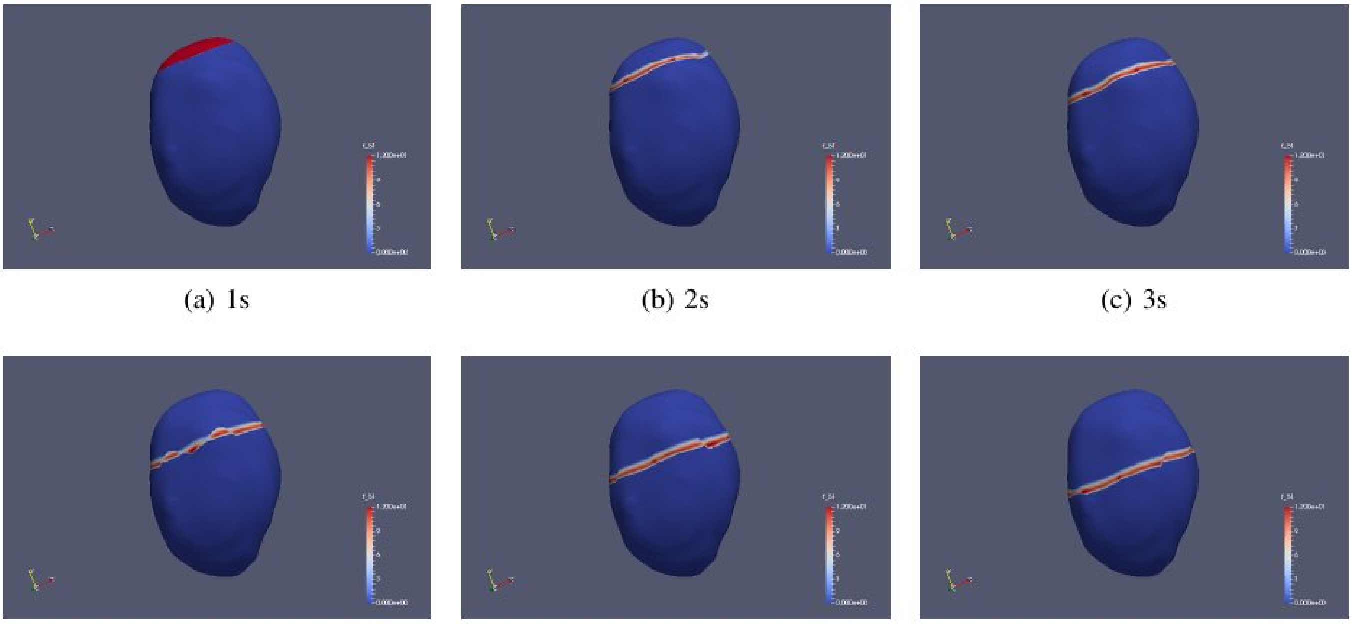

(a) 1s (b) 2s (c) 3s

(d) 4s (e) 5s (f) 6s

Figure 5.6: Results of the simulation Figures a) to f) correspond to the electrical activity of the uterus; Each figure corresponds to a given time of the simulation: respectively [1s, 2s, 3s, 4s, 5s, 6s]

tissue not as a discrete structure, but rather as two coupled, continuous domains: one for the intracellular space and the other for the interstitial space. For convenience, the averaged potentials and currents in both domains are defined at every point in space. The structure is partially preserved by assigning a conductivity tensor at each point. Numerical simulations on a three-dimensional domain (volumetric mesh) were done to show the behavior of the excitation spread and the repolarization phase for isotropic electric activity. The results show that the proposed developed approach can successfully be used to simulate uterus isotropic propagation of the excitation in three-dimensional tissue. It suggests that such method may provide a good basis for uterus simulation research in a more physiologically way. The present developed approach helps calculate the intra-cellular and extra-cellular action potential of uterus tissues in the uterus physical domain which can be used to predict the uterus electrohystrogram (EHG).

6

Conclusions and perspectives

The technique of EHGI allows a noninvasive reconstruction of the electrical potential on the uterus surface based on electrical potential measured on the body surface and anatomical data of the torso. EHGI provides very precious information about the uterus condition since it is able to provide refined spatial description of the electrical wave pathway and magnitude on the uterus surface. This may help a lot in different clinical interventions. The scientific algorithms behind any EHGI tool are able to preprocess the anatomical data of the patient in order to provide a computational mesh, filter noisy measurements of the electrical potential and solve an inverse problem.

The inverse problem in uterus electrohysterography (electrohysterography imaging (EHGI)) is a new and a powerful diagnosis technique. This non-invasive technology interests more and more medical in-dustries. The success of this technology would be considered as a breakthrough in the uterus diagnosis. However, in many cases the quality of reconstructed electrical potential is not accurate enough. The difficulty comes from the fact that the inverse problem in uterus electrohysterography is well known as a mathematically ill-posed problem. Different methods based on Thikhnov regularization have been used in order to regularize the problem.

We have conducted our analysis by using a realistic uterus model and have aimed at identifying the spa-tial extent of the sources. The computer simulations have shown that both SVB-SCCD and VB-SCCD exhibited the best performance, which permits to simultaneously localize several highly correlated active source regions. They appear therefore to be the most promising approaches for the identification of multiple active uterus regions in the context of propagation phenomena. When applying SVB-SCCD in-verse method to real signals, our analysis of the evolution of the real sources during contraction showed a non-linear propagation, propagating slowly in tissue, with complex pathways and noncontiguously.

Identifying uterus networks from noninvasive EHG data is a challenging issue. The joint use of the two needed approaches (source localization combined with functional connectivity analysis is still novel and raises a number of methodological issues that should be controlled in order to get appropriate and interpretable results. We presented a comparative analysis of the results obtained from the possible combinations between three algorithms to solve the EHG inverse problem and three methods to estimate the functional connectivity.

The results show that the choice of the inverse algorithm and the connectivity method is crucial and can strongly alter the results and their interpretation. By proposing a quantitative comparison procedure, we were able to propose one combination of methods (scbsccd and h2) that aoutperform the previously obtained results. This could be due to the ability of scbsccd to efficiently separate extended and sources. The non linear correlation h2 is also a method that is proved to be efficient for the characterization of uterine connectivity, which is clearly a non linear process. This combination of methods leads to the most relevant networks as compared with the ground-truth simulations. This source connectivity approach when applied to EHG could be a valuable method to identify uterus networks. However, results are highly dependent on the choice of the processing methods.

Computational uterus modeling is becoming an increasingly powerful tool in uterus disease research. Uterus electrophysiology at the tissue level is presently modeled with a discrete approach based on ordinary differential Equation (ODEs) describing the excitation and diffusion processes of the transmembrane potential through the uterus tissue. We presented in this work a mathematical description of a bidomain model for simulating the electrical behavior of uterus tissue. Numerical simulations on a three-dimensional domain (volumetric mesh) were simu-lated to show the behavior of the excitation spread and the repolarization phase for isotropic electric activity. The results show that the proposed developed numerical code can successfully be used to simulate uterus excitation isotropic propagation in three-dimensional tissue. It suggests that such bidomain method may provide a good basis for uterus simulation research in a more physiologically way.

In future work we would like to go deeply to the clinical applications (estimating the sizes of the regions, analysing the synchronicity between them). An interface that will permit to ease this process is presented in Apendix A. We would also like to improve the model used to solve the forward problem to get a more realistic representation of the uterine behavior. In the ideal, this model should be rendered patient specific to face to the wide interindividual variability encountered in the clinical practice. Indeed, to investigate the performance of this method in localizing synchronous regions from clinical measurements, we have to assume that the electrophysiological model that will be used to constrain the minimization problem is sufficiently accurate.

Associated publications

Parts of the work presented in this thesis can be associated with the following publications:

Journal Paper

S. Zahran, A. Diab, R. Arman Chowdhury, T. Hedrich, M. Hassan, C. Grova, M. Yochum, M. Khalil, C. Marque. Performance of source imaging techniques of spatially extended generators of uterine activity, Submitted to Informatics in Medicine Unlocked - Journal - Elsevier

International Conference papers

Zahran, S., Yochum, M., Diab, A., Marque, C. (2017, July). Variation-based sparse source imaging in localizing uterine activity. In Engineering in Medicine and Biology Society (EMBC), 2017 39th Annual International Conference of the IEEE (pp. 2948-2951).

Zahran, S., A. Diab, B. Al Rifai, M. Khalil, C. Marque, Separation and localization of EHG sources using tensor models. In Advances in Biomedical Engineering (ICABME), 2017 Fourth International Conference on (pp. 1-4). IEEE

Nader, N., **Zahran, S.**, Marque, C., Hassan, M., Yochum, M., Falou, W.& Khalil, M. (2017, October). Graph analysis of uterine networks using EHG source connectivity. In Advances in Biomedical Engineering (ICABME), 2017 Fourth International Conference on (pp. 1-4). IEEE

Zahran, S., Diab, A., Khalil, M., & Marque, C. (2018, March). Source localization of uterine activity using maximum entropy on the mean approach. In 2018 IEEE 4th Middle East Conference on Biomedical Engineering (MECBME) (pp. 247-251). IEEE.

Bibliography

[1] https://www.dataschool.io/roc-curves-and-auc-explained/.

[2] https://www.stanfordchildrens.org/en/topic/default?id=complications-of-pregnancy-85-p01198.

[3] Abe, Y. The hormonal control and the effects of drugs and ions on the electrical and mechanical activity of the uterus. *Smooth muscle* (1970), 396–417.

[4] Aguilar, H. N., and Mitchell, B. Physiological pathways and molecular mechanisms regulating uterine contractility. *Human reproduction update 16*, 6 (2010), 725–744.

[5] Alexandersson, A., Steingrimsdottir, T., Terrien, J., Marque, C., and Karlsson, B. The icelandic 16-electrode electrohysterogram database. *Scientific data 2* (2015).

[6] Alvarez, H., and Caldeyro, R. Contractility of the human uterus recorded by new methods. *Surgery Gynecology and Obstetrics 91*, 1 (1950), 1–13.

[7] Amblard, M. Conventions et comptabilité: vers une approche sociologique du modèle. *Comptabilité-Contrôle-Audit 10*, 3 (2004), 47–67.

[8] Ansari-Asl, K., Wendling, F., Bellanger, J.-J., and Senhadji, L. Comparison of two estimators of time-frequency interdependencies between nonstationary signals: application to epileptic eeg. In *Engineering in Medicine and Biology Society, 2004. IEMBS'04. 26th Annual International Conference of the IEEE* (2004), vol. 1, IEEE, pp. 263–266.

[9] Arora, S., and Garg, G. A novel scheme to classify ehg signal for term and pre-term pregnancy analysis. *International Journal of Computer Applications 51*, 18 (2012).

[10] Baggish, M. S., Valle, R. F., and Guedj, H. *Hysteroscopy: Visual perspectives of uterine anatomy, physiology and pathology*. Lippincott Williams & Wilkins, 2007.

[11] Bailey, G., Parkington, J., Audouze, F., Renfrew, C., Schlanger, N., Sherratt, A., Taylor, T., Ashmore, W., et al. *The archaeology of prehistoric coastlines*. Cambridge University Press, 1988.

[12] Baillet, S., Mosher, J. C., and Leahy, R. M. Electromagnetic brain mapping. *IEEE Signal processing magazine 18*, 6 (2001), 14–30.

[13] Bear, L., Cuculich, P. S., Bernus, O., Efimov, I., and Dubois, R. Introduction to noninvasive cardiac mapping. *Cardiac electrophysiology clinics 7*, 1 (2015), 1–16.

[14] Becker, H., Albera, L., Comon, P., Gribonval, R., and Merlet, I. Fast, variation-based methods for the analysis of extended brain sources. In *2014 22nd European Signal Processing Conference (EUSIPCO)* (2014), IEEE, pp. 41–45.

[15] Becker, H., Albera, L., Comon, P., Haardt, M., Birot, G., Wendling, F., Gavaret, M., Bénar, C.-G., and Merlet, I. Eeg extended source localization: tensor-based vs. conventional methods. *NeuroImage 96* (2014), 143–157.

[16] Becker, H., Comon, P., Albera, L., Haardt, M., and Merlet, I. Multi-way space–time–wave-vector analysis for eeg source separation. *Signal Processing 92*, 4 (2012), 1021–1031.

[17] Bibin, L., Anquez, J., de la Plata Alcalde, J. P., Boubekeur, T., Angelini, E. D., and Bloch, I. Whole-body pregnant woman modeling by digital geometry processing with detailed uterofetal unit based on medical images. *IEEE Transactions on Biomedical Engineering 57*, 10 (2010), 2346–2358.

[18] Boccaletti, S., Latora, V., Moreno, Y., Chavez, M., and Hwang, D.-U. Complex networks: Structure and dynamics. *Physics reports 424*, 4-5 (2006), 175–308.

[19] Brazier, M. A. Studies of the eeg activity of limbic structures in man. *Electroencephalography and clinical neurophysiology 25*, 4 (1968), 309–318.

[20] Brazier, M. A., and Casby, J. U. Crosscorrelation and autocorrelation studies of electroencephalographic potentials. *Electroencephalography and clinical neurophysiology 4*, 2 (1952), 201–211.

[21] Brennan, C. W., Verhaak, R. G., McKenna, A., Campos, B., Noushmehr, H., Salama, S. R., Zheng, S., Chakravarty, D., Sanborn, J. Z., Berman, S. H., et al. The somatic genomic landscape of glioblastoma. *Cell 155*, 2 (2013), 462–477.

[22] Buhimschi, C., Boyle, M. B., Saade, G. R., and Garfield, R. E. Uterine activity during pregnancy and labor assessed by simultaneous recordings from the myometrium and abdominal surface in the rat. *American journal of obstetrics and gynecology 178*, 4 (1998), 811–822.

[23] Buhimschi, C., and Garfield, R. Uterine contractility as assessed by abdominal surface recording of electromyographic activity in rats during pregnancy. *American journal of obstetrics and gynecology 174*, 2 (1996), 744–753.

[24] BULLMORE, E., AND SPORNS, O. Complex brain networks: graph theoretical analysis of structural and functional systems. *Nature Reviews Neuroscience 10*, 3 (2009), 186.

[25] BURGER, M. Inverse problems in ion channel modelling. *Inverse Problems 27*, 8 (2011), 083001.

[26] CABANISS, M. L., AND ROSS, M. G. *Fetal monitoring interpretation.* Lippincott Williams & Wilkins, 2010.

[27] CALDEYRO-BARCIA, R., AND POSEIRO, J. J. Physiology of the uterine contraction. *Clinical Obstetrics and Gynecology 3*, 2 (1960), 386–410.

[28] CALDEYRO-BARCIA, R., SICA-BLANCO, Y., POSEIRO, J., PANIZZA, V. G., MENDEZ-BAUER, C., FIELITZ, C., ALVAREZ, H., POSE, S., AND HENDRICKS, C. A quantitative study of the action of synthetic oxytocin on the pregnant human uterus. *Journal of Pharmacology and Experimental Therapeutics 121*, 1 (1957), 18–31.

[29] CHARD, T., AND GRUDZINSKAS, J. G. *The uterus.* Cambridge University Press, 1994.

[30] CHKEIR, A. *Modélisation de la propagation de l'activité électrique utérine avec des approches mathématiques et expérimentales.* PhD thesis, Compiègne, 2011.

[31] CHO, J.-H., HONG, S. B., JUNG, Y.-J., KANG, H.-C., KIM, H. D., SUH, M., JUNG, K.-Y., AND IM, C.-H. Evaluation of algorithms for intracranial eeg (ieeg) source imaging of extended sources: feasibility of using ieeg source imaging for localizing epileptogenic zones in secondary generalized epilepsy. *Brain topography 24*, 2 (2011), 91–104.

[32] CHOWDHURY, R. A., LINA, J. M., KOBAYASHI, E., AND GROVA, C. Meg source localization of spatially extended generators of epileptic activity: comparing entropic and hierarchical bayesian approaches. *PloS one 8*, 2 (2013), e55969.

[33] CLARKE, C., AND JANDAY, B. The solution of the biomagnetic inverse problem by maximum statistical entropy. *Inverse Problems 5*, 4 (1989), 483.

[34] CLUITMANS, M., PEETERS, R., WESTRA, R., AND VOLDERS, P. Noninvasive reconstruction of cardiac electrical activity: update on current methods, applications and challenges. *Netherlands Heart Journal 23*, 6 (2015), 301–311.

[35] COLE, W., GARFIELD, R., AND KIRKALDY, J. Gap junctions and direct intercellular communication between rat uterine smooth muscle cells. *American Journal of Physiology-Cell Physiology 249*, 1 (1985), C20–C31.

[36] COSTELOE, K. Epicure: facts and figures: why preterm labour should be treated. *BJOG: An International Journal of Obstetrics & Gynaecology 113* (2006), 10–12.

[37] Creasy, R. K. Preterm birth prevention: where are we? *American Journal of Obstetrics & Gynecology 168*, 4 (1993), 1223–1230.

[38] Csapo, A. Progesterone "block". *Developmental Dynamics 98*, 2 (1956), 273–291.

[39] Csapo, A. Smooth muscle as a contractile unit. *Physiological reviews. Supplement 5* (1962), 7–33.

[40] Csapo, A. The diagnostic significance of the intrauterine pressure. *Obstetrical & gynecological survey 25*, 6 (1970), 515–543.

[41] Csapo, A., and Suzuki, T. A preliminary note on excitation-contraction coupling. *Proceedings of the National Academy of Sciences 43*, 3 (1957), 278–281.

[42] Csapo, A. I., Takeda, H., and Wood, C. Volume and activity of the parturient rabbit uterus. *American journal of obstetrics and gynecology 85*, 6 (1963), 813–818.

[43] Dale, A. M., and Sereno, M. I. Improved localizadon of cortical activity by combining eeg and meg with mri cortical surface reconstruction: a linear approach. *Journal of cognitive neuroscience 5*, 2 (1993), 162–176.

[44] Devedeux, D., Marque, C., Mansour, S., Germain, G., and Duchêne, J. Uterine electromyography: a critical review. *American journal of obstetrics and gynecology 169*, 6 (1993), 1636–1653.

[45] Diab, A., Hassan, M., Boudaoud, S., Marque, C., and Karlsson, B. Nonlinear estimation of coupling and directionality between signals: Application to uterine emg propagation. In *Engineering in Medicine and Biology Society (EMBC), 2013 35th Annual International Conference of the IEEE* (2013), IEEE, pp. 4366–4369.

[46] Diab, A., Hassan, M., Marque, C., and Karlsson, B. Quantitative performance analysis of four methods of evaluating signal nonlinearity: application to uterine emg signals. In *Engineering in Medicine and Biology Society (EMBC), 2012 Annual International Conference of the IEEE* (2012), IEEE, pp. 1045–1048.

[47] Diab, M. O., Marque, C., and Khalil, M. A. Classification for uterine emg signals: comparison between ar model and statistical classification method. *INTERNATIONAL JOURNAL OF COMPUTATIONAL COGNITION (HTTP://WWW. IJCC. US) 5*, 1 (2007).

[48] Ding, L. Reconstructing cortical current density by exploring sparseness in the transform domain. *Physics in Medicine and Biology 54*, 9 (2009), 2683.

[49] DORET, M., BUKOWSKI, R., LONGO, M., MAUL, H., MANER, W. L., GARFIELD, R. E., AND SAADE, G. R. Uterine electromyography characteristics for early diagnosis of mifepristone-induced preterm labor. *Obstetrics & Gynecology 105*, 4 (2005), 822–830.

[50] DOS SANTOS, R. W., PLANK, G., BAUER, S., AND VIGMOND, E. J. Parallel multigrid preconditioner for the cardiac bidomain model. *IEEE Transactions on Biomedical Engineering 51*, 11 (2004), 1960–1968.

[51] DUCHENE, J., MARQUE, C., AND PLANQUE, S. Uterine emg signal: propagation analysis. In *Engineering in Medicine and Biology Society, 1990., Proceedings of the Twelfth Annual International Conference of the IEEE* (1990), IEEE, pp. 831–832.

[52] DUPONT, T., HOFFMAN, J., JOHNSON, C., KIRBY, R. C., LARSON, M. G., LOGG, A., AND SCOTT, L. R. *The fenics project*. Chalmers Finite Element Centre, Chalmers University of Technology, 2003.

[53] ELLIS, H. Anatomy of the uterus. *Anaesthesia & Intensive care medicine 6*, 3 (2005), 74–75.

[54] ENGSTRÖM, L., JINNEROT, H., AND JONASSON, E. Thickness of subcutaneous fat tissue where pregnant diabetics inject their insulin-an ultrasound study. *Diabetes Research and Clinical Practice 50* (2000), 215.

[55] ESWARAN, H., PREISSL, H., WILSON, J. D., MURPHY, P., ROBINSON, S. E., AND LOWERY, C. L. First magnetomyographic recordings of uterine activity with spatial-temporal information with a 151-channel sensor array. *American journal of obstetrics and gynecology 187*, 1 (2002), 145–151.

[56] EULIANO, T. Y., MAROSSERO, D., NGUYEN, M. T., EULIANO, N. R., PRINCIPE, J., AND EDWARDS, R. K. Spatiotemporal electrohysterography patterns in normal and arrested labor. *American Journal of Obstetrics and Gynecology 200*, 1 (2009), 54–e1.

[57] FANCHIN, R., AYOUBI, J.-M., RIGHINI, C., OLIVENNES, F., SCHÖNAUER, L. M., AND FRYDMAN, R. Uterine contractility decreases at the time of blastocyst transfers. *Human Reproduction 16*, 6 (2001), 1115–1119.

[58] FELE-ŽORŽ, G., KAVŠEK, G., NOVAK-ANTOLIČ, Ž., AND JAGER, F. A comparison of various linear and non-linear signal processing techniques to separate uterine emg records of term and pre-term delivery groups. *Medical & biological engineering & computing 46*, 9 (2008), 911–922.

[59] FRANASIAK, J. M., AND SCOTT, R. T. Reproductive tract microbiome in assisted reproductive technologies. *Fertility and sterility 104*, 6 (2015), 1364–1371.

[60] FRISTON, K., HARRISON, L., DAUNIZEAU, J., KIEBEL, S., PHILLIPS, C., TRUJILLO-BARRETO, N., HENSON, R., FLANDIN, G., AND MATTOUT, J. Multiple sparse priors for the m/eeg inverse problem. *NeuroImage 39*, 3 (2008), 1104–1120.

[61] GARCIA, M. A., AND BAFFA, O. Magnetic fields from skeletal muscles: a valuable physiological measurement? *Frontiers in physiology 6* (2015).

[62] GARFIELD, J. How students learn statistics. *International Statistical Review/Revue Internationale de Statistique* (1995), 25–34.

[63] GARFIELD, R., AND HAYASHI, R. Appearance of gap junctions in the myometrium of women during labor. *American journal of obstetrics and gynecology 140*, 3 (1981), 254–260.

[64] GARFIELD, R., MERRETT, D., AND GROVER, A. Gap junction formation and regulation in myometrium. *American Journal of Physiology-Cell Physiology 239*, 5 (1980), C217–C228.

[65] GARFIELD, R., SAADE, G., BUHIMSCHI, C., BUHIMSCHI, I., SHI, L., SHI, S., AND CHWALISZ, K. Control and assessment of the uterus and cervix during pregnancy and labour. *Human Reproduction Update 4*, 5 (1998), 673–695.

[66] GARFIELD, R., SIMS, S., DANIEL, E., ET AL. Gap junctions: their presence and necessity in myometrium during parturition. *Science 198*, 4320 (1977), 958–960.

[67] GARFIELD, R., AND YALLAMPALLI, C. Structure and function of uterine muscle. *The uterus* (1994), 54–93.

[68] GARFIELD, R. E., CHWALISZ, K., SHI, L., OLSON, G., AND SAADE, G. R. Instrumentation for the diagnosis of term and preterm labour. *Journal of Perinatal Medicine-Official Journal of the WAPM 26*, 6 (1998), 413–436.

[69] GARFIELD, R. E., AND MANER, W. L. Physiology and electrical activity of uterine contractions. 289–295.

[70] GARFIELD, R. E., MANER, W. L., MAUL, H., AND SAADE, G. R. Use of uterine emg and cervical lif in monitoring pregnant patients. *BJOG: An International Journal of Obstetrics & Gynaecology 112* (2005), 103–108.

[71] GOLDENBERG, R. L., CULHANE, J. F., IAMS, J. D., AND ROMERO, R. Epidemiology and causes of preterm birth. *The lancet 371*, 9606 (2008), 75–84.

[72] GONDRY, J., DUCHÊNE, J., AND MARQUE, C. First results on uterine emg monitoring during pregnancy. 2609–2610.

[73] GONDRY, J., MARQUE, C., DUCHENE, J., AND CABROL, D. Electrohysterography during pregnancy: preliminary report. *Biomedical instrumentation & technology 27*, 4 (1993), 318–324.

[74] GOTO, M., AND CSAPO, A. The effect of the ovarian steroids on the membrane potential of uterine muscle. *The Journal of general physiology 43*, 2 (1959), 455–466.

[75] GOVINDAN, R. B. Tracking the changes in synchrony of the electrophysiological activity as the uterus approaches labor using magnetomyographic technique. *Reproductive Sciences 22*, 5 (2015), 595–601.

[76] GRAMFORT, A., PAPADOPOULO, T., OLIVI, E., AND CLERC, M. Openmeeg: opensource software for quasistatic bioelectromagnetics. *Biomedical engineering online 9*, 1 (2010), 1.

[77] GRECH, R., CASSAR, T., MUSCAT, J., CAMILLERI, K. P., FABRI, S. G., ZERVAKIS, M., XANTHOPOULOS, P., SAKKALIS, V., AND VANRUMSTE, B. Review on solving the inverse problem in eeg source analysis. *Journal of neuroengineering and rehabilitation 5*, 1 (2008), 25.

[78] GROVA, C., DAUNIZEAU, J., LINA, J.-M., BÉNAR, C., BENALI, H., AND GOTMAN, J. Evaluation of eeg localization methods using realistic simulations of interictal spikes. *Neuroimage 29*, 3 (2006), 734–753.

[79] HAMALAINEN, M., AND ILMONIEMI, R. Interpreting measured magnetic fields of the brain: Estimates of current distribution. helsinki, finland: University of technology department of technical physics report. p. Tech. rep., TKK-F-A559, 1984.

[80] HÄMÄLÄINEN, M. S., AND ILMONIEMI, R. J. Interpreting magnetic fields of the brain: minimum norm estimates. *Medical and biological engineering and computing 32*, 1 (1994), 35–42.

[81] HASSAN, M., SHAMAS, M., KHALIL, M., EL FALOU, W., AND WENDLING, F. Eegnet: an open source tool for analyzing and visualizing m/eeg connectome. *PloS one 10*, 9 (2015), e0138297.

[82] HASSAN, M., TERRIEN, J., ALEXANDERSSON, A., MARQUE, C., AND KARLSSON, B. Improving the classification rate of labor vs. normal pregnancy contractions by using ehg multichannel recordings. In *Engineering in Medicine and Biology Society (EMBC), 2010 Annual International Conference of the IEEE* (2010), IEEE, pp. 4642–4645.

[83] HASSAN, M., TERRIEN, J., KARLSSON, B., AND MARQUE, C. Interactions between uterine emg at different sites investigated using wavelet analysis: comparison of pregnancy and labor contractions. *EURASIP Journal on Advances in Signal Processing 2010* (2010), 17.

[84] HASSAN, M., TERRIEN, J., MUSZYNSKI, C., ALEXANDERSSON, A., MARQUE, C., AND KARLSSON, B. Better pregnancy monitoring using nonlinear correlation analysis of external uterine electromyography. *IEEE Transactions on Biomedical Engineering 60*, 4 (2013), 1160–1166.

[85] He, B., and Cohen, R. J. Body surface laplacian ecg mapping. *IEEE Transactions on Biomedical Engineering 39*, 11 (1992), 1179–1191.

[86] Hill, M. A., Zou, H., Potocnik, S. J., Meininger, G. A., and Davis, M. J. Invited review: arteriolar smooth muscle mechanotransduction: Ca2+ signaling pathways underlying myogenic reactivity. *Journal of applied physiology 91*, 2 (2001), 973–983.

[87] Iams, J. D. Prediction and early detection of preterm labor. *Obstetrics & Gynecology 101*, 2 (2003), 402–412.

[88] Ivancevic, T., Jain, L., Pattison, J., and Hariz, A. Preterm birth analysis using nonlinear methods. *Recent Patents on Biomedical Engineering 1*, 3 (2008), 160–170.

[89] Iwaki, S., and Ueno, S. Weighted minimum-norm source estimation of magnetoencephalography utilizing the temporal information of the measured data. *Journal of Applied physics 83*, 11 (1998), 6441–6443.

[90] Karlsson, B., Terrien, J., Gudmundsson, V., Steingrimsdottir, T., and Marque, C. Abdominal ehg on a 4 by 4 grid: mapping and presenting the propagation of uterine contractions. In *11th Mediterranean Conference on Medical and Biomedical Engineering and Computing 2007* (2007), Springer, pp. 139–143.

[91] KENNEDY, D., and TAKEDA, K. Reflex control of abdominal flexor muscles in the crayfish: I. the twitch system. *Journal of Experimental Biology 43*, 2 (1965), 211–227.

[92] Kliegman, R. M., Behrman, R. E., Jenson, H. B., and Stanton, B. M. *Nelson textbook of pediatrics e-book*. Elsevier Health Sciences, 2007.

[93] Koles, Z. J. Trends in eeg source localization. *Electroencephalography and clinical Neurophysiology 106*, 2 (1998), 127–137.

[94] Kuriyama, H., and Suzuki, H. Changes in electrical properties of rat myometrium during gestation and following hormonal treatments. *The Journal of Physiology 260*, 2 (1976), 315–333.

[95] Kybic, J., Clerc, M., Abboud, T., Faugeras, O., Keriven, R., and Papadopoulo, T. A common formalism for the integral formulations of the forward eeg problem. *IEEE transactions on medical imaging 24*, 1 (2005), 12–28.

[96] Laforet, J., Rabotti, C., Terrien, J., Mischi, M., and Marque, C. Toward a multiscale model of the uterine electrical activity. *IEEE Transactions on Biomedical Engineering 58*, 12 (2011), 3487–3490.

[97] Lammers, T., Hennink, W., and Storm, G. Tumour-targeted nanomedicines: principles and practice. *British journal of cancer 99*, 3 (2008), 392.

[98] Lammers, W. J., Mirghani, H., Stephen, B., Dhanasekaran, S., Wahab, A., Al Sultan, M. A., and Abazer, F. Patterns of electrical propagation in the intact pregnant guinea pig uterus. *American Journal of Physiology-Regulatory, Integrative and Comparative Physiology 294*, 3 (2008), R919–R928.

[99] Lees-Miller, S. P., and Anderson, C. W. The human double-stranded dna-activated protein kinase phosphorylates the 90-kda heat-shock protein, hsp90 alpha at two nh2-terminal threonine residues. *Journal of biological chemistry 264*, 29 (1989), 17275–17280.

[100] Leitich, H., Brunbauer, M., Kaider, A., Egarter, C., and Husslein, P. Cervical length and dilatation of the internal cervical os detected by vaginal ultrasonography as markers for preterm delivery: a systematic review. *American journal of obstetrics and gynecology 181*, 6 (1999), 1465–1472.

[101] Leman, H., Marque, C., and Gondry, J. Use of the electrohysterogram signal for characterization of contractions during pregnancy. *IEEE transactions on biomedical engineering 46*, 10 (1999), 1222–1229.

[102] Li, G., and He, B. Non-invasive estimation of myocardial infarction by means of a heart-model-based imaging approach: a simulation study. *Medical and Biological Engineering and Computing 42*, 1 (2004), 128–136.

[103] Lowery, C., Eswaran, H., Murphy, P., and Wilson, J. Uterine magnetomyography, Apr. 9 2003. US Patent App. 10/411,027.

[104] Luciani. Canonical polyadic decomposition based on joint eigenvalue decomposition. *Chemometrics and Intelligent Laboratory Systems 132* (2014), 152–167.

[105] Luciani, X., and Albera, L. Semi-algebraic canonical decomposition of multi-way arrays and joint eigenvalue decomposition. In *2011 IEEE International Conference on Acoustics, Speech and Signal Processing (ICASSP)* (2011), IEEE, pp. 4104–4107.

[106] Lucovnik, M., Maner, W. L., Chambliss, L. R., Blumrick, R., Balducci, J., Novak-Antolic, Z., and Garfield, R. E. Noninvasive uterine electromyography for prediction of preterm delivery. *American journal of obstetrics and gynecology 204*, 3 (2011), 228–e1.

[107] Maner, W. L., Garfield, R. E., Maul, H., Olson, G., and Saade, G. Predicting term and preterm delivery with transabdominal uterine electromyography. *Obstetrics & Gynecology 101*, 6 (2003), 1254–1260.

[108] MANSOUR, S. Etude de l'electromyographie uterine: caracterisation, propagation, modelisation des transferts.

[109] MANSOUR, S., DEVEDEUX, D., GERMAIN, G., MARQUE, C., AND DUCHÊNE, J. Uterine emg spectral analysis and relationship to mechanical activity in pregnant monkeys. *Medical and Biological Engineering and Computing 34*, 2 (1996), 115–121.

[110] MARQUE, C., DIAB, A., LAFORÊT, J., HASSAN, M., AND KARLSSON, B. Dynamic behavior of uterine contractions: an approach based on source localization and multiscale modeling. 527–540.

[111] MARQUE, C., AND DUCHENE, J. Human abdominal ehg processing for uterine contraction monitoring. *Biotechnology (Reading, Mass.) 11* (1989), 187.

[112] MARQUE, C., DUCHENE, J. M., LECLERCQ, S., PANCZER, G. S., AND CHAUMONT, J. Uterine ehg processing for obstetrical monitorng. *IEEE transactions on biomedical engineering*, 12 (1986), 1182–1187.

[113] MARQUE, C., LEMAN, H., VOISINE, M., GONDRY, J., AND NAEPELS, P. Traitement de l'électromyogramme utérin pour la caractérisation des contractions pendant la grossesse. *RBM-News 21*, 9 (1999), 200–211.

[114] MARQUE, C. K., TERRIEN, J., RIHANA, S., AND GERMAIN, G. Preterm labour detection by use of a biophysical marker: the uterine electrical activity. In *BMC pregnancy and childbirth* (2007), vol. 7, BioMed Central, p. S5.

[115] MARSHALL, J. Regulation of activity in uterine smooth muscle. *Physiological Reviews. Supplement 5* (1962), 213.

[116] MAUL, H., MANER, W. L., OLSON, G., SAADE, G. R., AND GARFIELD, R. E. Non-invasive transabdominal uterine electromyography correlates with the strength of intrauterine pressure and is predictive of labor and delivery. *The Journal of Maternal-Fetal & Neonatal Medicine 15*, 5 (2004), 297–301.

[117] MAUL, H., MANER, W. L., SAADE, G. R., AND GARFIELD, R. E. The physiology of uterine contractions. *Clinics in perinatology 30*, 4 (2003), 665–676.

[118] MCCOOL, M., AND FIUME, E. Hierarchical poisson disk sampling distributions. In *Proceedings of the conference on Graphics interface* (1992), vol. 92, pp. 94–105.

[119] MCLEAN, M., BISITS, A., DAVIES, J., WOODS, R., LOWRY, P., AND SMITH, R. A placental clock controlling the length of human pregnancy. *Nature medicine 1*, 5 (1995), 460.

[120] Mheich, A., Hassan, M., Wendling, F., Khalil, M., Dufor, O., Gripon, V., and Berrou, C. Simnet: A new algorithm for measuring brain networks similarity. In *Advances in Biomedical Engineering (ICABME), 2015 International Conference on* (2015), IEEE, pp. 119–122.

[121] Michel, C. M., Murray, M. M., Lantz, G., Gonzalez, S., Spinelli, L., and de Peralta, R. G. Eeg source imaging. *Clinical neurophysiology 115*, 10 (2004), 2195–2222.

[122] Miller, S., Garfield, R., and Daniel, E. Improved propagation in myometrium associated with gap junctions during parturition. *American Journal of Physiology-Cell Physiology 256*, 1 (1989), C130–C141.

[123] Mironneau, J. Excitation-contraction coupling in voltage clamped uterine smooth muscle. *The Journal of physiology 233*, 1 (1973), 127–141.

[124] Miwakeichi, F., Martinez-Montes, E., Valdés-Sosa, P. A., Nishiyama, N., Mizuhara, H., and Yamaguchi, Y. Decomposing eeg data into space–time–frequency components using parallel factor analysis. *NeuroImage 22*, 3 (2004), 1035–1045.

[125] Molins, A., Stufflebeam, S. M., Brown, E. N., and Hämäläinen, M. S. Quantification of the benefit from integrating meg and eeg data in minimum ℓ 2-norm estimation. *Neuroimage 42*, 3 (2008), 1069–1077.

[126] Morrison, J. C., Allbert, J. R., McLaughlin, B. N., Whitworth, N. S., Roberts, W. E., and Martin, R. W. Oncofetal fibronectin in patients with false labor as a predictor of preterm delivery. *American Journal of Obstetrics & Gynecology 168*, 2 (1993), 538–542.

[127] Moslem, B., Diab, M. O., Khalil, M., and Marque, C. Classification of multichannel uterine emg signals using a reduced number of channels. In *Mechatronics and its Applications (ISMA), 2012 8th International Symposium on* (2012), IEEE, pp. 1–4.

[128] Muszynski, C., Terrien, J., Drean, Y., Chkeir, A., Hassan, M., Marque, C., and Gondry, J. Evolution of electrohysterogram signals synchronization according to term of pregnancy: interest for preterm labor diagnosis. *Gynecologie, obstetrique & fertilite 40*, 6 (2012), 344–349.

[129] Nader, N. *Connectivity analysis of the EHG during pregnancy and Labor*. PhD thesis, UTC Compiègne; Université Libanaise (Liban), 2017.

[130] Nader, N., Hassan, M., Khalil, M., Marque, C., and Falou, W. From ehg signals to graphs: A new method for predicting premature birth. In *Journées RITS 2015* (2015), pp. pp–182.

[131] Nader, N., Zahran, S., Marque, C., Hassan, M., Yochum, M., Falou, W., and Khalil, M. Graph analysis of uterine networks using ehg source connectivity. In *Advances in Biomedical Engineering (ICABME), 2017 Fourth International Conference on* (2017), IEEE, pp. 1–4.

[132] NÉDÉLEC, J.-C. Acoustic and electromagnetic equations: integral representations for harmonic problems.

[133] NEWMAN, M. E. Assortative mixing in networks. *Physical review letters 89*, 20 (2002), 208701.

[134] NGUYEN, V.-H., LE, A.-C., AND HUYNH, V.-N. *Knowledge and Systems Engineering: Proceedings of the Sixth International Conference KSE 2014*, vol. 326. Springer, 2014.

[135] NOLTE, G., BAI, O., WHEATON, L., MARI, Z., VORBACH, S., AND HALLETT, M. Identifying true brain interaction from eeg data using the imaginary part of coherency. *Clinical neurophysiology 115*, 10 (2004), 2292–2307.

[136] PARKINGTON, H., HARDING, R., AND SIGGER, J. Co-ordination of electrical activity in the myometrium of pregnant ewes. *Journal of reproduction and fertility 82*, 2 (1988), 697–705.

[137] PARTHIMOS, D., EDWARDS, D. H., AND GRIFFITH, T. Minimal model of arterial chaos generated by coupled intracellular and membrane ca 2+ oscillators. *American Journal of Physiology-Heart and Circulatory Physiology 277*, 3 (1999), H1119–H1144.

[138] PASCUAL-MARQUI, R. D., ET AL. Standardized low-resolution brain electromagnetic tomography (sloreta): technical details. *Methods Find Exp Clin Pharmacol 24*, Suppl D (2002), 5–12.

[139] PASCUAL-MARQUI, R. D., MICHEL, C. M., AND LEHMANN, D. Low resolution electromagnetic tomography: a new method for localizing electrical activity in the brain. *International Journal of psychophysiology 18*, 1 (1994), 49–65.

[140] PEREDA, E., QUIROGA, R. Q., AND BHATTACHARYA, J. Nonlinear multivariate analysis of neurophysiological signals. *Progress in neurobiology 77*, 1-2 (2005), 1–37.

[141] PIJN, J., VELIS, D., AND DA SILVA, F. L. Measurement of interhemispheric time differences in generalised spike-and-wave. *Electroencephalography and clinical neurophysiology 83*, 2 (1992), 169–170.

[142] PIJN, J. P., AND DA SILVA, F. L. Propagation of electrical activity: nonlinear associations and time delays between eeg signals. In *Basic Mechanisms of the EEG*. Springer, 1993, pp. 41–61.

[143] RABOTTI, C., AND MISCHI, M. Propagation of electrical activity in uterine muscle during pregnancy: a review. *Acta Physiologica 213*, 2 (2015), 406–416.

[144] RABOTTI, C., MISCHI, M., VAN LAAR, J., AELEN, P., OEI, S., AND BERGMANS, J. Relationship between electrohysterogram and internal uterine pressure: a preliminary study. In *Engineering in Medicine and Biology Society, 2006. EMBS'06. 28th Annual International Conference of the IEEE* (2006), IEEE, pp. 1661–1664.

[145] Radomski, D., Grzanka, A., Graczyk, S., and Przelaskowski, A. Assessment of uterine contractile activity during a pregnancy based on a nonlinear analysis of the uterine electromyographic signal. In *Information Technologies in Biomedicine*. Springer, 2008, pp. 325–331.

[146] Ramon, C., Preissl, H., Murphy, P., Wilson, J. D., Lowery, C., and Eswaran, H. Synchronization analysis of the uterine magnetic activity during contractions. *Biomedical engineering online 4*, 1 (2005), 55.

[147] Renthal, N. E., Chen, C.-C., Koriand'r, C. W., Gerard, R. D., Prange-Kiel, J., and Mendelson, C. R. mir-200 family and targets, zeb1 and zeb2, modulate uterine quiescence and contractility during pregnancy and labor. *Proceedings of the National Academy of Sciences 107*, 48 (2010), 20828–20833.

[148] Renthal, N. E., Koriand'r, C. W., and Mendelson, C. R. Micrornas—mediators of myometrial contractility during pregnancy and labour. *Nature Reviews Endocrinology 9*, 7 (2013), 391.

[149] Rihana, S., Lefrancois, E., and Marque, C. A two dimension model of the uterine electrical wave propagation. 1109–1112.

[150] Rihana, S., Santos, J., Mondie, S., and Marque, C. Dynamical analysis of uterine cell electrical activity model. In *Engineering in Medicine and Biology Society, 2006. EMBS'06. 28th Annual International Conference of the IEEE* (2006), IEEE, pp. 4179–4182.

[151] Rihana, S., Terrien, J., Germain, G., and Marque, C. Mathematical modeling of electrical activity of uterine muscle cells. *Medical & biological engineering & computing 47*, 6 (2009), 665–675.

[152] Riley, G., Harrall, R., Constant, C., Chard, M., Cawston, T., and Hazleman, B. Tendon degeneration and chronic shoulder pain: changes in the collagen composition of the human rotator cuff tendons in rotator cuff tendinitis. *Annals of the rheumatic diseases 53*, 6 (1994), 359.

[153] Rodriguez, E., George, N., Lachaux, J.-P., Martinerie, J., Renault, B., and Varela, F. J. Perception's shadow: long-distance synchronization of human brain activity. *Nature 397*, 6718 (1999), 430.

[154] Romero, R., Nicolaides, K., Conde-Agudelo, A., Tabor, A., O'brien, J. M., Cetingoz, E., Da Fonseca, E., Creasy, G. W., Klein, K., Rode, L., et al. Vaginal progesterone in women with an asymptomatic sonographic short cervix in the midtrimester decreases preterm delivery and neonatal morbidity: a systematic review and metaanalysis of individual patient data. *American journal of obstetrics and gynecology 206*, 2 (2012), 124–e1.

[155] RONCALI, J., GARREAU, R., YASSAR, A., MARQUE, P., GARNIER, F., AND LEMAIRE, M. Effects of steric factors on the electrosynthesis and properties of conducting poly (3-alkylthiophenes). *Journal of Physical Chemistry 91*, 27 (1987), 6706–6714.

[156] RUBINOV, M., AND SPORNS, O. Complex network measures of brain connectivity: uses and interpretations. *Neuroimage 52*, 3 (2010), 1059–1069.

[157] SACHS, F. Stretch-activated ion channels: what are they? *Physiology 25*, 1 (2010), 50–56.

[158] SAKAI, N., TABB, T., AND GARFIELD, R. E. Studies of connexin 43 and cell-to-cell coupling in cultured human uterine smooth muscle. *American Journal of Obstetrics & Gynecology 167*, 5 (1992), 1267–1277.

[159] SCHERG, M., AND VON CRAMON, D. Evoked dipole source potentials of the human auditory cortex. *Electroencephalography and Clinical Neurophysiology/Evoked Potentials Section 65*, 5 (1986), 344–360.

[160] SCHLEMBACH, D., MANER, W. L., GARFIELD, R. E., AND MAUL, H. Monitoring the progress of pregnancy and labor using electromyography. *European Journal of Obstetrics & Gynecology and Reproductive Biology 144* (2009), S33–S39.

[161] SHI, S.-Q., MANER, W. L., MACKAY, L. B., AND GARFIELD, R. E. Identification of term and preterm labor in rats using artificial neural networks on uterine electromyography signals. *American journal of obstetrics and gynecology 198*, 2 (2008), 235–e1.

[162] SI, H., AND TETGEN, A. A quality tetrahedral mesh generator and three-dimensional delaunay triangulator. *Weierstrass Institute for Applied Analysis and Stochastic, Berlin, Germany* (2006), 81.

[163] SIKORA, J., MATONIA, A., CZABANSKI, R., HOROBA, K., JEZEWSKI, J., AND KUPKA, T. Recognition of premature threatening labour symptoms from bioelectrical uterine activity signals. *Archives of perinatal medicine 17*, 2 (2011), 97–103.

[164] SMITH, R., IMTIAZ, M., BANNEY, D., PAUL, J. W., AND YOUNG, R. C. Why the heart is like an orchestra and the uterus is like a soccer crowd. *American journal of obstetrics and gynecology 213*, 2 (2015), 181–185.

[165] SONG, S., ROOIJAKKERS, M., HARPE, P., RABOTTI, C., MISCHI, M., VAN ROERMUND, A. H., AND CANTATORE, E. A low-voltage chopper-stabilized amplifier for fetal ecg monitoring with a 1.41 power efficiency factor. *IEEE transactions on biomedical circuits and systems 9*, 2 (2015), 237–247.

[166] STEINHÄUSER, C., KRESSIN, K., KUPRIJANOVA, E., WEBER, M., AND SEIFERT, G. Properties of voltage-activated na+ and k+ currents in mouse hippocampal glial cells in situ and after acute isolation from tissue slices. *Pflügers Archiv 428*, 5-6 (1994), 610–620.

[167] SUNDNES, J., LINES, G. T., AND TVEITO, A. Efficient solution of ordinary differential equations modeling electrical activity in cardiac cells. *Mathematical Biosciences 172*, 2 (2001), 55–72.

[168] SUREAU, C. Etude de l'activité électrique de l'utérus au cours du travail. *Gynecol Obstet 555* (1956), 153–175.

[169] TADEL, F., BAILLET, S., MOSHER, J. C., PANTAZIS, D., AND LEAHY, R. M. Brainstorm: a user-friendly application for meg/eeg analysis. *Computational intelligence and neuroscience 2011* (2011), 8.

[170] TAKEDA, H. Generation and propagation of uterine activity in situ. *Fertility and sterility 16*, 1 (1965), 113–119.

[171] TAWFIK, V. L., AND FLOOD, P. Electrical synapseshigh-speed communication in the maintenance of neuropathic pain. *Anesthesiology: The Journal of the American Society of Anesthesiologists 124*, 1 (2016), 13–15.

[172] TERRIEN, J., STEINGRIMSDOTTIR, T., MARQUE, C., AND KARLSSON, B. Synchronization between emg at different uterine locations investigated using time-frequency ridge reconstruction: comparison of pregnancy and labor contractions. *EURASIP Journal on Advances in Signal Processing 2010* (2010), 18.

[173] TONG, W.-C., TRIBE, R. M., SMITH, R., AND TAGGART, M. J. Computational modeling reveals key contributions of kcnq and herg currents to the malleability of uterine action potentials underpinning labor. *PloS one 9*, 12 (2014), e114034.

[174] TRUJILLO-BARRETO, N. J., AUBERT-VÁZQUEZ, E., AND VALDÉS-SOSA, P. A. Bayesian model averaging in eeg/meg imaging. *NeuroImage 21*, 4 (2004), 1300–1319.

[175] VIGMOND, E., DOS SANTOS, R. W., PRASSL, A., DEO, M., AND PLANK, G. Solvers for the cardiac bidomain equations. *Progress in biophysics and molecular biology 96*, 1-3 (2008), 3–18.

[176] VINKEN, M. P., RABOTTI, C., MISCHI, M., AND OEI, S. G. Accuracy of frequency-related parameters of the electrohysterogram for predicting preterm delivery: a review of the literature. *Obstetrical & gynecological survey 64*, 8 (2009), 529–541.

[177] WANG, D., KIRBY, R. M., MACLEOD, R. S., AND JOHNSON, C. R. Inverse electrocardiographic source localization of ischemia: An optimization framework and finite element solution. *Journal of computational physics 250* (2013), 403–424.

[178] WENDLING, F., BARTOLOMEI, F., BELLANGER, J., AND CHAUVEL, P. Interpretation of interdependencies in epileptic signals using a macroscopic physiological model of the eeg. *Clinical neurophysiology 112*, 7 (2001), 1201–1218.

[179] WILLIAMS, K. C., RENTHAL, N. E., GERARD, R. D., AND MENDELSON, C. R. The microrna (mir)-199a/214 cluster mediates opposing effects of progesterone and estrogen on uterine contractility during pregnancy and labor. *Molecular Endocrinology 26*, 11 (2012), 1857–1867.

[180] WILLIAMS, M. A., HICKOK, D. E., ZINGHEIM, R. W., MITTENDORF, R., KIMELMAN, J., AND MAHONY, B. S. Low birth weight and preterm delivery in relation to early-gestation vaginal bleeding and elevated maternal serum alpha-fetoprotein. *Obstetrics and gynecology 80*, 5 (1992), 745–749.

[181] WOLFS, G., AND ROTTINGHUIS, H. Electrical and mechanical activity of the human uterus during labourdie elektrische und mechanische aktivität des menschlichen uterus während der wehenperiode. *Archiv für Gynäkologie 208*, 4 (1970), 373–385.

[182] WOLFS, G. M. J. A., AND VAN LEEUWEN, M. Electromyographic observations on the human uterus during labour. *Acta obstetricia et gynecologica scandinavica 58*, sup90 (1979), 1–61.

[183] WORD, R. A., STULL, J. T., CASEY, M. L., AND KAMM, K. E. Contractile elements and myosin light chain phosphorylation in myometrial tissue from nonpregnant and pregnant women. *Journal of Clinical Investigation 92*, 1 (1993), 29.

[184] WRAY, S. Uterine contraction and physiological mechanisms of modulation. *American Journal of Physiology-Cell Physiology 264*, 1 (1993), C1–C18.

[185] YOCHUM, M., LAFORÊT, J., AND MARQUE, C. An electro-mechanical multiscale model of uterine pregnancy contraction. *Computers in Biology and Medicine 77* (2016), 182–194.

[186] YOUNG, R. C. Myocytes, myometrium, and uterine contractions. *Annals of the new york academy of sciences 1101*, 1 (2007), 72–84.

[187] YOUNG, R. C. Synchronization of regional contractions of human labor; direct effects of region size and tissue excitability. *Journal of biomechanics 48*, 9 (2015), 1614–1619.

[188] YOUNG, R. C. Mechanotransduction mechanisms for coordinating uterine contractions in human labour. *Reproduction* (2016), REP–16.

[189] YOUNG, R. C., AND GOLOMAN, G. Mechanotransduction in rat myometrium: coordination of contractions of electrically and chemically isolated tissues. *Reproductive Sciences 18*, 1 (2011), 64–69.

[190] ZAHRAN, S., YOCHUM, M., DIAB, A., AND MARQUE, C. Variation-based sparse source imaging in localizing uterine activity. In *Engineering in Medicine and Biology Society (EMBC), 2017 39th Annual International Conference of the IEEE* (2017), IEEE, pp. 2948–2951.

[191] ZIETEK, J., HOROBA, K., JEZEWSKI, J., MATONIA, A., SIKORA, J., AND KUPKA, T. Analysis of bioelectrical uterine activity for detection of threatening premature labour. In *14th Nordic-Baltic Conference on Biomedical Engineering and Medical Physics* (2008), Springer, pp. 469–472.

[192] ZOU, H., LIFSHITZ, L. M., TUFT, R. A., FOGARTY, K. E., AND SINGER, J. J. Imaging ca2+ entering the cytoplasm through a single opening of a plasma membrane cation channel. *The Journal of general physiology 114*, 4 (1999), 575–588.

[193] ZOU, H., LIFSHITZ, L. M., TUFT, R. A., FOGARTY, K. E., AND SINGER, J. J. Imaging calcium entering the cytosol through a single opening of plasma membrane ion channels: Sc-cafts—fundamental calcium events. *Cell Calcium 35*, 6 (2004), 523–533.

A

Appendix

A. EHG Computer Interface

Although EHG instrumentation is becoming more common in research centers and hospitals, research software availability and standardization remain limited. EHG source imaging poses a series of specific technical challenges (e.g., the multidimensional nature of the data, the multitude of approaches to modeling tissues and geometry, and the ambiguity of source modeling). Ideally, EHG imaging is multimodal: EHG recordings need to be registered to a source space that may be obtained from structural MRI data, which adds to the complexity of the analysis. EHG data analysis and source imaging feature a multitude of possible approaches, which draw on a wide range of signal processing techniques. Forward modeling, which maps elemental myometrium current sources to skin potentials, is dependent on the shape and conductivity of tissues and can be performed using a number of methods. Inverse source modeling, which resolves the myometrium sources that gave rise to EHG recordings, has been approached through a multitude of methods, [190]. This diversity of models and methods reflects the ill-posed nature of electrophysiological imaging which requires restrictive models or regularization procedures to ensure a stable inverse solution. In a clinical environment, raw recordings are often used to identify and characterize uterus activity [45, 127]. More recently, an increasing number of methods have been proposed to address the detection of functional connectivity among uterus regions [131]. Despite such daunting diversity and complexity in user needs and methodological approaches, an integrated soft- ware solution would be beneficial to the imaging community and provide progressive automation, standardization and reproducibility of some of the most common analysis pathways.

EHG are effective imaging techniques allowing for analysis of the dynamics of functional uterus networks at abdominal skin level and/or at reconstructed sources. However, a tool that can cover all the processing steps of identifying uterus networks from EHG signals is still missing. Here, we report an adaption of brainstorm software package [169] and eegnet tool [81] to uterus domain, running under MATLAB (Math works, inc), and allowing for analysis and visualization of functional uterus networks from EHG recordings. It includes 1) solving the forward problem 2) the solution of the inverse problem to localize / reconstruct the uterus sources, 3) the computation of functional connectivity among signals collected at the time courses of reconstructed sources, 4) simulate uterine activity in a determined region and 5) the computation of the network measures based on graph theory analysis. This unique tool combines the EHG functional connectivity analysis and the computation of network measures derived from the graph theory.

The processing pipeline is to identify, visualize and characterize uterus networks from EHG recordings. It can perform all steps including the estimation of uterus sources, the computation of the functional connectivity and the mapping of uterus networks at source level. The basic workflow is shown in Figure A.1.

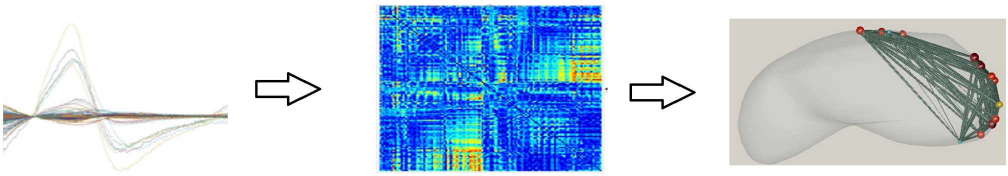

Reconstructed sources Uterus regions Uterus network

Figure A.1: The EHG data can be used to estimate the uterus sources by solving the inverse problem. Functional connectivity measures can be applied on the reconstructed sources. Graph measures can be computed and the correspondent uterus network can be visualized. Node's size and color can be used to encode any chosen network measures (their strength for instance) as well as the edges (their weight for instance)..

The main elements are:

The data. This file represents either the EHG data or the reconstructed sources. The default file format is the '.mat'. It should be a 3 dimensional matrix $(N_c x N_s x N_t)$ where $N_c, N_s and N_t$ are the channels (uterus regions in the case of sources file) number, the sample size and the number of trials (N_t is considered 1 for data averaged over trials), respectively. When solving the inverse problem and for visualizing the network at electrode level, the electrode location file is required. Both the.xyz and.mat formats are supported.

The imported data can be firstly visualized.

The adjacency matrix. This file is an $N_c x N_c$ dimension. It contains the values of the functional connections between all the channels (or uterus regions). This file can be also in $N_s x N_c x N_c$ in the case where it is the dynamics of functional networks that is being analyzed. To compute the functional connectivity (FC) matrices, four methods are available: the cross-correlation, the mean phase coherence (MPC), the mutual information (MI) and the Phase Locking Value (PLV), see section 4.2.3. After choosing the desired method, the connectivity values can be computed over EHG signals (generating 2D networks) or over the time series associated with the reconstructed sources (generating 3D networks at uterus level). To assess the significance of the obtained connections, surrogates data analysis can be used and a level of significance can be set which allow users to keep only the statistically significant connections (see [153] for details about this approach). The output of this analysis is the matrix containing only the significant connections.

Visualization of the Data Brainstorm provides a rich interface for displaying and interacting with EHG recordings including various displays of time series, topographical mapping on 2D or 3D surfaces

Source modeling

We now need to obtain a model that explains how uterine electric currents (the source space) produce differences in electrical potentials at external sensors (the sensor space), given the different tissues (essentially uterus, muscle, fat and skin)(Figure A.2) .

The process of modeling how data values can be obtained outside of the uterus with EHG from electrical current dipoles in the uterus is called forward modeling.

We will obtain a matrix $[N_{sensors} * N_{sources}]$ that relates the activity of the sources to the sensor data collected during the experiment.

For solving the EHG forward modeling OpenMEEG BEM: Symmetric Boundary Element Method from the open-source software OpenMEEG was used.

After having the forward model in the database that explains how the uterus sources determine the values on the sensors. This is useful for simulations, but what we need next is to solve the inverse problem: how to estimate the sources when we have the recordings.

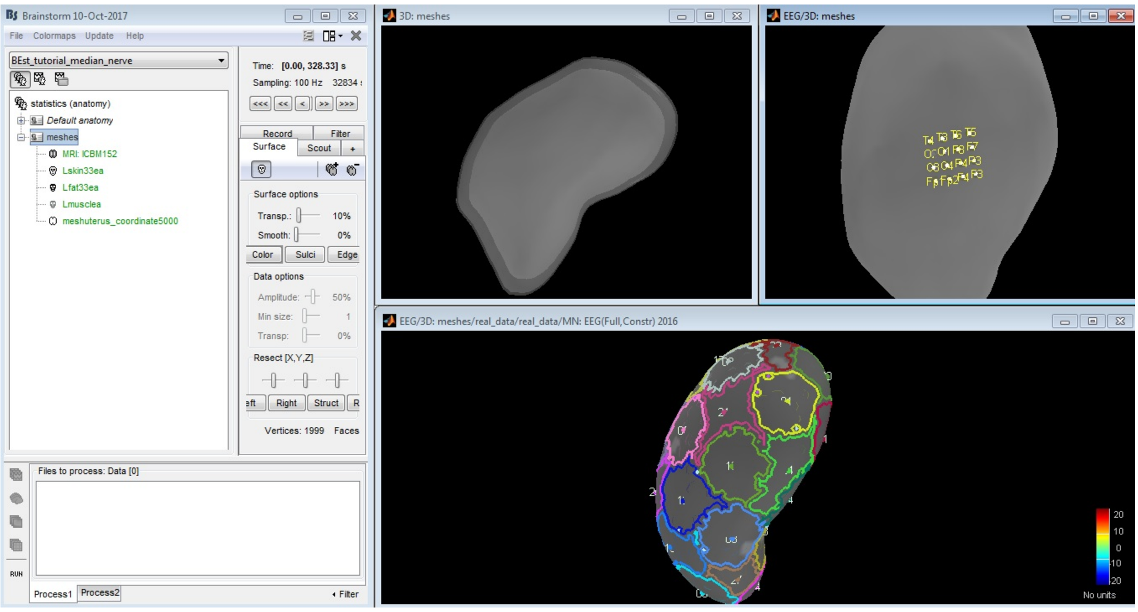

Figure A.2: The interface of forward modeling computation

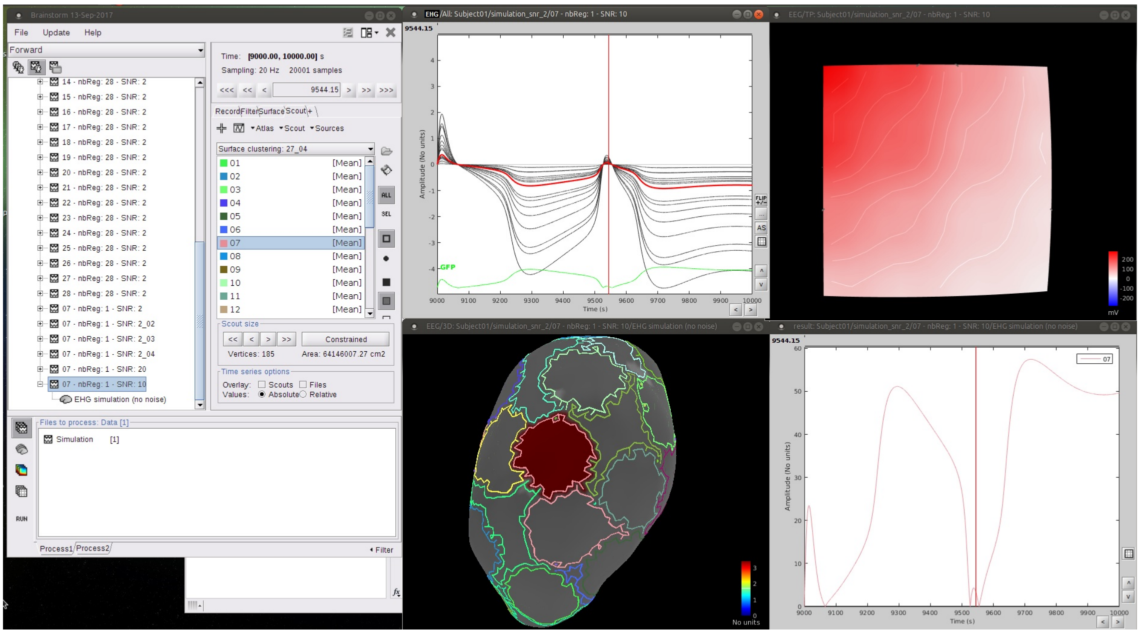
Brainstorm 13-Sep-2017

Forward

14 - nbReg: 28 - SNR: 2
15 - nbReg: 28 - SNR: 2
16 - nbReg: 28 - SNR: 2
17 - nbReg: 28 - SNR: 2
18 - nbReg: 28 - SNR: 2
19 - nbReg: 28 - SNR: 2
20 - nbReg: 28 - SNR: 2
21 - nbReg: 28 - SNR: 2
22 - nbReg: 28 - SNR: 2
23 - nbReg: 28 - SNR: 2
24 - nbReg: 28 - SNR: 2
25 - nbReg: 28 - SNR: 2
26 - nbReg: 28 - SNR: 2
27 - nbReg: 28 - SNR: 2
28 - nbReg: 28 - SNR: 2
07 - nbReg: 1 - SNR: 2
07 - nbReg: 1 - SNR: 2_02
07 - nbReg: 1 - SNR: 2_03
07 - nbReg: 1 - SNR: 2_04
07 - nbReg: 1 - SNR: 20
07 - nbReg: 1 - SNR: 10
EHG simulation (no noise)

Time: [9000.00, 10000.00] s
Sampling: 20 Hz 20001 samples
9544.15

Surface clustering: 27_04
01 [Mean]
02 [Mean]
03 [Mean]
04 [Mean]
05 [Mean]
06 [Mean]
07 [Mean]
08 [Mean]
09 [Mean]
10 [Mean]
11 [Mean]
12 [Mean]

Scout size
Constrained
Vertices: 185 Area: 64146007.27 cm2

Time series options
Overlay: ☐ Scouts ☐ Files
Values: ● Absolute ○ Relative

Files to process: Data [1]
Simulation [1]

EHG/All: Subject01/simulation_snr_2/07 - nbReg: 1 - SNR: 10

EEG/TP: Subject01/simulation_snr_2/07 - nbReg: 1 - SNR: 10

EEG/3D: Subject01/simulation_snr_2/07 - nbReg: 1 - SNR: 10/EHG simulation (no noise)

result: Subject01/simulation_snr_2/07 - nbReg: 1 - SNR: 10/EHG simulation (no noise)

Figure A.3: The interface of inverse modeling computation

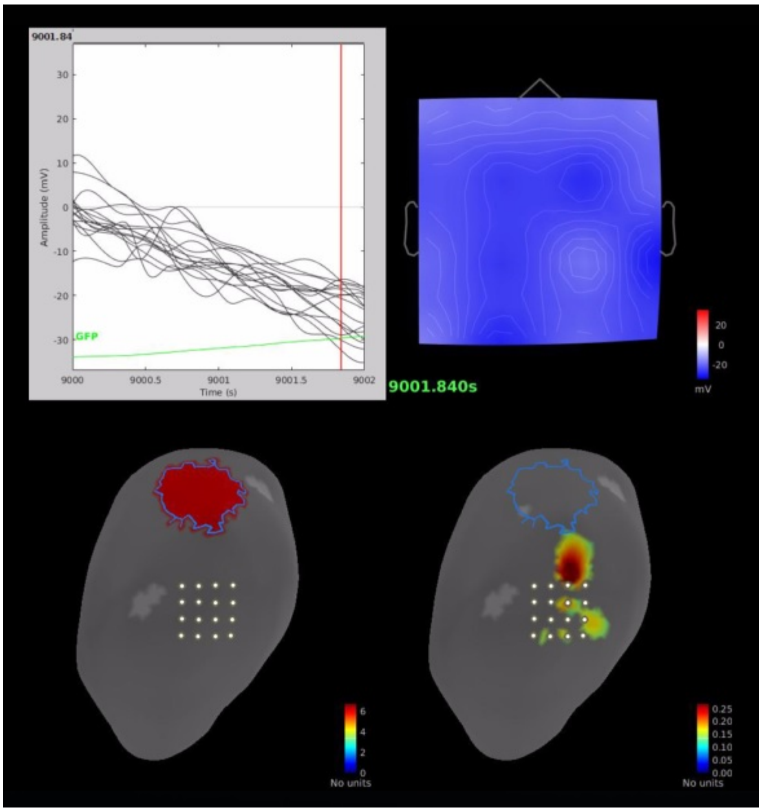

Figure A.4: Source estimation of a region far from electrodes

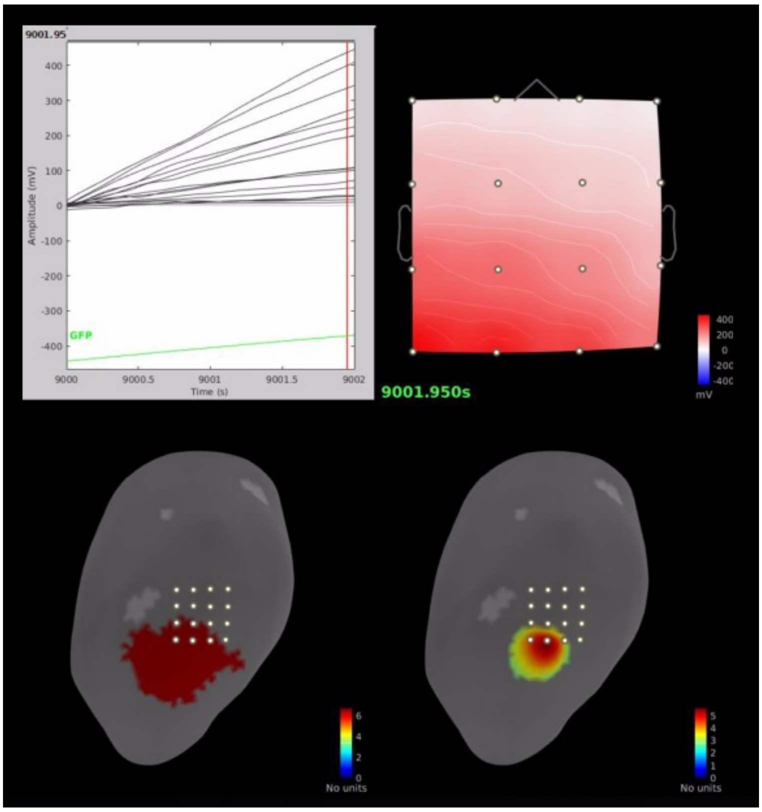

Figure A.5: Source estimation of a region near from electrodes

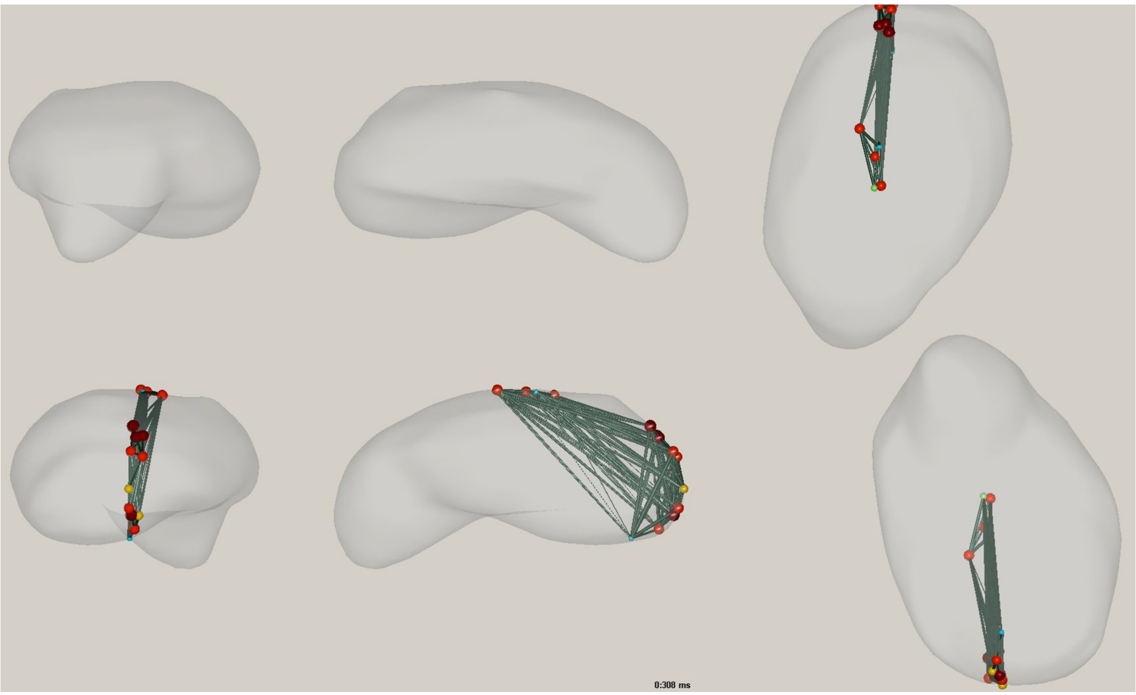

Figure A.6: Multiview of uterus netwark

B. Region growing algorithm

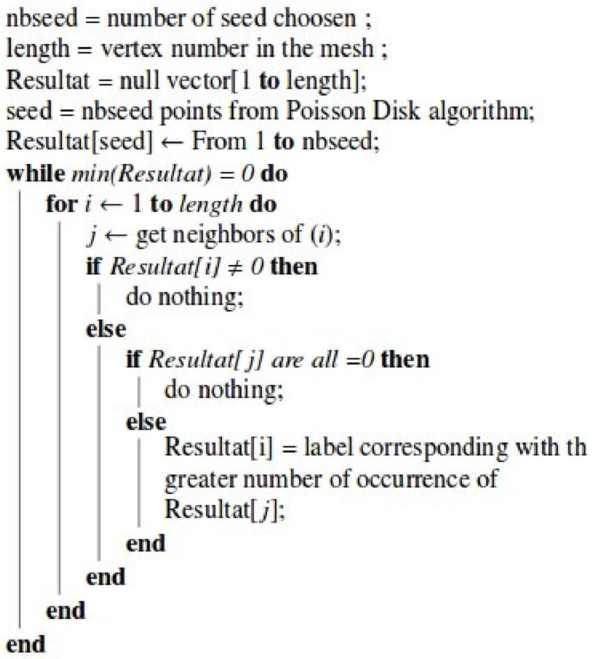

```
nbseed = number of seed choosen ;
length = vertex number in the mesh ;
Resultat = null vector[1 to length];
seed = nbseed points from Poisson Disk algorithm;
Resultat[seed] ← From 1 to nbseed;
while min(Resultat) = 0 do
    for i ← 1 to length do
        j ← get neighbors of (i);
        if Resultat[i] ≠ 0 then
            do nothing;
        else
            if Resultat[j] are all =0 then
                do nothing;
            else
                Resultat[i] = label corresponding with th
                greater number of occurrence of
                Resultat[j];
            end
        end
    end
end
```

Algorithm 1: Region-growing algorithms